# search for SM Higgs decaying to two photons via ATLAS detector

*by*

Yaquan Fang

A dissertation submitted in partial fulfillment of the

requirements for the degree of

Doctor of Philosophy

(Physics)

*at the*

University of Wisconsin – Madison

2008

# Abstract

This dissertation reports the discovery potential of the Standard Model Higgs boson with the di-photon decay using the ATLAS detector. First, photon calibration techiques is studied and a likelihood method for photon identification and jet rejection is developed. A method to evaluate photon identification and fake photon backgrounds with data was also discussed. The potential of an inclusive SM Higgs decaying to two photons search and Higgs boson searches in association with one or two high $P_T$ jets is evaluated. Finally an extended maximum likelihood fit together with event classifications was performed to estimate the sensitivity of the search. With 30 $\text{fb}^{-1}$ data, the expected sensitivity for the channel Higgs decaying to two photons is above 5 sigma for Higgs masses between 120 and 140 GeV.

# Acknowledgements

This work can not be done without the the kind aid and helpful guidance from quite a few people. I would like to sincerely appreciate the following people. I am greatly indebted to my wife, Yi, for her huge sacrifices and endless patience. I would like to be grateful to my parents Desong and Jinxian. Their incredible support for my education is immeasurable. I also think to my old brother Yaxiang whose dedication and diligence have great influence on me.

A few more teachers or professors in China I would like to thanks are Yuzi Ding, Xiaowen Zi and Professor Nanshan Ai. Their kindness has deeply deposited in my mind. I also need to appreciate Professor David Garelick and Pran Nath who motivate my interest in high energy physics.

In the past five years I worked in Wisconsin group led by Sau Lan Wu. I appreciate the happy time with those colleagues: Ruslan Asfandiyarov, Andrey Bagrov, German Carillo, Alfredo Castaneda, Elizabeth Castaneda, Xin Chen, Dos Anjos André, Luis Flores Castillo, Yibin Pan, Isabel Pedraza, Haiping Peng, Bill Quayle, Tapas Sarangi, Sepehr Saremi, Trevor Vickey, Haichen Wang, Werner Wiedenmann,TT Wu, Yichun Zhu, Haimo Zobering, Kyle Cranmer, Nathan Goldschmidt, Sanjay Padhi, Stathes Paganis, Alden Stradling, Karina Loureiro. I also want to give a warm thanks to Wen Guan, Neng Xu, Mengmeng Chen for assistance related with computing. I am also greatly appreciate Annabelle Leung, Antonella Lofranco, Catharine Noble for various help. In particular, I would like to appreciate Trevor Vickey, Bill Quayle, Annabelle Leung and Bruce Mellado for carefully proofreading the thesis and give plenty literal

corrections, advice and suggestion in physics.

I also want to thank the assistance from the ATLAS Collaboration. The Monte Carlo generated by central production is widely used in this dissertation. I would appreciate the cooperation and fruitful discussion and helpful advice from Nicolas Berger, Tanaka Junichi, Hyeonjin Kim, Guillaume Unal, Dirk Zerwas, Ning Zhou.

The work was supported by US Department Energy Grant DE-FG0295-ER40896.

Finally, This work is supervised by Professor Sau Lan Wu and Professor Bruce Mellado. Sau Lan's dedication and comprehensive assistance drive the dissertation into the right direction with full speed. Bruce gives me most direct advise and education in the past five years. His enthusiasm, dedication, hard working and keen insight sets me a good example.

# Contents

# List of Tables

# List of Figures

# Chapter 1

# The Higgs mechanism in the Standard Model of Particle Physics

Nature is composed of matter and energy. The Standard Model of Particle Physics is so far the most successful model to understand the dynamics between those two basic components of nature. The most fundamental particles described by the Standard Model are all known as fermions which means the spin of the particle is 1/2. Apart from their antiparticle partners, a total of twelve different types of matter particles are known and accounted for by the Standard Model. Forces are transmitted via mediating particles. Currently, we know four fundamental forces: gravity, the electromagnetic force, weak nuclear force and strong nuclear force. The mediating particle corresponding to those forces are the graviton, photon, weak bosons ($W^+$,$W^-$,$Z^0$), gluon. Those particles are bosons with integer spins [1].

Gravity is partially understood by Albert Einstein with his general relativity theory [2]. His theory is distinguished from other metric theories of gravitation by its use of field equations to relate space-time content and space-time curvature. Quantum field theory (QFT) [3] provides a theoretical framework for particle and condensed

matter physics. Combined with relativistic quantum mechanics and group theory, QFT describes the other three forces and all associated particles. Although QFT and general relativity can almost explain all force and fundamental particles, the effort to unify them in one uniform frame has not yet succeeded. In principle, one should expect that one theory can unify all of forces and fundamental particles. Some new theory such as superstring theory or M theory [4] offer the prospect of a possible ultimate unification of all fundamental particles and forces and prediction of physics at higher energy scale.

## 1.1 Standard Model and Motivation of the Higgs mechanism

Symmetry [5] is one of the most profound principles for theoretical physics. The physics language for symmetry is the invariance under some translation. This invariance gives rise to conservation law in classical physics, i.e. invariance under time displacements, translations leads to the conservation of energy, momentum and angular momentum in classical mechanics, respectively.

In particle physics, a particle is described by a complex quantum field, while the translation is denoted by a phase transformation, which normally forms a unitary group. So far, one of the most popular quantum field theories to describe the properties and interaction of fundamental particles is known as the Standard Model. The group present in Standard Model is $U(1)_Y \otimes SU(2)_L \otimes SU(3)_{color}$. The factorized term of $U(1)_Y$ corresponds to electromagnetic interactions. Similarly, $SU(2)_L$ and $SU(3)_{color}$ lead to weak and strong interactions. Renormalizability is the key for a successful model in particle physics. It has been shown by 't Hooft [6] that for a theory to be renormalizable, it must be Yang-Mills theory [7], namely a theory with

local gauge invariance. In classical mechanics the connection between symmetries and conservation laws has been discussed in the framework of a Lagrangian field. In analogy, the Lagrangian formalism is requried to be invariant under local gauge transformations. For example, in QED the Lagrangian for an electron can be written as $\mathcal{L} = i\overline{\Psi}\gamma^\mu\partial_\mu\Psi - m\overline{\Psi}\Psi$. In order to keep the invariance of the Lagrangian under local gauge transformations, a vector field $A_\mu$, which has to be massless, is introduced. The new Lagrangian formula is like the following:

$$\mathcal{L} = i\overline{\Psi}(i\gamma^\mu\partial_\mu - m)\Psi + e\overline{\Psi}\gamma^\mu A_\mu\Psi - \frac{1}{4}F_{\mu\nu}F^{\mu\nu}. \tag{1.1}$$

where $F_{\mu\nu} = \partial_\mu A_\nu - \partial_\nu A_\mu$. The first term is the original electron field. The second one denotes the coupling between an electron and the new vector field. The last term is the kinetic term for the massless vector field which is regarded as a photon. In an analogous way, one can extend the idea above but replace $U(1)$ transformations on an electron field by $SU(3)$ transformations on a quark color field. This theory, which is called Quantum Chromodynamics (QCD), predicts eight massless vector gluon fields. The three jet events at Tasso with process $e^+e^- \to q\overline{q}g$ was the first direct evidence of the gluon [8, 9]. The gauge invariant QCD lagrangian is :

$$\mathcal{L} = \overline{q}(i\gamma^\mu\partial_\mu - m)q - g_s(\overline{q}\gamma^\mu T_a q)G^a_\mu - \frac{1}{4}G^a_{\mu\nu}G^{\mu\nu}_a. \tag{1.2}$$

where $G^a_{\mu\nu}$ is counterpart of $F_{\mu\nu}$, but with more complicated form : $G^a_{\mu\nu} = \partial_\mu G^a_\nu - \partial_\nu G^a_{mu} - g_s f_{abc} G^b_\mu G^c_\nu$. We can see that both mediators, photon and gluon, are required to be massless since the presence of a mass term for gauge fields breaks the gauge invariance of Lagrangian. The problem will arise when we apply gauge symmetry to the weak interaction which, as we know in experiment, are mediated by massive

gauge bosons ($W^{\pm}$ and Z). In this case, we have to either give up gauge invariance which will cause the theory to be non renormalizable (i.e., divergent) or ignore the experimental fact (the $W^{\pm}$, Z bosons were discovered at the CERN SPS by UA1 and UA2 experiments [10, 11]) that $W^{\pm}$ and Z have a mass on the order of 100 GeV. A mechanism called Spontaneous Symmetry breaking was proposed to introduce mass without breaking gauge invariance [12, 13].

## 1.2 The Higgs mechanism

For a single local SU(2) doublet of complex scalar fields:

$$\phi = \begin{pmatrix} \phi^+ \\ \phi^0 \end{pmatrix}. \tag{1.3}$$

The lagrangian is :

$$\mathcal{L} = (D_\mu \phi)(D^\mu \phi^\dagger) - \mu^2 \phi^\dagger \phi - \lambda(\phi^\dagger \phi)^2. \tag{1.4}$$

In this formula, $D_\mu = \partial_\mu + ig\frac{\tau_\alpha}{2}W_\mu^\alpha$ where $W_\mu^\alpha(x)$ with $\alpha = 1, 2, 3$ are three gauge fields, $g$ is the coupling constant and $\tau$ is linearly independent traceless $2 \times 2$ matrices. The last two terms of $\mathcal{L}$ correspond to the potential. In the case $\mu^2 < 2$, the potential has minimal at $\phi^\dagger \phi = \frac{\nu^2}{2} = -\frac{\mu^2}{2\lambda}$ as Figure 1.1 shows. The field $\phi$ develops a vacuum expectation value:

$$\langle \phi \rangle = \frac{1}{\sqrt{2}} \begin{pmatrix} 0 \\ \mu \end{pmatrix}. \tag{1.5}$$

The expansion of $\phi$ about $\langle \phi \rangle$ and gauge invariance principle imply that:

$$\phi(x) = \frac{1}{\sqrt{2}} \begin{pmatrix} 0 \\ \nu + h(x) \end{pmatrix}. \tag{1.6}$$

So there are four degrees of freedom $h(x)$ and $W^{\alpha}$ $(\alpha = 1, 2, 3)$. Three of them give rise to longitudinal modes of the $W^{+}$,$W^{-}$ and $Z^{0}$. The remaining degree of freedom is the Higgs boson. By applying the Higgs Mechanism on the electroweak

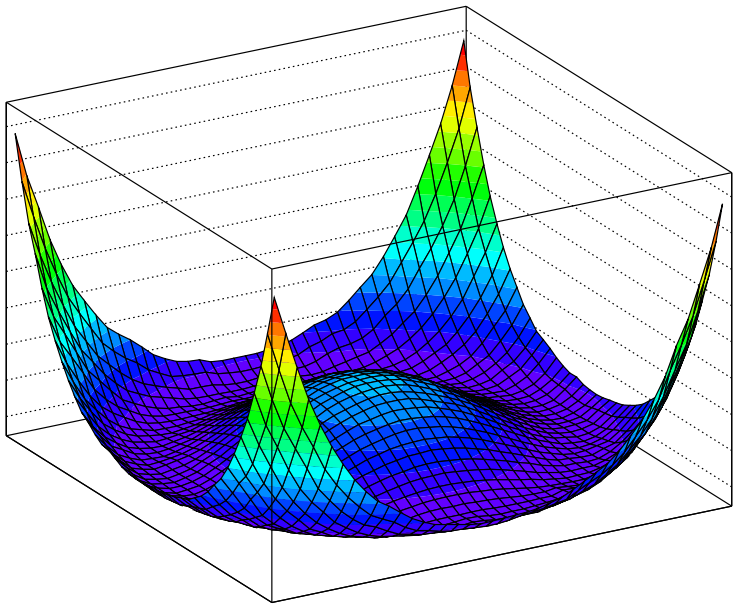

Figure 1.1: the potential $V(\phi)$ for a complex scalar field in the case $\mu^2 < 0$ and $\lambda > 0$ .

interaction, Glashow, Weinberg and Salam [14, 15, 16] successfully cast electroweak interaction into an $U(1)_Y \otimes SU(2)_L$ invariant Lagrangian. In this framework, they predicted the massive $W^{\pm}$, Z bosons and a neutral scalar Higgs boson. After gathering all the ingredients of Lagrangian, the complete one for the Standard Model is :

$$\mathcal{L} = \frac{1}{4}W_{\mu\nu}W^{\mu\nu} - \frac{1}{4}B_{\mu\nu}B^{\mu\nu} - \frac{1}{4}F_{\mu\nu}F^{\mu\nu} \tag{1.7}$$
$$+\overline{L}\gamma^{\mu}(i\partial_{\mu} - g\frac{1}{2}\tau \cdot W_{\mu} - g'\frac{Y}{2}B_{\mu})L + \overline{R}\gamma^{\mu}(i\partial_{\mu} - g'\frac{Y}{2}B_{\mu})R$$
$$+|(i\partial_{\mu} - g'\frac{Y}{2}B_{\mu})\Phi|^2 - V(\Phi)$$
$$+g''(\overline{q}\gamma^{\mu}T_{\alpha}q)G_{\mu}^{\alpha}$$
$$+G_1\overline{L}\Phi R + G_2\overline{L}\Phi_c R + h.c.$$

where $g$, $g'$, $g''$ correspond to the coupling constants for U(1), SU(2) and SU(3) groups, respectively. L and R denote the left-handed fermion doublet and right-handed fermion singlet. $W_{\mu}$ and $Z_{\mu}$ are gauge boson fields. The terms on the first line include kinetic energies and the self interaction of gauge bosons $W^{\pm}$,Z and $\gamma$. Those on the second line are kinematic energies of fermions and their interaction with a gauge boson. The last three terms are related to $W^{\pm}$, Z, $\gamma$ and the Higgs masses and couplings, interactions between quarks and gluons, fermion masses and couplings to the Higgs.

## 1.3 Higgs production and decay at the LHC

The LHC is a proton-proton collider. As a hadronic collider with $\sqrt{s} = 14$ TeV, the most dominant production is called gluon-gluon fusion. The leading diagram for gluon-gluon fusion can be seen in Figure 1.2 *a*, where the Higgs is produced via a t or b quark loop. The second dominant process is Higgs production through Vector Boson Fusion (VBF) (Figure 1.2 *b*). The initial state is mostly from $u$ or $d$ quarks. The advantage of this process is the appearance of forward jets which are usually tagged in dedicated analyses. The third largest rate comes from production of a $W$ or $Z$ boson by two quarks with Higgs-strahlung (Figure 1.2 *c*). There is also associated

production of Higgs with a $t\bar{t}(b\bar{b})$ pairs, with the same initial state as in gluon fusion as Figure 1.2 *d* shows. The relevant couplings for Figure 1.2 *a* and Figure 1.2 *d* are the heavy-quark Yukawa coupling; And Figure 1.2 *b* and Figure 1.2 *c* are $WWH(ZZH)$ weak coupling. The cross-sections of those productions as a function of the Higgs mass are shown in Figure 1.3.

In principle, the Higgs can couple to fermions by the Yukawa coupling. The strengths of the couplings are proportional to the fermion mass. The SM Higgs therefore prefers to decay into $b\bar{b}$ or $\tau^+\tau^-$ rather than light quarks or leptons. The coupling of Higgs to $W$ and $Z$ with a normal weak strength is the other important contribution for Higgs decay. The Standard Model Higgs can not decay directly into two photons. But it can decay into two photons via a $b/t/W$ loop. The branching ratio of the decay is about 0.2% which can be seen in Figure 1.4 [17].

The LEP experiments have excluded a Higgs boson with mass blew 114.1 GeV at 95% confidence Level (see shaded area in Figure 1.5 [18]). In addition to setting an exclusion limit, LEP experiments also observed hints of a Higgs boson with a mass near 115 GeV [19]. A Higgs with mass $m_H > 260$ GeV is indirectly excluded at the 95% confidence level.

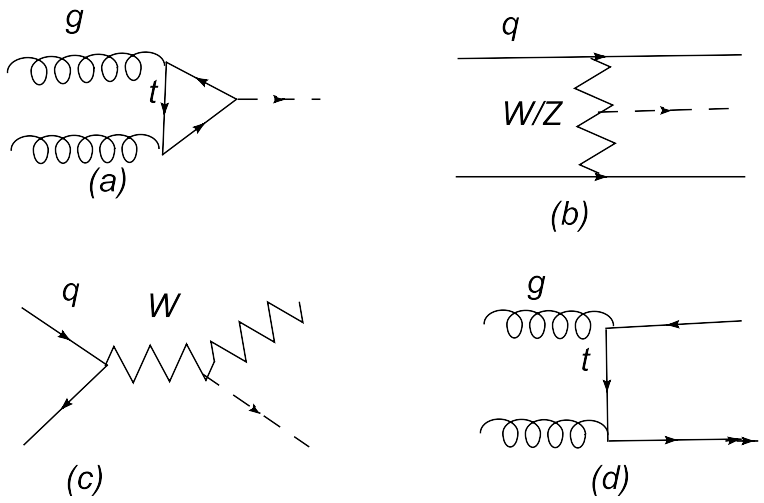


Figure 1.2: Feynman diagrams for Higgs production at the LHC. (a) gluon fusion (b) vector boson fusion (c) Associative production with W/Z. (d) production with a heavy quark pair.

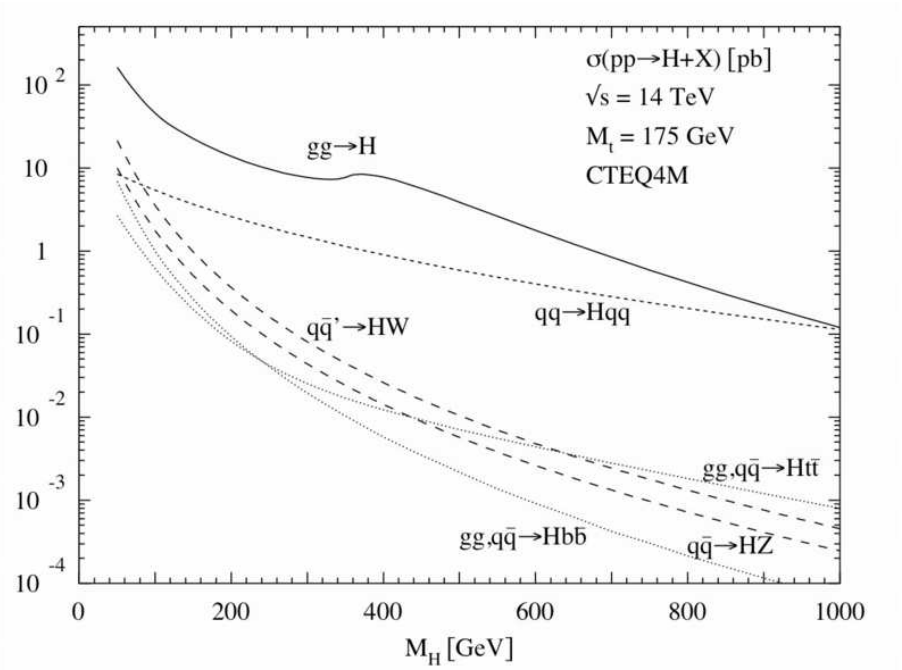


Figure 1.3: The cross-section for production of a Standard Model Higgs boson. The Figure is taken from M. Spira, Fortsch. Phys. 46 (1998).

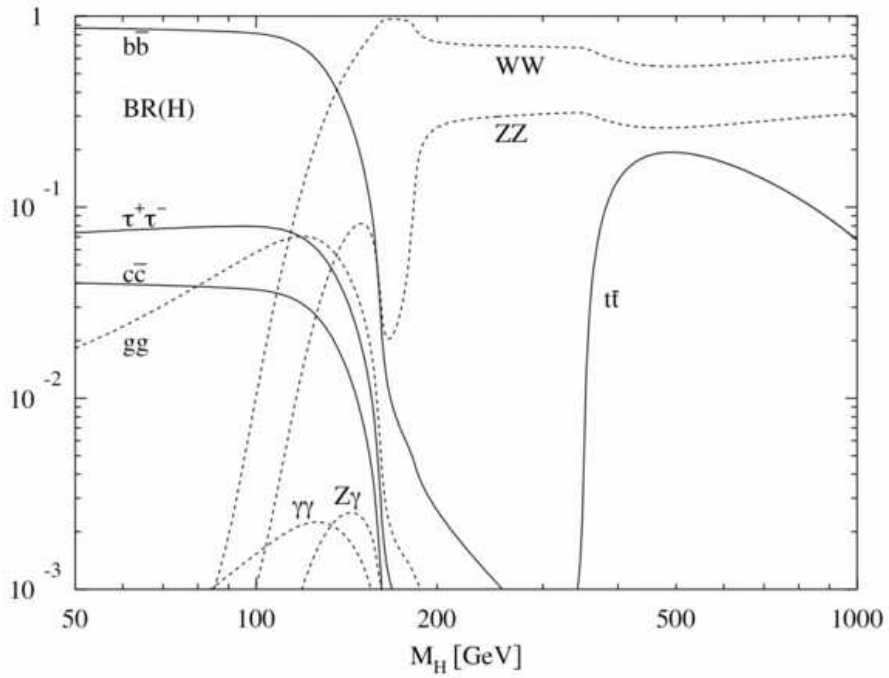


Figure 1.4: Higgs decay branching ratios. The Figure is taken from M. Spira, Fortsch. Phys. 46 (1998).

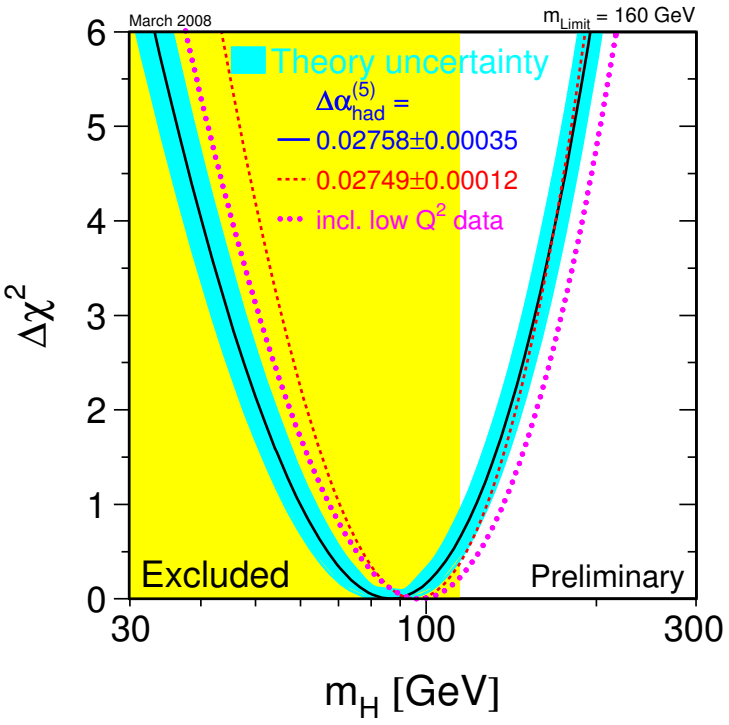


Figure 1.5: The LEP Higgs boson mass exclusion limit.

# Chapter 2

# The ATLAS Detector at the LHC

## 2.1 The Large Hadron Collider

The Large Hadron Collider (LHC) [20] is a proton-proton collider at European Organization for Nuclear Research (CERN). It is built in the 27 km tunnel where the LEP collider was situated and first collisions are expected in the fall of 2008. The collider has two opposing proton beams which have an energy of 7 TeV for each beam. This gives a total collision energy of 14 TeV. The beams move around the LHC ring inside a continuous vacuum guided by superconducting magnets which are cooled by a large and complex cryogenic system. The two counter-rotating beams collide and data is taken by four main LHC experiments: A Toroidal LHC ApparatuS (ATLAS), A Large Ion Collider Experiment (ALICE), the Compact Muon Solenoid (CMS) and the Large Hadron Collider beauty experiment (LHCb) as Figure 2.1 shows. The maximal luminosity the LHC can achieve will be close to $2 \cdot 10^{34} cm^{-2} s^{-1}$. However, due to stability concerns, the nominal luminosity will be fixed at $10^{34} cm^{-2} s^{-1}$. A standard year at the LHC is intended to allow total of running time $10^7 s$. Taking as an example a Standard Model 120 GeV Higgs particle, the NLO signal production cross-section

is 24.42 pb and the branching ratio for $H \rightarrow \gamma\gamma$ is 0.223% [21]. At $10^{34} cm^{-2} s^{-1}$, this will give about 900 events a year before taking any detection efficiency into account. Assuming that the photon efficiency is 80% per photon and the efficiency of the selection cuts is about 50%. This leaves roughly around 300 $H \rightarrow \gamma\gamma$ events after the first year.

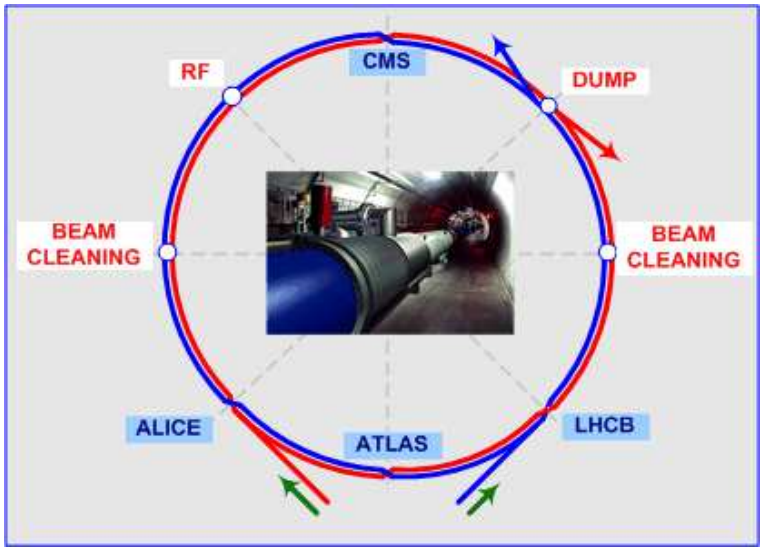


Figure 2.1: Four experiments ATLAS, CMS, ALICE and LHCb are positioned around the LHC collider ring. Two beams with accelerated protons will collide inside each of the detectors. Those four experiments will take the data.

## 2.2 The ATLAS Detector

Due to the high luminosity and increased cross-section provided by the LHC, ATLAS has the opportunity of precisely testing QCD, electroweak interactions and flavor physics. Beyond those, the goals of ATLAS consist of searching for a Standard Model Higgs boson, new heavy gauge bosons $W'$ and $Z'$, supersymmetric particles extra dimensions and other deviations from the SM. Those physics goals put stringent requirements on identification and measurement of photons, leptons, jets, b-tagging

and missing transverse momentum ($E_T^{miss}$), all with $P_T$ scales ranging from tens of GeV to several TeV. In proton-proton collisions, QCD jet production cross-sections dominate over those processes which will challenge the identification of experimental signatures characteristic of the physics process. The total inelastic $pp$ cross-section at $\sqrt{s} = 14$ TeV is about 80 mb. This translates to an average of 2.3 interactions per bunch crossing at low luminosity ( $\mathcal{L} \cong 10^{33} cm^{-2} s^{-1}$ ) or 23 interactions per bunch crossing at high luminosity ( $\mathcal{L} \cong 10^{34} cm^{-2} s^{-1}$ ) considering beam crossings are 25 ns apart. So each time a high $P_T$ event is produced, some additional soft events (pile-up) will overlap to the trigger one. The presence of the pile-up also has a major impact on the design of the readout electronics for the ATLAS detector especially for high luminosity.

ATLAS is one of the general-purpose detectors and is documented in detail in Refs [22, 23]. The overall view of the detector and coordinate system are summarized by Figure 2.2 and its text. For a completeness, a brief introduction of the ATLAS sub-detectors is described blew.

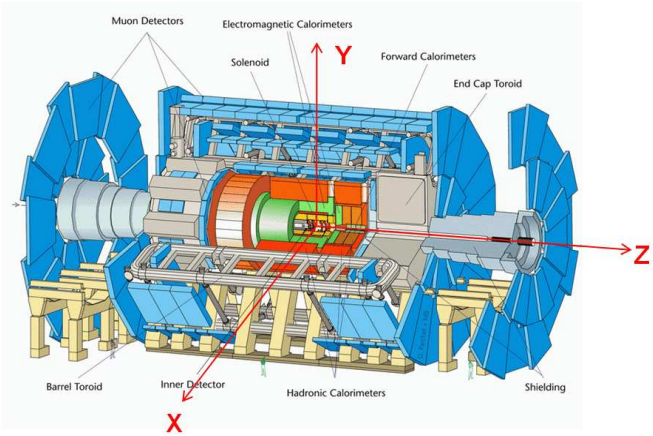


Figure 2.2: The overall layout of the ATLAS Detector. The z-axis is defined by the beam direction and the x-y plane is transverse to the beam direction. The positive x-axis is from the interacting point to the center of the LHC ring and the positive y-axis is defined as pointing upwards. The azimuthal angle $\phi$ is measured around the beam axis, and the polar angle $\theta$ is the angle from the beam axis. The pseudo-rapidity is $\eta = -\log(tan(\theta/2))$. The overall dimensions of the detector are 25 m in height and 44 m in length. The overall weight of the detector is approximately 7000 tonnes.

### 2.2.1 Inner Detector

The Inner Detector (ID) is immersed in a solenoid magnetic field of 2 T and is contained within a cylindrical envelope of length ±3512 mm and of radius 1150 mm as Figure 2.3 shows. It covers the region $|\eta| < 2.5$. Due to the track bending ability of the solenoid magnet, the ID provides a good measurement of the momentum of charged particles. It also allows the offline tagging of $\tau$-leptons and $b$-jets by the reconstruction of secondary vertices. Together with the electromagnetic (EM) calorimeter, it also provides important imformation for the identification of electrons and photons.

- The Pixel Detector (PD) has three different layers in the barrels with average radii of 4 cm, 10 cm and 13 cm and five end-cap disks on each side, positioned between 11 and 20 cm. The PD provides three precise measurements over the full acceptance and determines the impact parameter resolution and the ability of the Inner Detector to measure secondary vertices.

- The Semiconductor Tracker (SCT) measures the momentum, impact parameter and vertex position and provides good pattern recognition. It follows the PD and covers up to 56 cm from the base line. It uses eight layers of silicon microstrip to provide precision points in space.

- The Transition Radiation tracker (TRT) uses straw tubes, which can operate at very high rates and allow a large number of measurements. The radial range it can measure from 56 cm to 107 cm. Due to the use of xenon gas to detect transition-radiation photons created in a radiator between the straws, the

TRT provides a good electron identification capability. Moreover, by continuous tracking with a high occupancy and counting rate, good pattern recognition performance is assured.

### 2.2.2 Calorimeters

The Calorimeters of ATLAS are responsible for measuring photons, electrons, jets and missing $E_T$. As mentioned before, the calorimeters are also used to identify electrons and photons together with the ID. Moreover, based on calorimeter information, the Level 1 (LVL1) trigger will decide region-of-interest (RoI) events.

The calorimetry consists of 3 parts: an electromagnetic (EM) calorimeter covering $|\eta| < 3.2$, hadronic calorimeters covering $|\eta| < 3.2$ and forward calorimeters covering $3.1 < |\eta| < 4.9$. The view of the calorimeter is presented in Figure 2.4

The EM calorimeter uses lead as the absorber and liquid argon (LAr) as active material. It has electromagnetic barrel (EMB) covers a pseudo-rapidity range $|\eta| < 1.37$ and the end-cap (EMEC), covers the pseudo-rapidity range is from $1.52 < |\eta| < 3.2$. In all of them, it has a full azimuth acceptnace in the range $0 < \phi < 2\pi$. The EM calorimeter is segmented in longitudinal samplings: front (Sampling 1), middle (Sampling 2) and back (Sampling 3) as Figure 2.5 defines. For $|\eta| < 1.8$, there is also a presampler before the front sampling which is used to correct the energy lost upstream in the calorimeter.

The Hadronic Calorimeter is located outside of the EM calorimeter. It is designed to contain the hadronic shower and minimize the leakage of energy into the muon system.

The tile calorimeter has one barrel that covers $|\eta| < 1.0$ and two extended barrels

in the range $0.8 < |\eta| < 1.7$. It uses steel as the absorber and scintillating tiles as the active material. In total, there are three longitudinal segmentation layers inside tile calorimeter. A reasonable interaction length (e.g. $10\,\lambda$ at $|\eta| = 0$) ensures that it absorbs all the hadronic energy in the event and that it provides good resolution for high energy jets.

The LAr hadronic end-cap calorimeter is composed of two independent wheels for each end-cap and has some overlap with forward calorimeter to provide uniform material density at the transition region between end-cap and forward calorimeter. Each wheel consists of two longitudinal segments in total, four layers per end-cap. The inner wheels are built from 25 mm thick parallel copper plates, while the outer wheels are built from 50 mm thick copper plates. The copper plates are interleaved with 8.5 mm LAr gaps, providing the active material for the sampling calorimeter.

The Forward Calorimeter (FCal) is integrated into the end-cap cryostats to provide continuous coverage in high $\eta$ region as well as reduced radiation background levels in the muon spectrometer. The FCal consists of three modules in each end-cap: the first, made of copper, is optimized for electromagnetic measurements, while the other two, made of tungsten, measure mostly the energy of hadronic interactions. Again LAr is the active medium. The total interaction length is about $10\,\lambda$.

### 2.2.3 The Muon Spectrometer

The Muon spectrometer, as Figure 2.6 shows, provides precise muon measurement and a stand-alone local trigger system. Monitored Drift Tubes (MDT's) provides a precise measurement of the track coordinates. For larger pseudorapidites, Cathode Strip Chambers (CSC's) are employed to withstand the demanding rate and back-

ground conditions. In addition, Resistive Plate Chambers(RPC's) and Thin Gap Chambers(TGC's) serve as trigger chambers. The muon tracks are bent by toroid magnets. In the central region $|\eta| < 1.4$, the large toroid provides the magnetic field to deflect muon tracks. For $1.6 < |\eta| < 2.7$, magnetic bending is provided by two smaller end-cap magnets inserted into both ends of the barrel toroid. In the transition region $1.4 < |\eta| < 1.6$, magnetic bending is provided by the combination of barrel and end-cap fields.

### 2.2.4 The Magnet System

The ATLAS detector system is provided with two different kinds of magnetic fields ( Figure 2.7 ):

The central solenoid aligned on the beam axis and provides a 2T field for the inner detector.

Three large air-core toroids systems (two end-cap and one barrel) generate the magnetic field for the muon spectrometer. Each of the three toroids consists of eight coils assembled radially and symmetrically around the beam axis. In the barrel region, The barrel toroid provides 1.5 - 5.5 Tesla meters (Tm) of bending power. It is 1 to 7.5 Tm in the end-cap.

### 2.2.5 The Trigger and Data Acquisition

The trigger and Data Acquisition (TDAQ) systems, as Figure 2.8 shows, has three levels: L1, L2 and the event filter. Each level's decision is based on the data selected by the previous one and an additional selection criteria is applied, if necessary. The interaction rate is about 1 GHz (Bunching crossing rate 40 MHz). After the trigger

systems, the final rate is about 200 Hz with an event size of approximately 1.3 Mbyte.

The most difficult challenge for L1 trigger is that it should uniquely identify the bunch-crossing of interest in short time interval about 2.5 $\mu$s. Based on reduced-granularity information, L1 searches for high transverse-momentum muons, electrons, photons, jets and $\tau$-jets, as well as missing energy. As mentioned before, the trigger of high transverse-momentum muons are done by RPC and TGC. Furthermore, L1 also defines one or more Regions-of-Interest (RoI) for each event.

With RoI information provided by the L1 trigger over a dedicated data path, the L2 trigger selectively accesses data from readout buffers (ROBs) at full granularity and precision. The L2 menus are designed to reduce the trigger rate to approximately 3.5 kHz, with an event processing time of about 10 ms.

The last stage of the event selection is carried out by the event filter, which reduces the event rate to about 200 Hz. This selection are applied with offline analysis. The average processing time is on the order of seconds.

### 2.2.6 The Simulation of ATLAS detector

Simulation has played a key role in designing the ATLAS detector. The full simulation of ATLAS detector is performed with GEANT. From 2004, ATLAS has converted from FORTRAN-based GEANT3 to GEANT4 which is written in C++ after extensive validations [24]. From then up to now, the detector simulation has migrated from Data Challenge 2 (DC2) to Computing System Commissioning (CSC), where the latter has a detector geometry with more material budget, in particular one more layer in the inner detector. This thesis is mostly based on CSC. The material distribution in the ID can be seen from photon conversion mapping as Figure 2.9

shows. In CSC, there are three different geometries[1]:

- ideal0 data processed with geometry ATLAS-CSC-01-00-00. First digit refers to magnetic field, second to geometry and last to version. This one means "new magnetic field, perfect geometry".

- misal1 data processed with geometry ATLAS-CSC-01-02-00. This one means "new magnetic field, misaligned geometry with material distortions" as Figure 2.10 shows.

- misalg data processed with geometry ATLAS-CSC-01-01-00. This one means "new magnetic field, misaligned geometry without material distortions".

The chain of full simulation has 4 steps: process generation, detector simulation, digitization and reconstruction. Generation refers to the production of particles from specific physics process. The results are saved as four-vectors. There are many generators available, e.g. the generations for gg Fusion $H \rightarrow \gamma\gamma$ can be produced with PYTHIA [25], ALPGEN [26], HERWIG [27] and MC@NLO [28, 29]. Simulation is then the process that passes generated events through a GEANT4 simulation of the ATLAS Detector to produce the GEANT4 Hits which record the particle information when it transverses the detector. In order to mimic the raw data from the real detector, the response of the detector to the hits is simulated in the so called "digitization" which induces information such as voltages, times etc. Finally, the digitized output is reconstructed into tracks, energy, etc., using the same reconstruction algorithms that will be applied to real data. The output from the reconstruction is called Event

[1]https://twiki.cern.ch/twiki/bin/view/Atlas/InDetGeometryVersions has detail definition of the convention.

Summary Data (ESD). Essentially, the users can work on the ESD. However, the ATLAS computing model recommends that users work with a reduced data format called Analysis Object Data (AOD). Geant4 as part of the ATLAS offline software is fully integrated in the ATLAS framework for the offline event processing called ATHENA [30].

Full Simulation is necessary for the study of tracking performance, energy, missing ET resolution, photon conversion, electron/photon/muon/tau identification, jet clustering etc.

However, a fast simulation [31] is needed in order to model huge reducible backgrounds (e.g. QCD multi-jets and $\gamma$-jets for $H \rightarrow \gamma\gamma$ analysis.). Fast simulation (Atlfast) replaces the full simulation and reconstruction phases by smearing the MC truth information directly with resolutions measured from full simulation studies. The diagramatic illustration is shown in Figure 2.11.

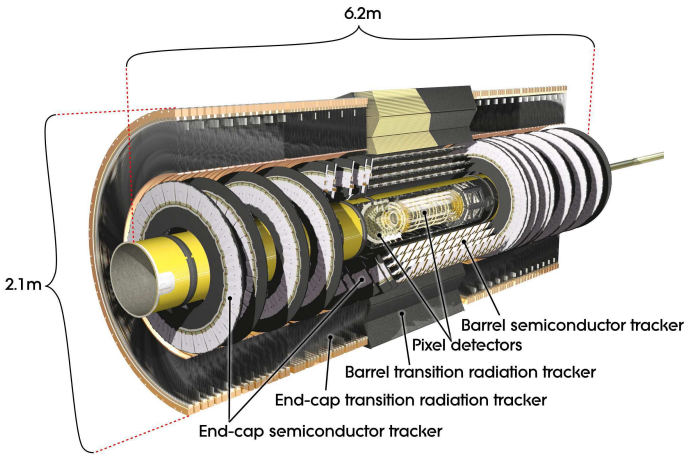


Figure 2.3: Cut-away view of the ATLAS inner detector

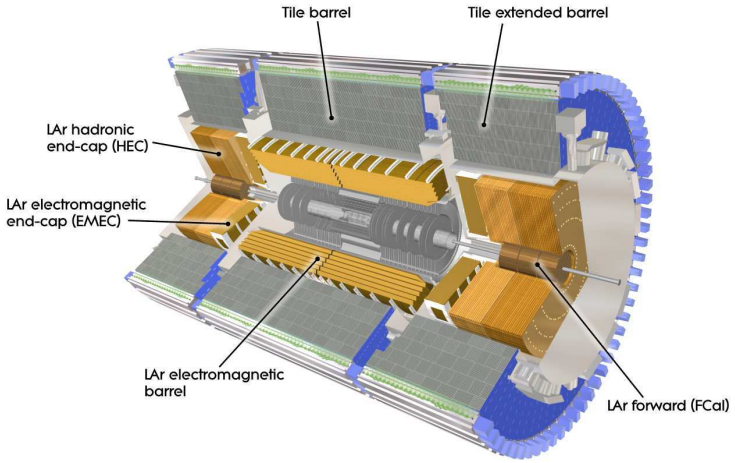


Figure 2.4: Cut-away view of the ATLAS calorimeter

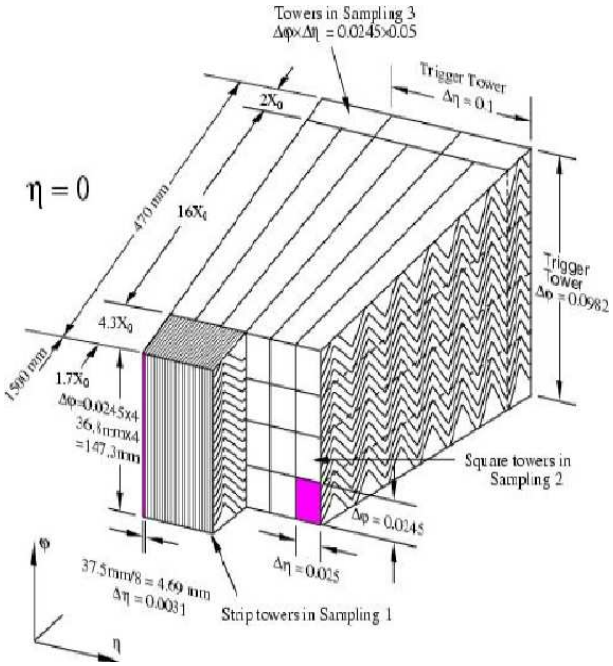


Figure 2.5: The segmentation of EM calorimeter Barrel

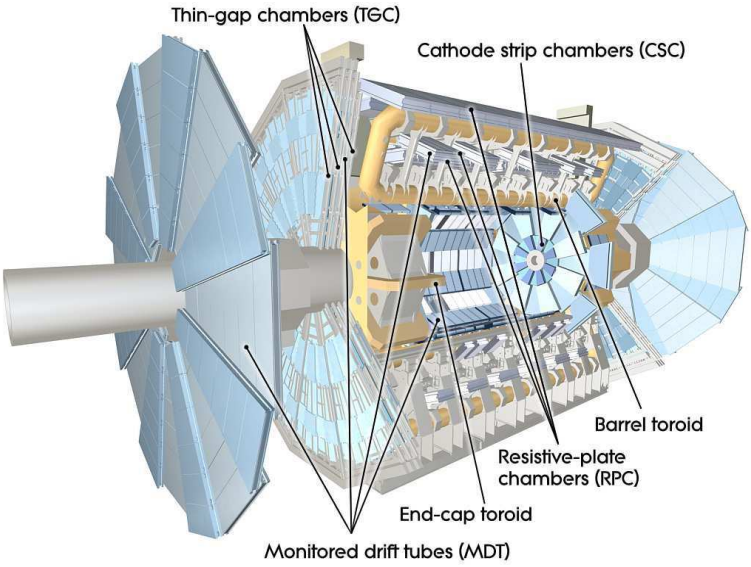


Figure 2.6: Cut-away view of the Muon detector

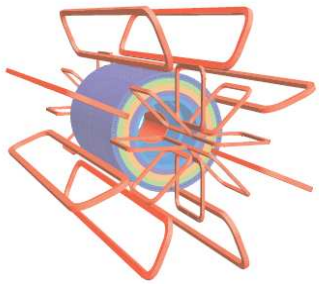

Figure 2.7: View of the ATLAS magnet system. The central cylindrical coil of the superconducting solenoid is surrounded by toroids in the barrel and end-cap regions

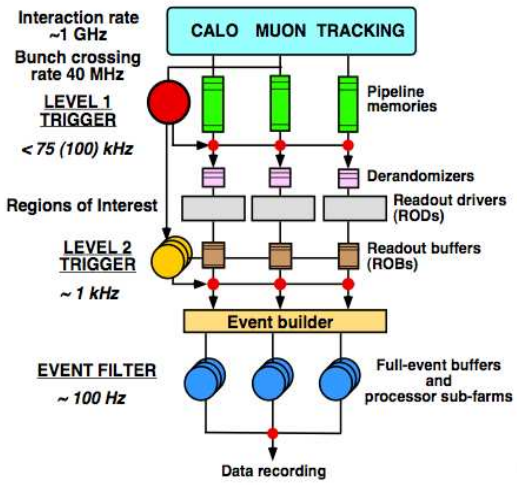


Figure 2.8: The schematic description of the ATLAS trigger system

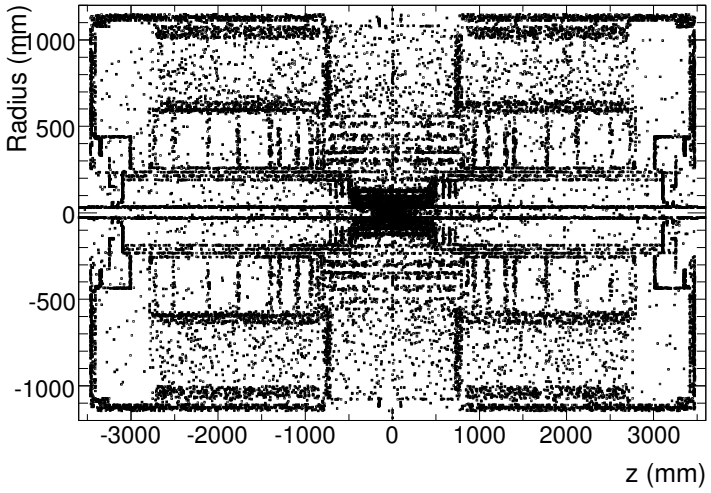


Figure 2.9: The mapping of photon conversions as a function of z and radius, integrated over $\phi$ for the ID. It is based on 57000 converted photons from PhotonJet sample.

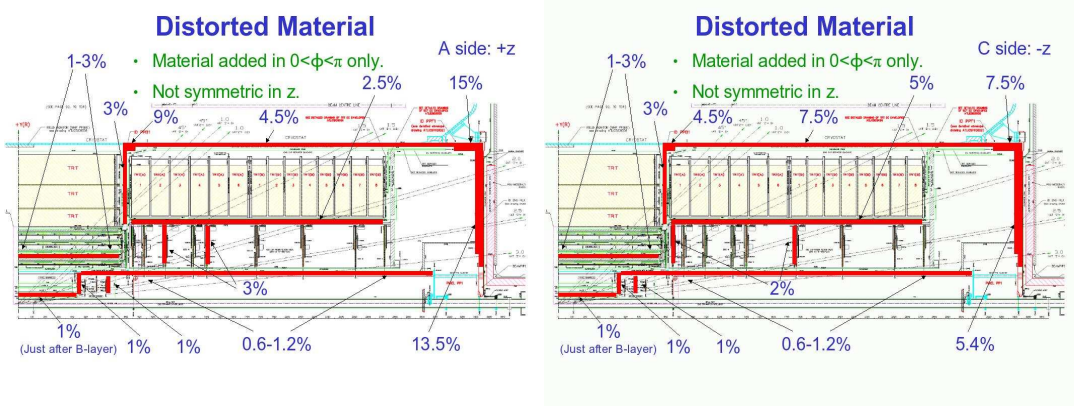


Figure 2.10: Distorted material distribution. The plots show the location of the extra material added and the amount is in the percent of radiation length. The left plot is in the +z direction, the right one is in the -z direction.

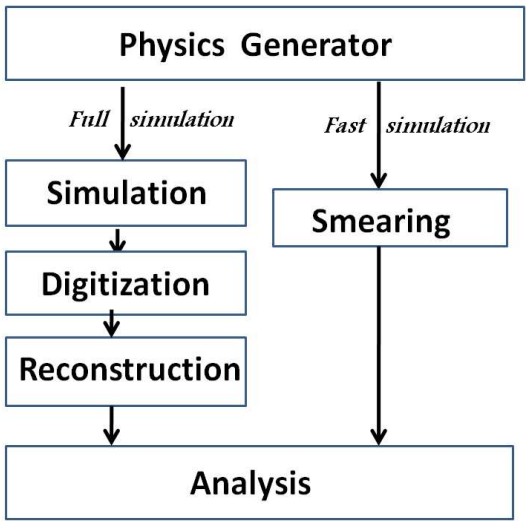


Figure 2.11: A schematic overview of the simulation of ATLAS

# Chapter 3

# Photon calibration with Longitudinal weights

One of the challenges for the $H \rightarrow \gamma\gamma$ channel is that it requires good energy and angular resolution to achieve about 1% resolution in Higgs mass reconstruction. Hence, understanding of the calorimeter response such as electrons' or photons' resolution and linearity has been one of the main goals of ATLAS Liquid Argon Calorimeter Test-Beams and early data analysis [32].

For the calibration of photons for ATLAS, the issue one will face is the large amount of inactive material upstream of the Liquid Argon (LAr) electromagnetic calorimeter (EMC). The upstream material causes conversion of photons and the pre-showering of the produced electrons. Since the distribution of upstream material in ATLAS is $\eta$ dependent, it is reasonable for a calibration to take into account this dependency.

In this chapter, a photon-based calculation of longitudinal weights for the ATLAS Electromagnetic Calorimeter is performed. In ATLAS, there exists reconstruction algorithms based on topological clusters [33] and fixed window clusters. Weights for

both of them are computed.

## 3.1 Cluster Level $e/\gamma$ Correction in ATHENA

The basic unit of granularity storing energy in EM Calorimeter is called a cell. The dimension of a cell is $\Delta\eta \times \Delta\phi = 0.025 \times 0.025$. The collection of the cells around the barycenter of the shower in the middle compartment is called a cluster. In ATHENA (see Section 2.2.6), there are two types of clusters: one is of fixed window size such as 3x3, 3x5, 3x7 in $\Delta\eta \times \Delta\phi$. The other one is called the topological cluster, which groups cells into clusters based on their neighbor relations and on the significance of their energy contents.

Before discussing the longitudinal weights, it is helpful to give an overview of the cluster level $e/\gamma$ corrections in ATHENA.

- S-shape correction: corrects the reconstructed $\eta$ coordination of an EM Cluster. The definition of a cluster position is : $\frac{\sum_{i=1}^{n} E_i X_i}{\sum_{i=1}^{n} E_i}$ where $X_i$,$E_i$ are the position and energy of the cell respectively. Due to the finite size of the EM Calorimeter, a shift of the cluster towards the center of a cell is known as S-shapes in the measurement of the cluster position.

- $\phi/\eta$ Modulation: Correction of the cell energy response to an incident particle varies due to the variation of the amount of passive material in the $\phi/\eta$ direction.

- $\eta 1/\phi 2$ position correction: Corrects the cluster position along the $\phi$ or $\eta$ direction.

- Lateral leakage correction: This is the correction of out of the clustering cone.

- Longitudinal correction: As mentioned in Chapter 2, the EM calorimeters are longitudinally segmented in four layers. The energy loss upstream and downstream can be parameterized with weighted energies with the presampler and the last layer. The parameterization is supposed to be $\eta$ dependent due to upstream material.

## 3.2 Monte Carlo Sample Production

A large amount of MC samples have been generated for the purpose of this study. The files are described in Table 3.1. All files include underlying event and electronic noise.

Single-photon events have been studied to extract the calibration constants. These events were generated according to the following criteria:

- Single photons with energy ranging from 20 GeVto 1TeV(as Table 3.1 shows) are generated using ATHENA 12.0.31 and rebinned with 100 $\eta$ bins from 0.0125 to 2.4875.
- Simulation using Atlsim 02-32-10.
- Filters in the particle level filter at $|\eta| < 2.7$,$P_T > 20$ GeV (for 2 photons) are applied for $H \rightarrow \gamma\gamma$ samples.
- Cuts in the simulation at $|\eta| < 2.5$ for two photons are applied.
- Reconstruction using ATHENA 12.0.6. Electronic noise in the CALO was switched on. Low luminosity pile-up was applied for the $H \rightarrow \gamma\gamma$ sample.

| Channel | Run Number | Events | Detector Geometry |
|---|---|---|---|
| Single $\gamma(20GeV)$ | 7082 | 49K | 01-00-00 |
| Single $\gamma(50GeV)$ | 7062 | 45K | 01-00-00 |
| Single $\gamma(75GeV)$ | 7083 | 48K | 01-00-00 |
| Single $\gamma(100GeV)$ | 7063 | 40K | 01-00-00 |
| Single $\gamma(200GeV)$ | 7084 | 44K | 01-00-00 |
| Single $\gamma(500GeV)$ | 7085 | 45K | 01-00-00 |
| $H(120GeV) \rightarrow \gamma\gamma$ | 5310 | 45K | 01-00(01)(02)-00 |
| $H(130GeV) \rightarrow \gamma\gamma$ | 6307 | 45K | 01-00(01)(02)-00 |
| $H(140GeV) \rightarrow \gamma\gamma$ | 6308 | 45K | 01-00(01)(02)-00 |

Table 3.1: Fully Simulated and Reconstructed MC files used in this study. The detector geometries are described in section 2.2.6.

## 3.3 Investigation of Photon Conversion

The interaction between the upstream material and photon causes the photon conversion into $e^+e^-$ pair. The photons' lifetime can be described as:

$$N_\gamma = N_{0,\gamma} \cdot e^{\frac{-\Delta x}{\lambda_{INT}}}. \tag{3.1}$$

the interaction length $\lambda_{INT}$ is defined as:

$$\lambda_{INT} = A/(N_A \sigma_{INT}) \tag{3.2}$$

and

$$\sigma_{INT} \approx 7A/(9N_A X_0) \tag{3.3}$$

where A is the average atomic mass, $N_A$ is Avogadro's number, $X_0$ is the radiation length which depends on the material of the medium photons travel, $N_{0,\gamma}$ is the number of the initial photons, $N_\gamma$ is the number of survived photons from conversion after traveling $\Delta X$ distance. It is clear that:

$$N_\gamma / N_{0,\gamma} = e^{\frac{-\Delta x}{9X_0/7}} \tag{3.4}$$

which means that if a photon travels $1/2X_0$, there is a 23% chance that it converts. Figure 3.1 shows the material thickness distribution in $X_0$ versus pseudo-rapidity from the interaction point to the face of the EM calorimeter in ATLAS which can help the understanding of photon conversion. Figure 3.2 displays the conversion rate versus the pseudo-rapidity in ATLAS. This plot is consistent with the previous one and the conversion rate is roughly independent of the photon energy. The Inner detector provides tagging ability for the those early converted photons by reconstructing the tracks of converted $e^+$ $e^-$ from photons. Figures 3.3 shows the relation between the tagging of converted photons and the conversion radius of photons. The tagging efficiency decreases w.r.t the converted radius because the track of earlier converted photons are easier to reconstruct. An algorithm to tag converted photons using one or two tracks has been developed in ATLAS [34]. The addition of back-tracking will help the tagging for converted photons of large radii [35].

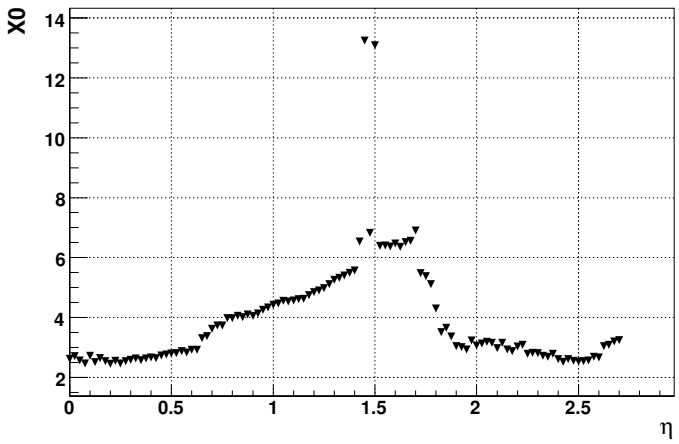


Figure 3.1: Amount of material (in $X_0$) in front of the ATLAS EM Calorimeter as a function of pseudo-rapidity.

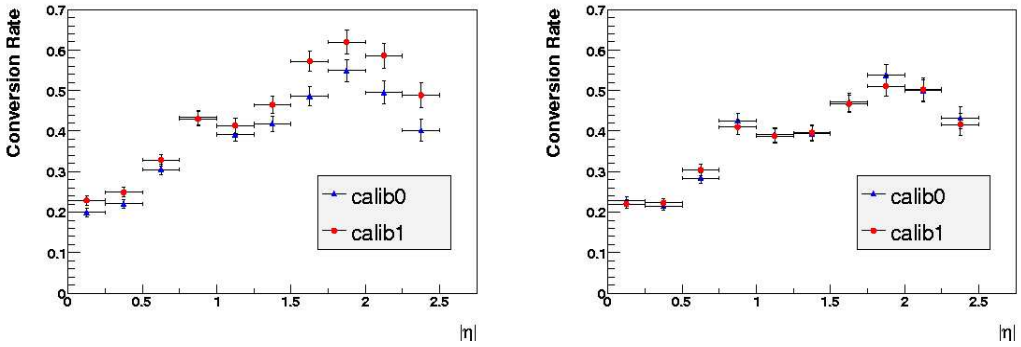


Figure 3.2: Photons' conversion rate with respect to pseudo-rapidity. The left plot is for $0 < \phi < \pi$, the right plot is for $-\pi < \phi < 0$. calib0 means perfect geometry, calib1 has misalignment + more material geometry as described in Section 2.2.6.

## 3.4 Longitudinal Weights for the LAr EM Calorimeter's Photon Calibration

In the current combined ntuple (CBNT) or AOD files, photon variables from both fixed window cluster blocks and topological cluster blocks are available. Figure 3.4-3.6 show the mean fractional energy deviation from the truth and corresponding resolutions. A comparison of photons' energy reconstructed by 3x7 3x5 and topological cluster are given in Figure 3.7. As seen from the plot, the topological cluster, due to its multi-cluster energy collection, has the best behavior for the same sampling. For the unconverted photon, the 3x5 and 3x7 clusters are reasonably consistent. For the late converted photon, the tails between 3x5 and 3x7 clusters are still not very significant. However in the case of early converted photons, the 3x5 reconstructed clusters have longer tails than those of 3x7. This happens because that the converted $e^+$ $e^-$ spreads wider in the $\phi$ direction due to the magnetic field in the Inner Detector.

For the calculation of the longitudinal weights, a modified parameterization is

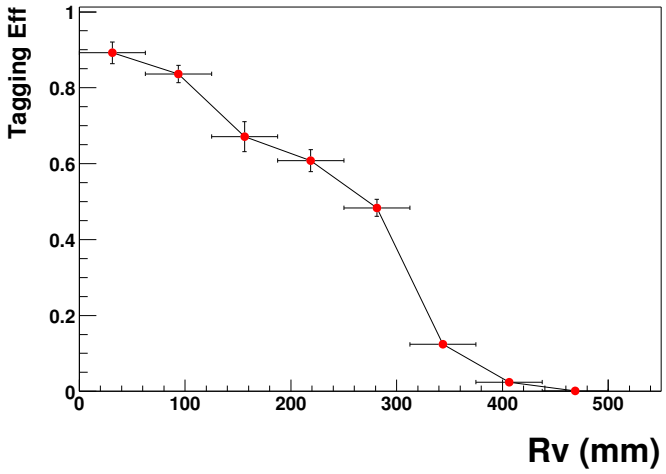


Figure 3.3: tagging efficiency for converted photons vs the radius of conversion

applied for the energy reconstruction:

$$E_{rec} = \lambda(b + W_0 E_{pres} + E_1 + E_2 + W_3 E_3). \tag{3.5}$$

where b is an offset which can help to improve the photon energy linearity and resolution. The weight $W_0$ is used to correct the energy deposit in the presampler. The weight $W_3$ for the third sampling is supposed to correct the longitudinal leakage. In the range $|\eta| > 1.8375$, there is no presampler, $W_0$ is set to 0. Calibration constants in the crack range $1.37 < |\eta| < 1.52$ are not reliable.

The longitudinal weight calculation approach used here consists of the following steps:

- perform calibration based on single photons shooting from the center of the ATLAS detector with $\eta$ from 0.0125 to 2.4875 at a step of 0.025;
- using the elecron-photon block of the CBNT, calculate the constants for 3x7,

3x5 and topological clusters.

- truncate non-gaussian tails with respect to $\eta$ around the center of the distribution.

- perform minimization of a function for all clusters belonging to a specific $\eta$ bin. Here $\Sigma\frac{(E_{rec}-E_{true})^2}{\sigma^2}$ is minimized, where $E_{rec}$ is the reconstructed energy, $E_{true}$ is the generated photon energy and $\sigma$ is the calorimeter resolution parametrization.

The resulting longitudinal weights for topological, 3x5 and 3x7 clusters are shown in Figure 3.8, Figure 3.9 and Figure 3.10, respectively. The evaluation of the calibration for the same samplings can been seen in Figure 3.11, Figure 3.12 and Figure 3.13.

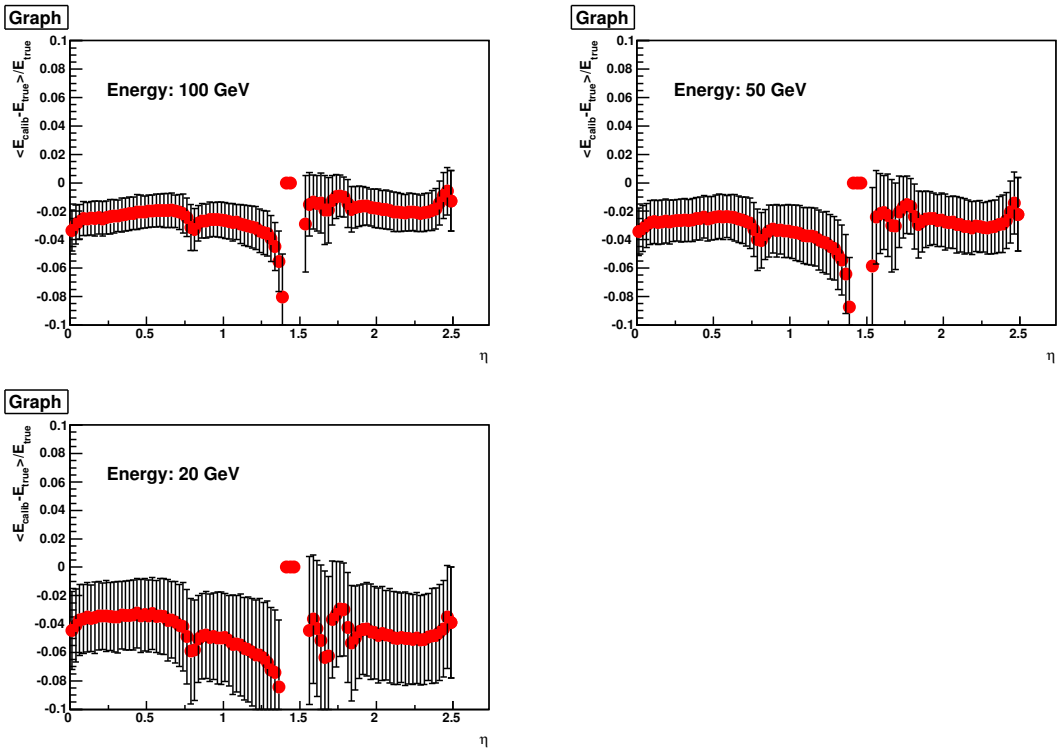


Figure 3.4: Mean fractional energy deviation from truth(data points) and energy resolution (error-bars) for photons as a function of $\eta$ before any calibration, for topological clusters

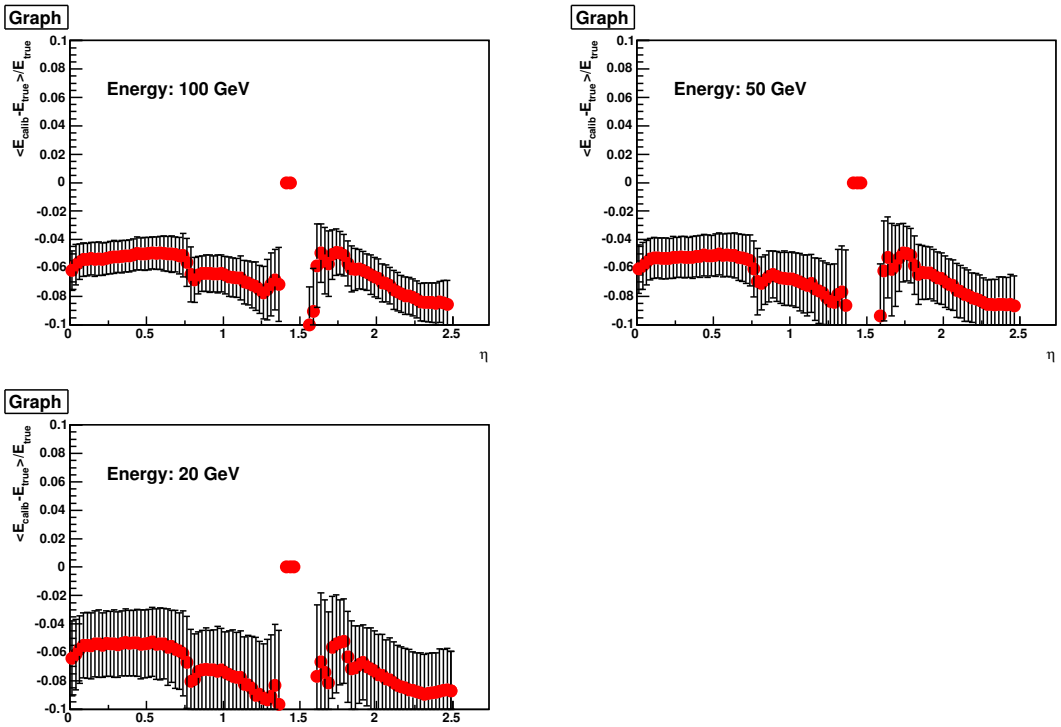


Figure 3.5: Mean fractional energy deviation from truth(data points) and energy resolution (error-bars) for photons as a function of $\eta$ before any calibration, for clusters reconstructed within 3x5 cell fixed window algorithm.

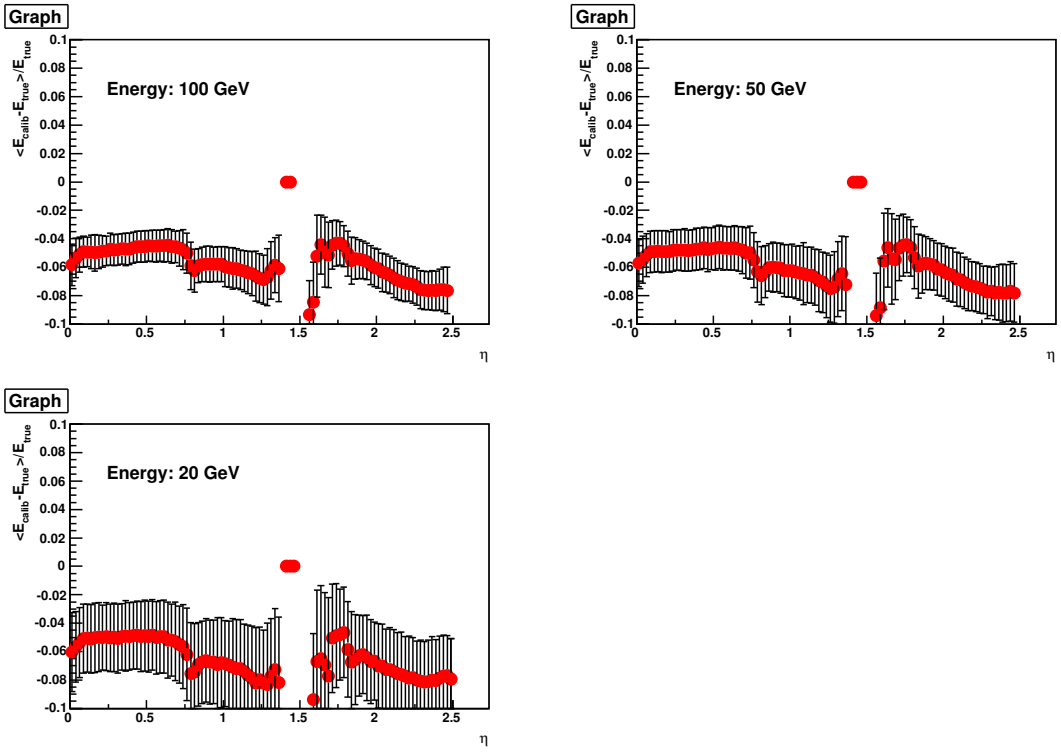


Figure 3.6: Mean fractional energy deviation from truth(data points) and energy resolution (error-bars) for photons as a function of $\eta$ before any calibration, for clusters reconstructed within 3x5 cell fixed window algorithm.

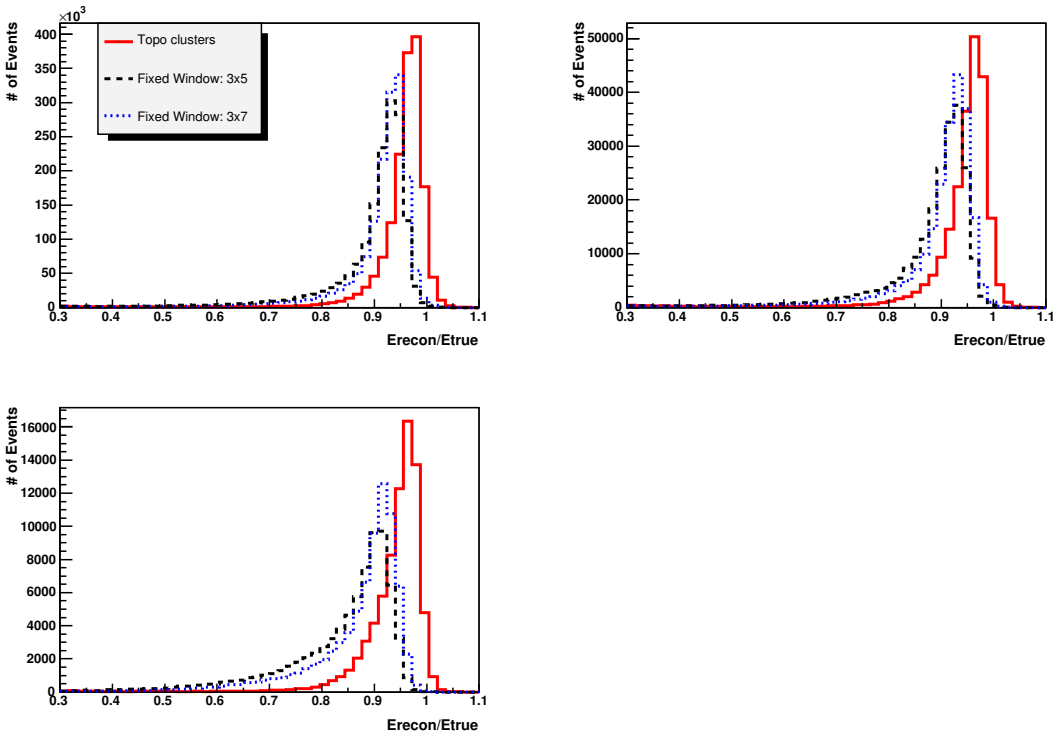


Figure 3.7: Histogram distribution of the ratio between reconstructed photon energy and generated photon energy. The upper left is for unconverted photons, the upper right is for later converted photons with the conversion radius $R > 350mm$. The bottom one is for the case of early converted photons. For each plot, 3x7, 3x5, and topological clusters are used.

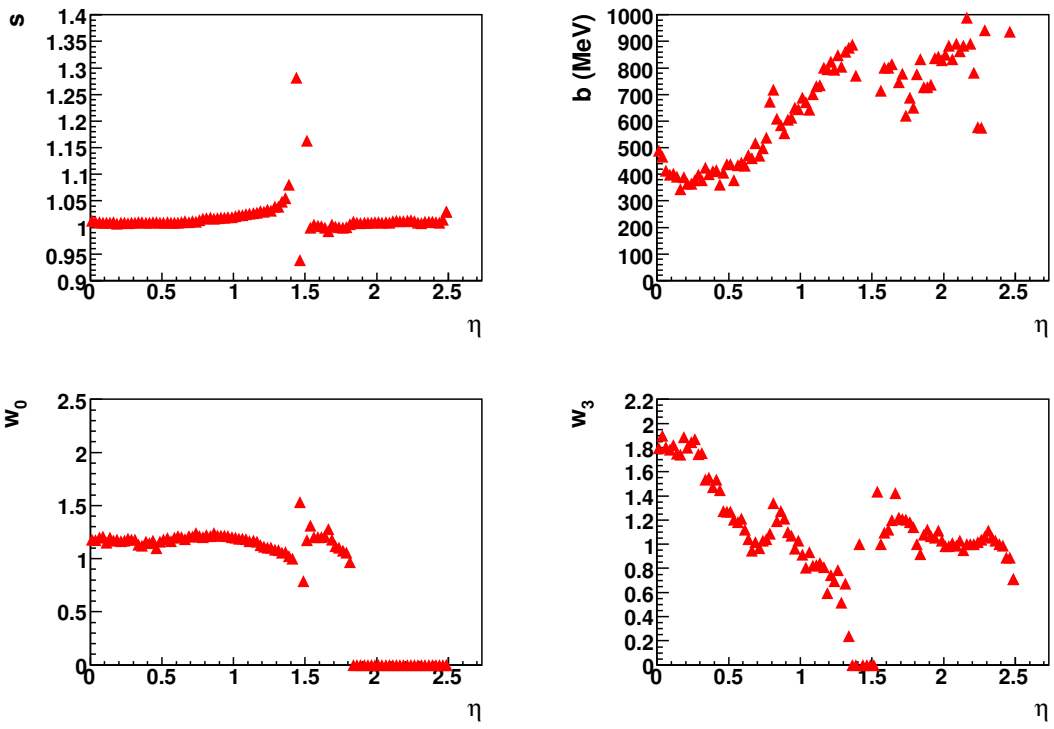


Figure 3.8: Constants of photon calibration for topological clusters. The upper left plot is for scale factor $\lambda$, the upper right plots offset b$\times$1000, the bottom left is $W_0$ and bottom right is $W_3$.

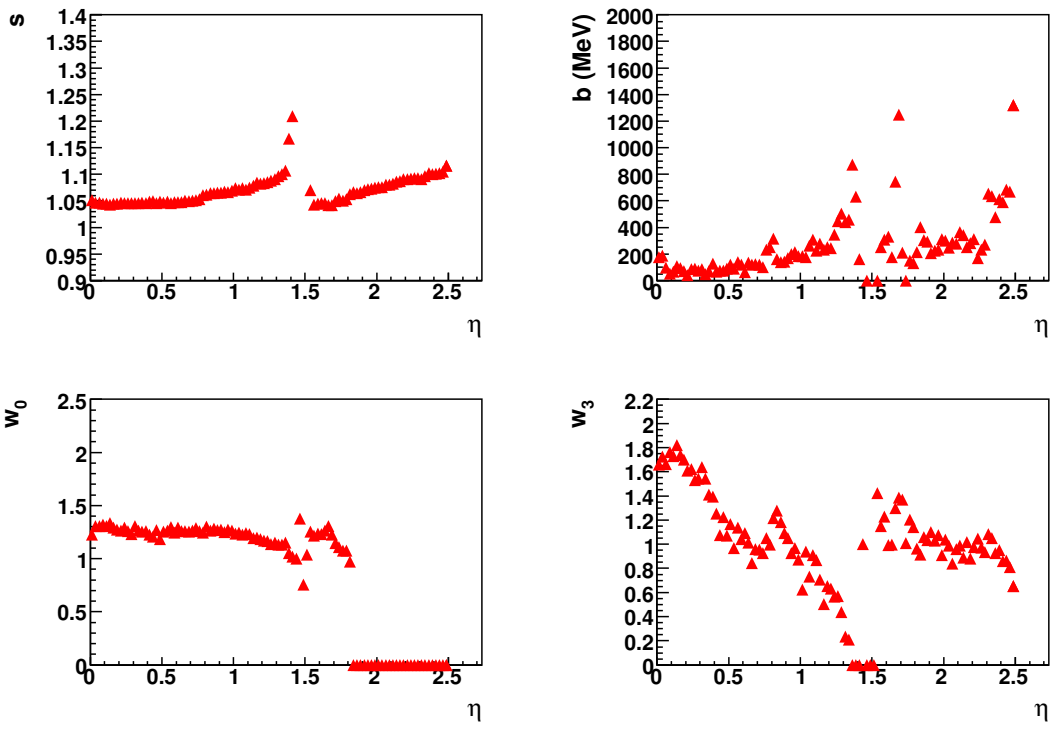


Figure 3.9: Constants of photon calibration for fixed window 3x5. The upper left plot is for scale factor $\lambda$, the upper right plots offset b$\times$1000, the bottom left is $W_0$ and bottom right is $W_3$.

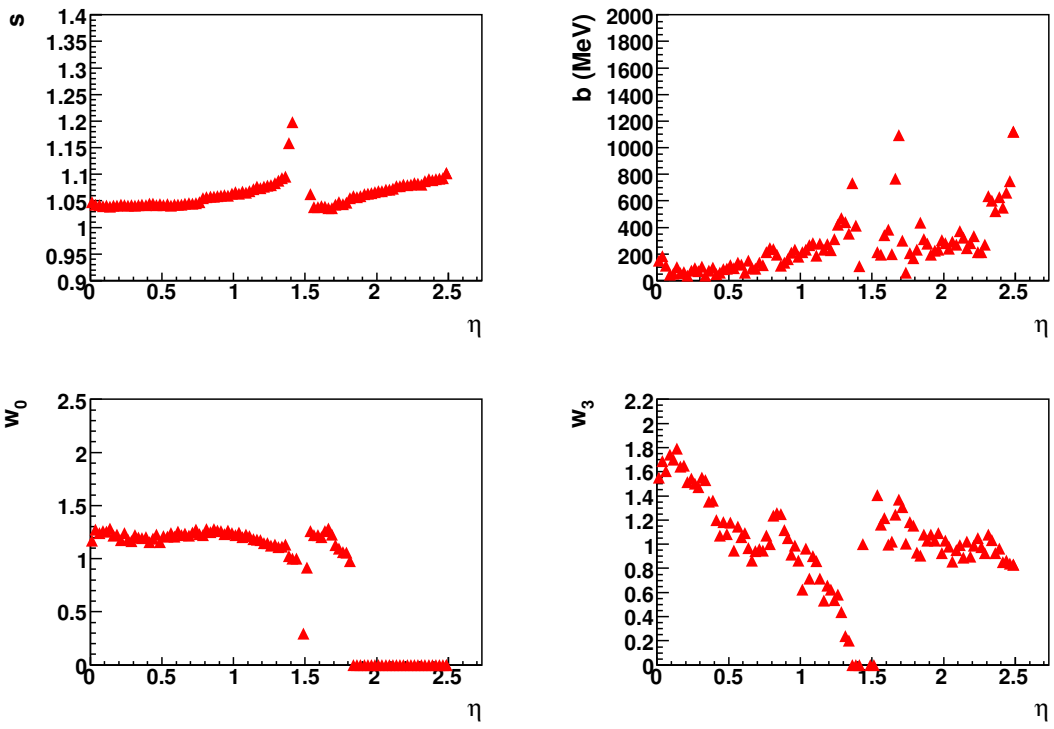


Figure 3.10: Constants of photon calibration for fixed window 3x7. The upper left plot is for scale factor $\lambda$, the upper right plots offset b$\times$1000, the bottom left is $W_0$ and bottom right is $W_3$.

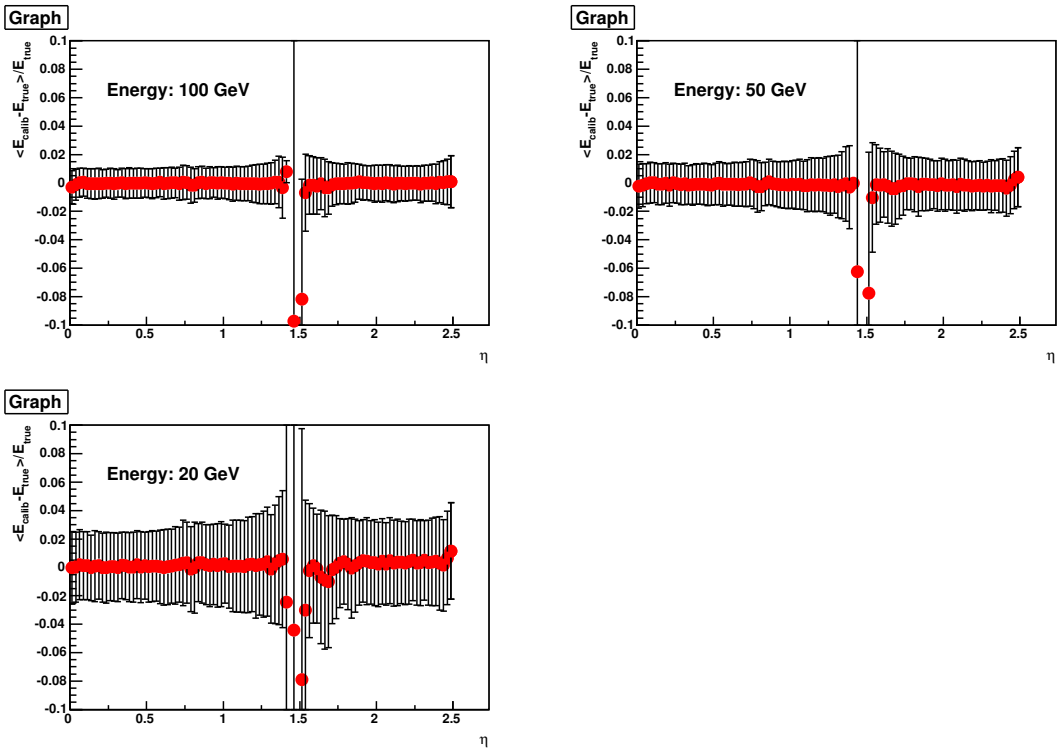


Figure 3.11: Evaluation of photon calibration for different energies in the case of topology clusters 6.3.0, where the center of each bin is the mean of $\langle E_{calib} - E_{true} \rangle / E_{true}$, while the error bar is the sigma from $\langle E_{calib} - E_{true} \rangle / E_{true}$.

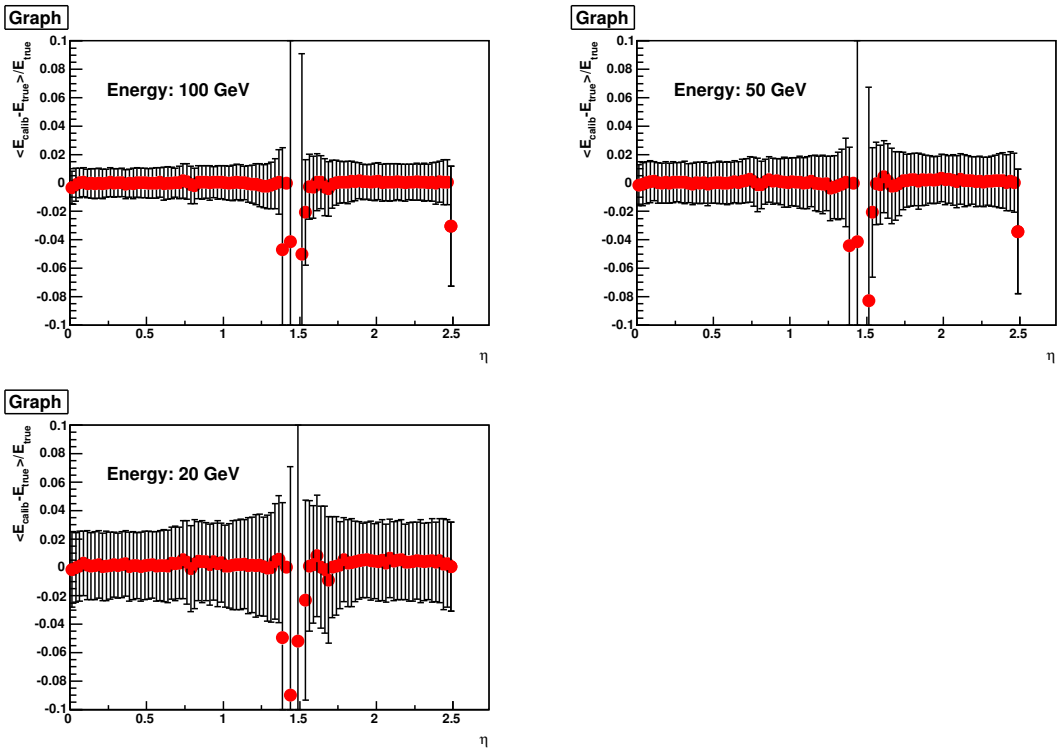


Figure 3.12: Evaluation of photon calibration for different energies in the case of fixed window 3x5 where the center of each bin is the mean of $\langle E_{calib} - E_{true} \rangle / E_{true}$, while the error bar is the sigma from $\langle E_{calib} - E_{true} \rangle / E_{true}$.

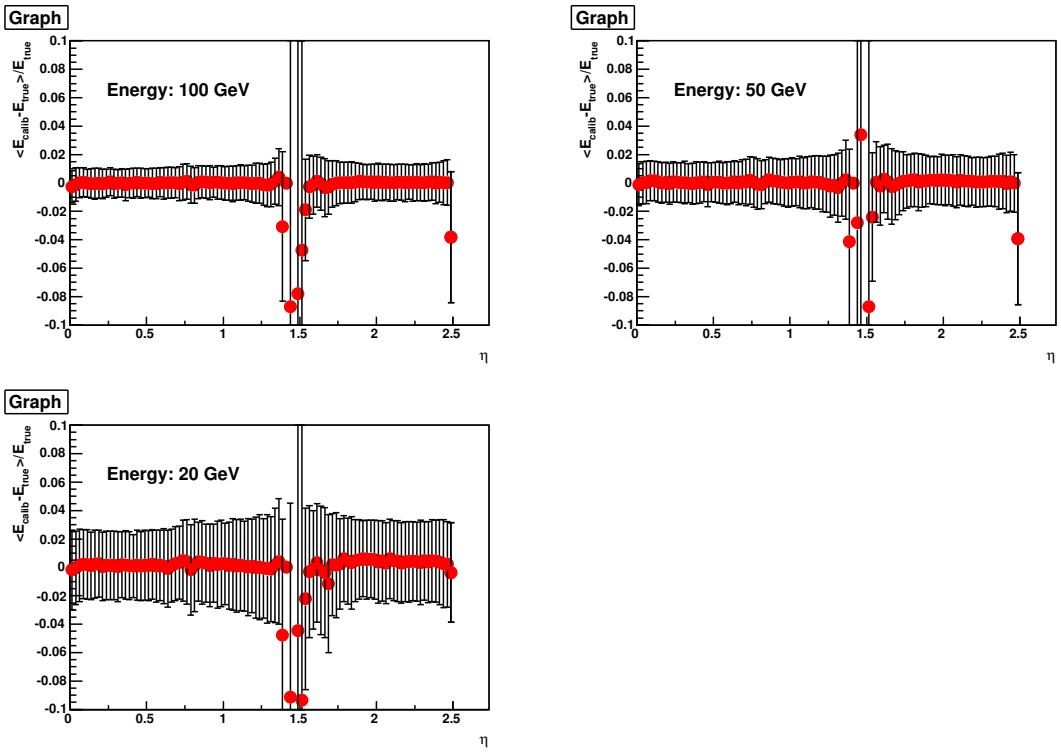


Figure 3.13: Evaluation of photon calibration for different energies in the case of fixed window 3x7 where the center of each bin is the mean of $\langle E_{calib} - E_{true} \rangle / E_{true}$, while the error bar is the sigma from $\langle E_{calib} - E_{true} \rangle / E_{true}$.

## 3.5 Vertex correction and its application to the mass reconstruction of two photons

The equation for the mass of two photons is:

$$m_{\gamma\gamma} = \sqrt{2E_{\gamma 1}E_{\gamma 2}(1 - cos(\Delta\theta_{\gamma 1\gamma 2}))} \tag{3.6}$$

where $E_{\gamma 1}, E_{\gamma 2}$ are the energies of photons from Higgs decay, $\Delta\theta_{\gamma 1\gamma 2}$ is the angles between two photons. From equation 3.6, it is obvious that the related angular variable is the $\Delta\theta_{\gamma 1\gamma 2}$ distribution between the two photons into which Higgs decays . Here, precise measurements of $\Delta\theta_{\gamma 1\gamma 2}$ as well as the photons' energies are fundamental for Higgs reconstruction.

The reason why we introduced vertex correction is that the assumption that the interaction occurs at the origin of the ATLAS coordinate system is not always true. In reality, quite a few primary vertices in the events varied from the origin o to o' as Figure 3.14 describes. In practice, the beams have been smeared as Figure 3.15 shows. One can see that the correction is mostly from Z vertex correction. In other word, instead of calibrating the energy of photon, the vertex correction procedure corrects the angular variables $\phi$ and especially $\theta$ as described in Chapter 2 to finally improve the resolution of the Higgs mass distribution.

A linear fit is applied on the event primary vertex and barycenters of shower centers of different layers to estimate the photon direction. In addition, a likelihood method has been developed to reduce the impact from pile-up.

The results for the correction can be found in the thesis [36].

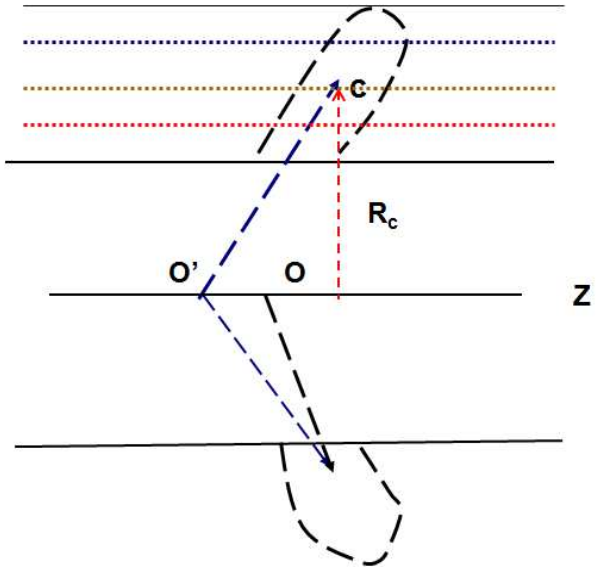


Figure 3.14: The projected description of primary vertex. The point o is the standard interaction point(IP). o' is the corrected o, Z is the axis of beam line and c is the shower center in calorimeter. $R_c$ is the radius of shower center.

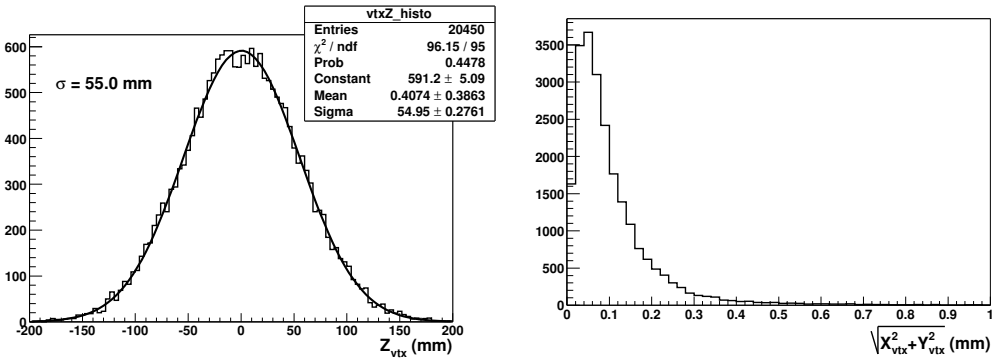


Figure 3.15: True Z and R vertex distribution.

## 3.6 Conclusions

In this chapter, a photon-based calculation of longitudinal weights for ATLAS Electromagnetic Calorimeter (Barrel and Endcap) and a vertex correction were performed. The improvement in the resolution and linearity for photons due to the calibration was demonstrated. The reconstructions of Higgs with calibration and vertex for a few masses are shown in Figure 3.16. The results are also summerized in Table 3.2. The final resolution $\sigma/m_H$ achieves about 1.1% which is the requirement for this channel.

| | No Pileup | | $10^{33}$ $s^{-1}cm^{-2}$ | |
|---|---|---|---|---|
| Higgs Mass ( $GeV/c^2$) | Mass ( $GeV/c^2$) | $\sigma/m_H$ (%) | Mass ( $GeV/c^2$) | $\sigma/m_H$ (%) |
| 120 | 119.6 | 1.1 | 119.5 | 1.2 |
| 130 | 129.6 | 1.1 | 129.5 | 1.2 |
| 140 | 139.5 | 1.1 | 139.5 | 1.1 |

Table 3.2: The reconstructed invariant mass peaks and resolutions for different Higgs masses using misaligned and distorted geometry samples with and without $10^{33}$ $s^{-1}cm^{-2}$ pileup.

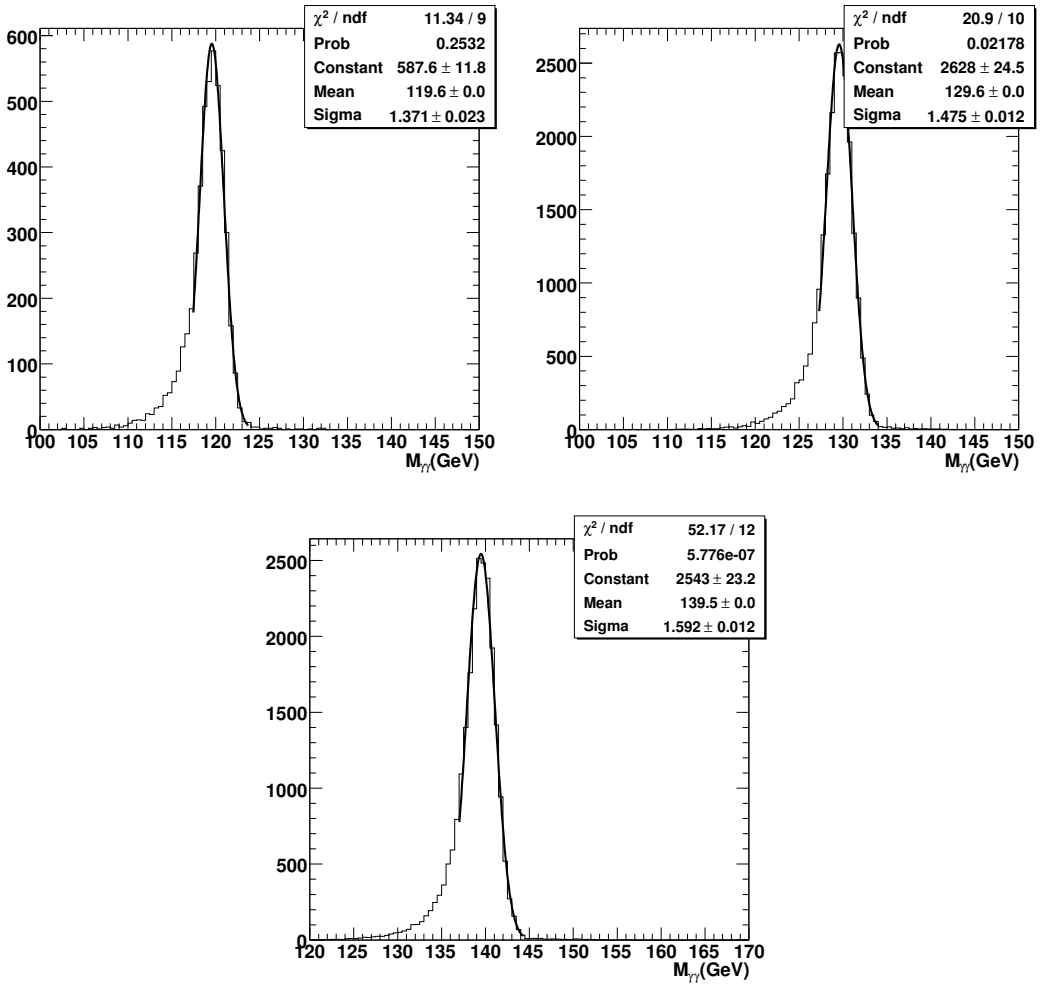


Figure 3.16: The reconstructed invariant mass using misaligned and distorted geometry without pileup. The upper left plot is the one with mass 120 GeV. The upper right plot is the one with mass 130 GeV. The bottom one plots the invariant mass distribution with 140 GeV.

# Chapter 4

# Photon identification and jet rejection

Photon/Jet separation for $E_T > 25$ GeV is essential for the $H \rightarrow \gamma\gamma$ channel. The $\gamma$-jets, which is dominated by the quark initiated jets, constitutes most of reducible background. Since the cross-section of the $\gamma$-jet process is at the level of 100 nb, a rejection of at least 1000 is required in order to obtain a reasonable signal significance.

From DC2 to the CSC layout (see Section 2.2.6), the Inner Detector (ID) geometry has been significantly modified. Two more layers have been added to the ID. Also, extra material has been added to EM calorimeter. The inner detector change can affect mostly the conversion of photons.

## 4.1 Reconstruction and analysis

The Monte Carlo events were generated and filtered with PYTHIA 6.4 under the framework of ATHENA and stored in CBNT format. Monte Carlo events were fully simulated and digitized and reconstructed with GEANT4. The events are reconstructed with 12.0.6. Tuned underlying event was used.

### 4.1.1 Data Sets used

In this study, the binned $\gamma$-jet samples are summarized in Table 4.1.

| samples | $E_T$ range | Filter Efficiency | $\sigma$ | events | dataset |
|---|---|---|---|---|---|
| $\gamma$-jet1 | $17-35$ GeV | 0.57 | 1.49E5 | 390K | 8095 |
| $\gamma$-jet2 | $35-70$ GeV | 0.68 | 1.88E4 | 330K | 8096 |
| $\gamma$-jet3 | $70-140$ GeV | 0.82 | 1.00E5 | 290K | 8097 |

Table 4.1: Data samples used, $E_T$ range is on the hadronic level where $\sigma$ is the cross-section after filter (unit pb) The filter is defined as $|\eta_\gamma| < 2.7$ and $P_{T\gamma}$ >10 GeV.

$H \rightarrow \gamma\gamma$ ($M_H = 120$ GeV) has been used as a benchmark sample for medium $P_T$ photons and with pile-up of $10^{33} cm^{-2} s^{-1}$. The rejection studies for di-jet were conducted using a pre-filtered, highly electromagnetic jet sample with $P_T > 17$ GeV. The total number of di-jet events used in rejection studies was around 1000000.

## 4.2 $\gamma$/jet separation criteria

Jets and photons have different behaviors in the calorimeters and inner detector tracking systems. In order to distinguish photons from jets, discriminating variables based on the leakage of EM showers into the Hadronic Calorimeter and the shower shape in the first and second compartments of the EM Calorimeter are reconstructed. These variables were also used in previous studies [37, 38, 39]. With them, there are a few different methods to approach the aim of separating photons and jets.

The variables used are defined as following:

i. Hadronic leakage: This variable is defined as the transverse energy leaked in the first sampling of the hadronic calorimeter over the transverse energy in the the EM calorimeter. This cut is motivated by the fact that photons deposit little

energy in the hadronic calorimeter, typically less than 1 percent of their electromagnetic energy. The leakage in the first sampling in the hadronic calorimeter is measured by using a window of size $\Delta\eta \times \Delta\phi = 0.2 \times 0.2$. Figure 4.1 shows the distributions for photon and jet at low luminosity.

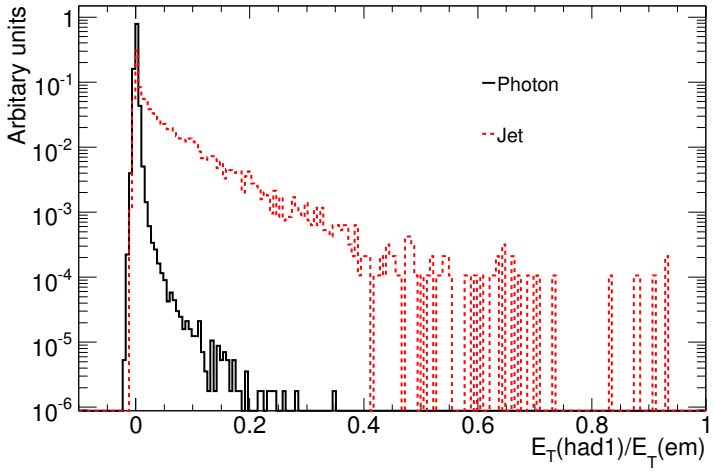


Figure 4.1: The ratio between transverse energy deposit in the hadronic calorimeter and transverse energy in the EM calorimeter. The black solid line is for photons, the red dotted line is for jets.

ii. Variables reconstructed using the second sampling of the calorimeter

- shower shape in $\eta$ direction. Photons deposit most of their energy in 3x7 clusters, while a jet has a wider shower in the EM calorimeter. So the ratio between $E_2(3\times7)$ and $E_2(7\times7)$ as shown in Figure 4.2 can help distinguish the photon from jet.
- Shower width in the $\eta$ direction. The width is calculated by summing weighted energy in the cells of 3x5 cluster. This of course depends on the particle impact point inside the cell. The width for photons and jets is shown in Figure 4.3.

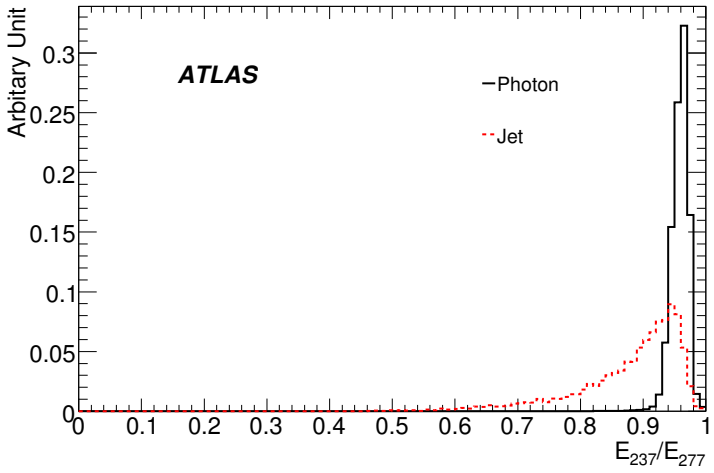


Figure 4.2: The energy deposit in 3x7 cluster divided by that in 7x7 cluster.

iii. Second sampling calorimeter variables

- Second maximum energy deposited in the second sample. A $\pi^0$ can decay into two photons. In this case, two maxima will be found in the second sampling. In order to reject these events, the variable $\Delta E = E_{2max} - E_{min}$, where $E_{min}$ is minimum energy found in the valley between the two maxima. This variable is shown in Figure 4.4. Variable $E_{2max}/(1 + 0.009 \times E_t)$ is also reconstructed as Figure 4.5 shows.

- Total shower width. This width is the weighted sum of energy with a window of granularity $\Delta\eta \times \Delta\phi = 0.0625 \times 0.2$. The expression is $\omega_{tot1} = \sqrt{\Sigma E_i \cdot (i - i_{max})^2 / \Sigma E_i}$ where i is the strip number and $i_{max}$ is the strip of the first maximum as Figure 4.6 shows.

- Fraction of energy outside the shower core in $\eta$. This variable, as Figure 4.7 shows, is the fraction of energy in 7 strips minus the energy deposited in 3

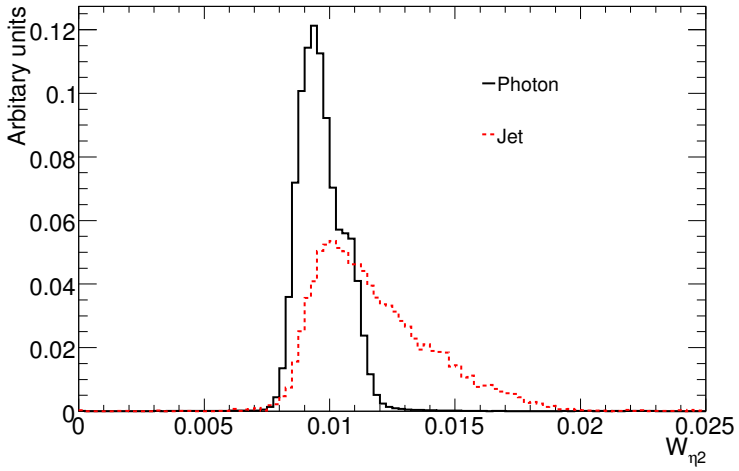


Figure 4.3: Shower width in $\eta$ direction which is calculated by 3x5 cluster.

strips over the energy in 7 strips.

- Shower width calculated using three strips around the one with maximal energy deposit. The formula is $w_{3strips} = \sqrt{\Sigma E_i \cdot (i - i_{max})^2 / \Sigma E_i}$ It is shown in Figure 4.8.

iv. Track isolation : The variable defined for track isolation is the sum of $P_T$ of all tracks with $\Delta R$ between the track at the vertex and cluster smaller than 0.3. Tracks with $P_T < 1$ GeV are ignored because they originate from the underlying events. For tracks with $\Delta R < 0.1$, some additional cuts are applied to remove conversions tracks from the sum:

- the impact parameter must be less than 0.1mm;
- number of hits on b-layer (barrel region of the Pixel Detector) must be larger than 0;
- the track $P_T$ must not exceed 15 GeV in order to remove the contribution

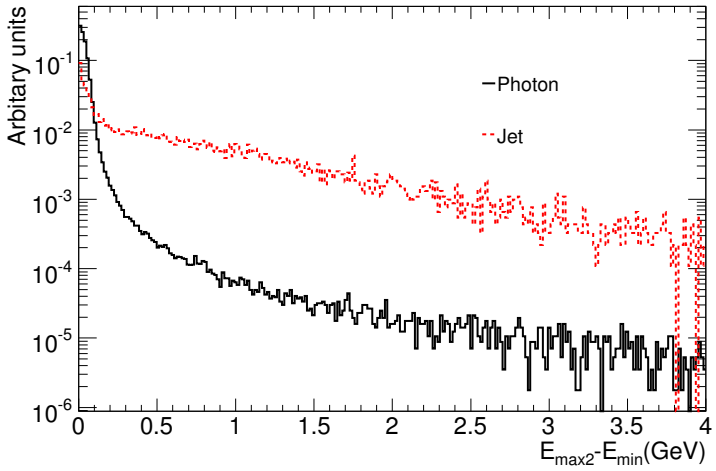


Figure 4.4: The energy of second maximum in the second sample minus the minimum between the first and second maximum

from very asymmetric conversions;

- the track is not a part of a conversion vertex.

Figure 4.9 shows the variable of the sum of $P_T$ of qualified tracks. Generally speaking, variables related to different features of photons interacting with the detector will have low correlations. Table 4.2 lists the correlations among the discriminating variables. The hadronic leakage (a) and sum of $P_T$ of qualified tracks (j) have weak correlations with the other variables. Furthermore, variables reconstructed from the first sampling don't have very strong correlations with those reconstructed from the second sampling. The identification will be more efficient if the chosen variables are less correlated.

### 4.2.1 Introduction of Photon identification method at ATLAS

So far, three photon identification algorithms have been developed in ATLAS [40]: the cut-based algorithm, the Log-likelihood Ratio based algorithm (LLR) and the co-

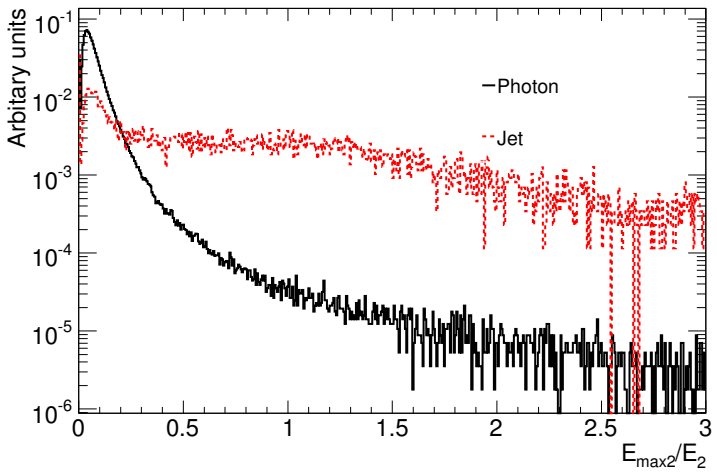


Figure 4.5: The energy of second maximum in the second sample divided by a fraction of cluster energy.

variant matrix based algorithm which is still under development.

For the cut-based algorithm, cuts on the variables introduced in Section 4.2 have been developed to maintain high photon efficiency.

The Log-likelihood Ratio algorithm first constructs the probability density function (PDF) for signal and background with the same discriminating variables used in the cut-based algorithm. Then for a photon or jet candidate, a likelihood ratio for it to be a photon over a jet is computed. Finally, one cut is applied on the likelihood ratio.

The covariance Matrix Based Photon Identification Method also uses similar shower shape variables and energy deposited in different layers of the EM calorimeter. Using those variables, a covariant matrix, M is constructed. For each photon/jet candidate, a $\chi^2$ is computed and a cut can be applied on it [40].

In order to ensure consistency among all three algorithms, the algorithm studies have agreed on definitions of efficiencies and rejections, as well as which Monte Carlo

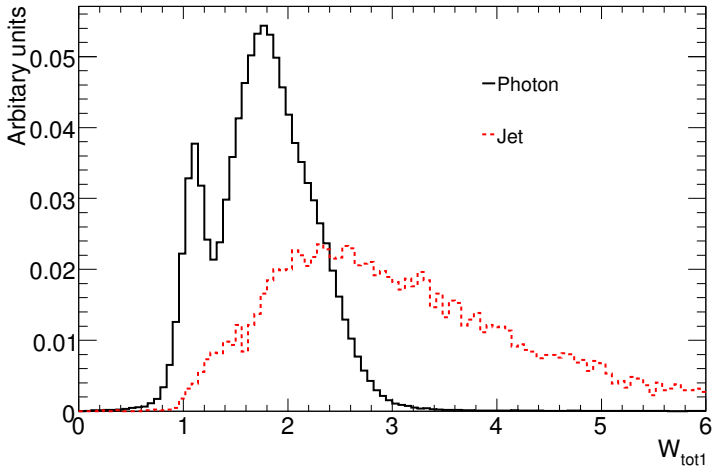


Figure 4.6: The total width calculated in the second sampling.

samples are used. The base sample criteria are as follows:

- Truth match: The reconstructed photons must be within $\Delta R = \sqrt{\Delta\eta^2 + \Delta\phi^2} <$ 0.2 of the MC truth photons resulting from the Higgs particle.

- The reconstructed photons must be in the pseudo-rapidity $0 \leq |\eta| \leq 1.37$ or $1.52 \leq |\eta| \leq 2.37$ to avoid detector cracks or uncovered geometric region.

Using the base samples that satisfy the above requirements, we define the efficiencies as follows:

$$\epsilon = \frac{N_\gamma^{reco}(\Delta\ R(Truth - reco) < 0.2 * fiducial * E_T^{truth} > 25(40)GeV * PhotonID)}{N_\gamma^{truth}(fiducial * E_T^{truth} > 25(40)GeV)} \tag{4.1}$$

The rejection is defined as follows:

$$R = \frac{N_{jet}}{N_{fake\gamma}} \frac{N_1}{N_2} \frac{1}{\epsilon_{\gamma-filter}} \tag{4.2}$$

where $N_{jet}$ is the total number of jets in the normalization sample. $N_{fake\gamma}$ is the number of fake photons in the reconstructed sample with the candidates that matched

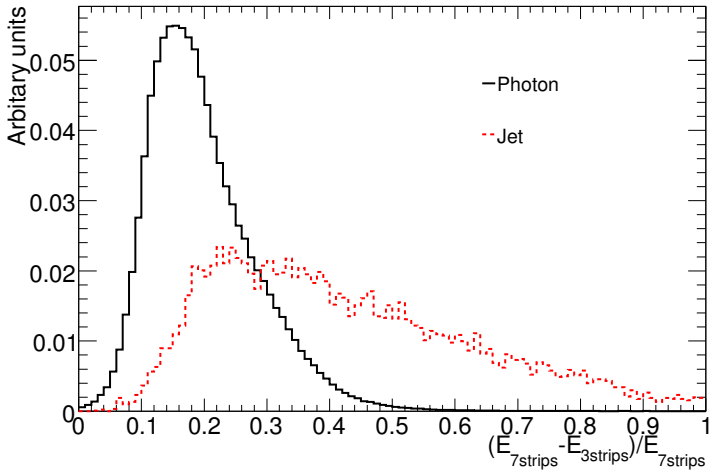


Figure 4.7: Fraction of energy deposited in 7 strips minus the energy deposited in 3 strips normalized to the energy in 7 strips.

to true photons from matrix element or quark bremsstrahlung removed. $N_1$ is the number of events analyzed from the sample. This number of di-jet for the studies is 3,095,900. $N_2$ is the number of di-jet events used in the normalization sample and is 400,000. The values for $N_{jet}/N_2$ in the fiducial volume of $|\eta| < 1.37$ or $1.52 < |\eta| < 2.37$ are 0.226 for jets with $E_T > 25$ GeV and 0.042 for jets with $E_T > 40$ GeV. $\epsilon_{\gamma-filter}$ is the efficiency of the high EM filter applied to 5802 and is 8.2% [41]. True photons (either from the hard process or from bremsstrahlung) are removed from the fake candidates in computing rejection factors.

The formula for the rejection of $\gamma$-jet is essentially similar. However, due to the fact that the samples are binned with $P_T$ at hadronic level and the cross-section for each individual sample significantly decreases according to the $P_T$, the numbers such as $N_{jet}$, $N_{fake\gamma}$ need to weighted w.r.t its cross-section.

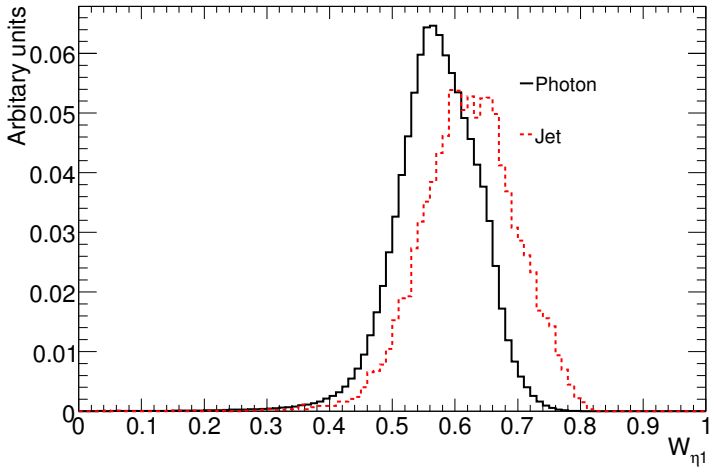


Figure 4.8: Shower width over 3 strips. The middle one is the strip with maximal energy.

### 4.2.2 $\gamma$/jet separation with Likelihood ratio method

In the likelihood ratio method, the distribution of the shower shape variables are normalized to unity to obtain the probability density function (PDF). The shower shape variables are pseudo-rapidity dependent, hence, we separate them with several intervals as shown below:

- $|\eta| \leq 0.8$;
- $0.8 < |\eta| \leq 1.37$;
- $1.52 < |\eta| \leq 2.0$;
- $2.0 < |\eta| \leq 2.37$.

The motivation of dividing variables into $\eta$ bins is due to the level of the granularity and the material in front of the electromagnetic calorimeter as a function of pseudo-rapidity. The crack regions $1.37 < |\eta| \leq 1.52$ and $|\eta| > 2.37$ are excluded due

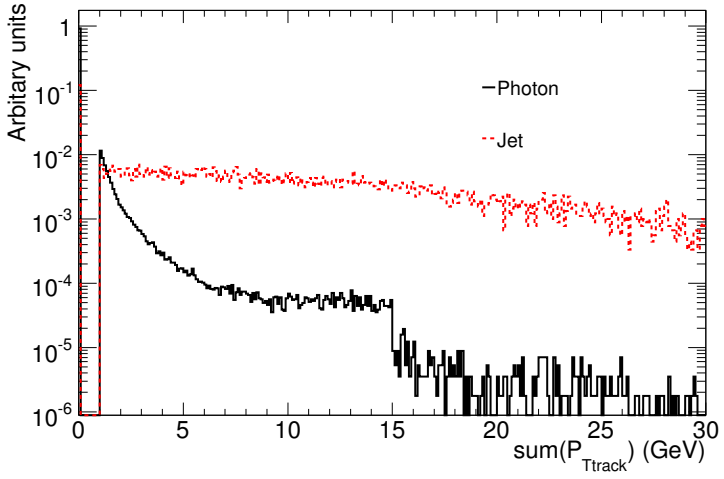


Figure 4.9: Track isolation variable, which is the sum of $P_T$ of the tracks as defined before. For the cut-based analysis, a typical cut a 4 GeV is applied.

to the fact that there are no strips in the first sampling layer within these two eta regions. Since the PDF also has a $P_T$ dependency, three $P_T$ bins (20-35 GeV, 35-70 GeV and 70-140 GeV) are implemented. In total, there are 4 eta bins and 3 $P_T$ bins, and each bin has 8 sets of PDF's for the eight variables used in this algorithm. So far, the $\gamma$-jet PDF is obtained using 1.6 million $\gamma$-jet events. The statistics is slightly low due to the fact that the samples have been separtated into quite a few bins while constructing PDFs. One improvement can made through the use of KEYS [42], which is a statistic tool, can be used to estimate probability for low statistics and smooth the PDF. Using the PDF of a specific shower shape variable, one can compute the likelihood ratio of a photon or jet candidate being a photon over a jet (to follow the convention, logarithm of this ratio is used in this study). After going through through all eight variables for each object, ratios are summed up to give the likelihood of the

| | a | b | c | d | e | f | g | h | j |
|---|---|---|---|---|---|---|---|---|---|
| a | 1.00 | 0.13 | 0.14 | 0.13 | 0.11 | 0.15 | 0.03 | 0.10 | 0.08 |
| b | 0.13 | 1.00 | 0.42 | 0.25 | 0.07 | 0.24 | 0.13 | 0.04 | 0.10 |
| c | 0.14 | 0.42 | 1.00 | 0.30 | 0.08 | 0.23 | 0.16 | 0.05 | 0.04 |
| d | 0.13 | 0.25 | 0.30 | 1.00 | 0.06 | 0.36 | 0.20 | 0.30 | 0.02 |
| e | 0.11 | 0.07 | 0.08 | 0.58 | 1.00 | 0.06 | 0.07 | 0.08 | 0.01 |
| f | 0.15 | 0.24 | 0.23 | 0.36 | 0.06 | 1.00 | 0.69 | 0.78 | 0.02 |
| g | 0.03 | 0.13 | 0.16 | 0.20 | 0.07 | 0.69 | 1.00 | 0.56 | 0.04 |
| h | 0.10 | 0.04 | 0.05 | 0.30 | 0.08 | 0.78 | 0.56 | 1.00 | 0.03 |
| j | 0.08 | 0.10 | 0.04 | 0.02 | 0.01 | 0.02 | 0.04 | 0.03 | 1.00 |

Table 4.2: Correlation between discriminating variables for photons. a-j correspond to $E_T(had1)/E_T(em)$,$E_{237}/E_{277}$,$W_{\eta 2}$,$E_{max2}/fr\_Et$, $E_{max2} - E_{min1}$,$(E_{7strips} - E_{3strips})/E_{7strips}$,$W_{\eta 1}$,$W_{tot1}$ and $sum(P_{Track})$ respectively.

object. Hence, the Log-likelihood ratio (LLR) is defined as:

$$LLR = \sum_{i=1}^{n} \ln\left(Ls_i/Lb_i\right), \tag{4.3}$$

where $Ls_i$ and $Lb_i$ are density functions of the shower shape variable $i$ for the photon and jet respectively. Track isolation was included as a discriminating variable in equation 4.3.

Figure 4.10 shows the LLR distribution for photons and jets. In practice, one can choose a LLR cut on photon/jet candidates to separate photons and jets. Furthermore, the LLR cut can be tuned w.r.t. $\eta$ and $P_T$ to obtain an optimized separation between photons and jets. For example, a tight LLR cut can be applied on a low $P_T$ jet, while a loosen cut can be applied to a high $P_T$ jet to improve photon efficiency considering the fact that the cross-section of the former is much larger than the latter.

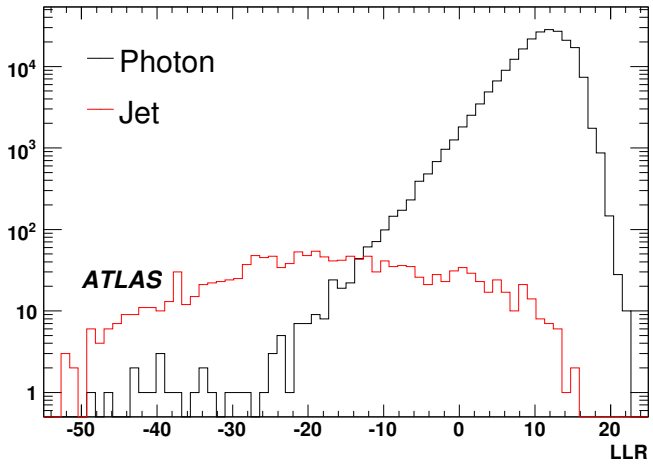


Figure 4.10: LLR distribution for photon and jet. The black solid curve is for photons, the red dashed line is for jets. The $\gamma$-jet sample with $17 < P_T < 35$ GeV is used. The photon is selected with $\Delta R < 0.2$ w.r.t the generated photon. $P_{T\gamma} > 20$ GeV and $P_{Tjet} > 20$ GeV are applied. The jet is selected recoiling to the photon. Here the track isolation is implemented and the bremsstrahlung contribution is removed.

### 4.2.3 Performance of the Log-Likelihood Ratio Method

The photon efficiency is computed with photons from Higgs decay with the nominal geometry. The efficiency is normalized to total number of truth photons, as defined in Section 4.2.1. Figure 4.11 shows photon efficiency vs $\eta$ (left) and $P_T$ (right) with LLR cut values set at 8,9 and 10. The overall efficiencies are 87.6%, 84.3% and 80.0% for the LLR cuts at 8, 9 and 10 shown in Table 4.3 and Table 4.4. Photon efficiency and jet rejection vs different LLR cuts for different $P_T$ ranges are shown in Figure 4.12

The photon efficiency is $P_T$ dependent, as illustrated in Fig. 4.11. A looser cut on low $P_T$ photons is recommended in order to retain flat photon efficiency as a function of $P_T$. Furthermore, it might also be useful to employ a parametrized cut value on LLR as a function of $P_T$ of the photon. The jet rejection is also $P_T$ dependent, as

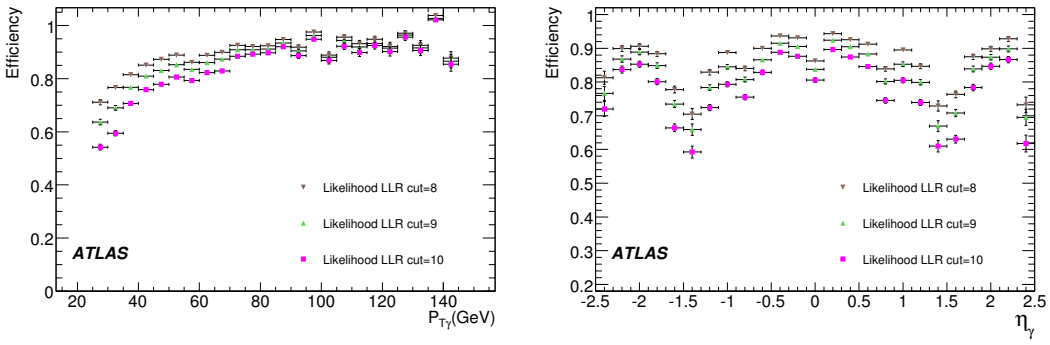


Figure 4.11: Photon efficiency vs $P_T$ and efficiency vs $\eta$ with different LLR cuts. The photon sample is from the $H \rightarrow \gamma\gamma$ sample with nominal geometry.

shown in the plot on the left in Fig. 4.12. A harder cut on LLR for variety of jet $P_T$ can help maintain the rejection vs $P_T$ curve flat, if necessary. The rejection against jets from $\gamma + jet$ and di-jet samples are shown in the fourth and fifth rows. The cuts on photon and jet $P_T$ are 25 GeV and 40 GeV respectively. The rejection for jet from di-jet samples is significantly higher than that on $\gamma + jet$ samples. This is largely due to the fact that the jets in $\gamma + jet$ events are dominated by quark initiated jets while those in di-jet events are enriched with gluon initiated jets.

| | $E_T > 25\ GeV$ | | |
|---|---|---|---|
| LLR cut | $LLR > 8$ | $LLR > 9$ | $LLR > 10$ |
| Eff.(%) | $87.6 \pm 0.3$ | $84.3 \pm 0.2$ | $80.0 \pm 0.2$ |
| Rej.($\gamma$j) | $1660 \pm 170$ | $2190 \pm 260$ | $2930 \pm 390$ |
| Rej. (jj) | $6820 \pm 440$ | $8930 \pm 650$ | $12430 \pm 1070$ |

Table 4.3: Overall photon efficiencies and jet rejections with different LLR cuts. The $E_T$ cut on photons and jets are 25 GeV. The efficiencies on third row are from $H \rightarrow \gamma\gamma$ with nominal geometry. The rejections of $\gamma$-jet in the fourth row are from binned $\gamma$-jet sample. The rejections of di-jet sample in the last row is from the filtered di-jet sample.

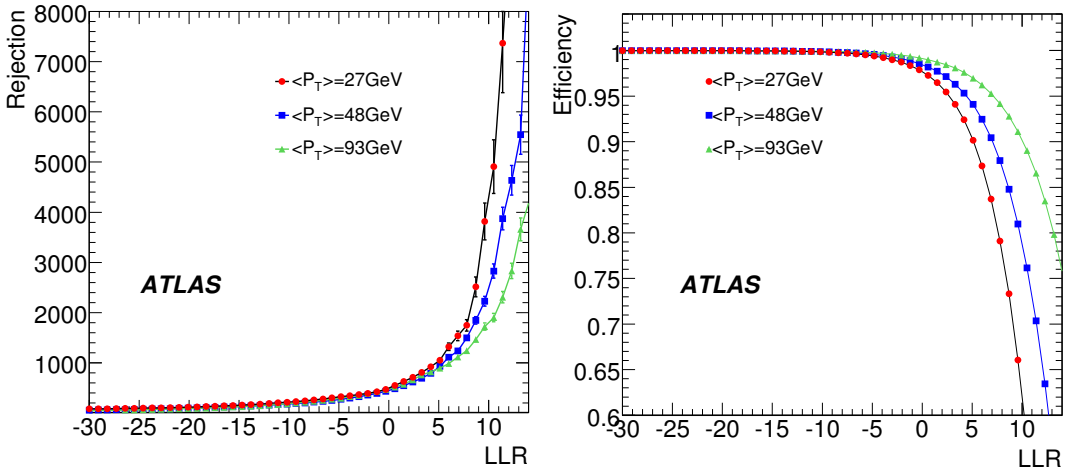


Figure 4.12: Jet rejection and photon efficiency w.r.t LLR cut. The red dotted line is for $\gamma$-jet $20 < P_T < 35$ GeV with $P_{T\gamma,jet} > 20$ GeV, the curve with blue squares is for $\gamma$-jet $35 < P_T < 70$ GeV with $P_{T\gamma,jet} > 35$ GeV, and the curve with green triangles is for $\gamma$-jet $70 < P_T < 140$ GeV with $P_{T\gamma,jet} > 70$ GeV. The track isolation is implemented, and bremsstrahlung contribution is removed.

## 4.3 Comparison of Photon Identification Algorithms

Figure 4.13 shows the rejection and efficiency curve with cut-based and likelihood ratio method for binned $\gamma + jet$ sample. Similarly Fig. 4.14 shows the rejection and efficiency curve with cut-based and likelihood ratio method for di-jet sample. Further, Tables 4.5 and 4.6 provide numerical comparisons of fake rejections for the three methods with similar photon efficiencies. The $\gamma + jet$ events whose jets are dominated by quark initiated jets are the largest reducible background for $H \rightarrow \gamma\gamma$. It is apparent from Figure 4.13 and Figure 4.14 that both of these two methods demonstrate significantly reduced rejections for jets from the $\gamma + jet$ samples than those from di-jet samples. As discussed in Section 4.2.3, this effect is attributed to the fragmentation differences of the quark vs gluon initiated jets. Further studies would be required to

| | $E_T > 40\ GeV$ | | |
|---|---|---|---|
| LLR cut | $LLR > 8$ | $LLR > 9$ | $LLR > 10$ |
| Eff.(%) | $86.4 \pm 0.3$ | $83.2 \pm 0.2$ | $79.0 \pm 0.2$ |
| Rej.($\gamma$j) | $1690 \pm 140$ | $2170 \pm 210$ | $2650 \pm 280$ |
| Rej. (jj) | $6780 \pm 1000$ | $7800 \pm 1230$ | $11550 \pm 2220$ |

Table 4.4: Overall photon efficiencies and jet rejections with different LLR cuts. The $E_T$ cut on photons and jets are 40 GeV. The efficiencies on third row are from $H \rightarrow \gamma\gamma$ with nominal geometry. The rejections of $\gamma$-jet in the fourth row are from binned $\gamma$-jet sample. The rejections of di-jet sample in the last row is from the filtered di-jet sample.

improve the algorithm performances.

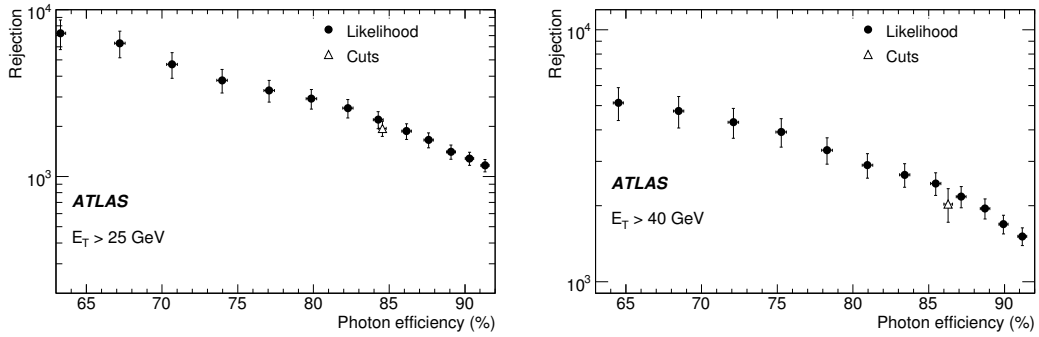


Figure 4.13: Jet rejection vs photon efficiency for binned $\gamma + jet$ samples with cut $P_{T\gamma}, P_{Tjet} > 25$ GeV (left) and cut $P_{T\gamma}, P_{Tjet} > 40$ GeV (right). The initial jet is normalized to full simulated truth jet with cone size 0.4. The track isolation is implemented and the bremsstrahlung contribution is removed. Photon efficiency is from $H \rightarrow \gamma\gamma$ sample with nominal geometry.

In addition, as can be seen from Figs. 4.13 and 4.14, for equal efficiencies, the log-likelihood based algorithm and the cut based algorithm perform similarly in rejecting highly electromagnetic jets.

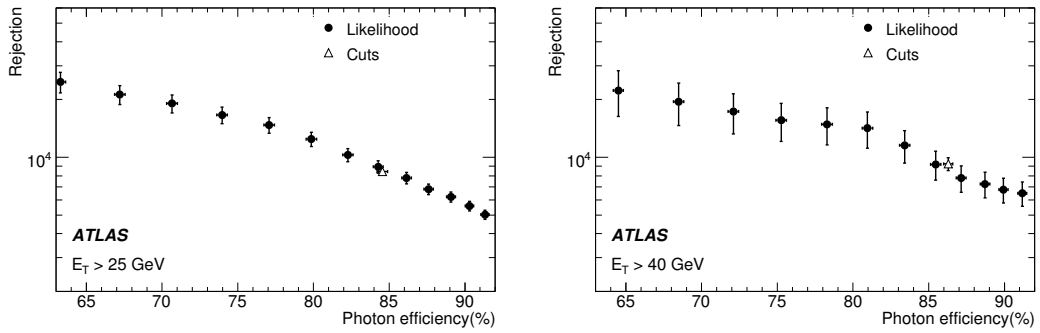


Figure 4.14: Jet rejection vs photon efficiency for filtered di-jet samples with cut $P_{T\gamma}, P_{Tjet} > 25$ GeV(left) and cuts $P_{T\gamma}, P_{Tjet} > 40$ GeV (right). The initial jet is normalized to full simulated truth jet with cone size 0.4.The track isolation is implemented and the bremsstrahlung contribution is removed. The photon efficiency is taken from a $H \rightarrow \gamma\gamma$ sample with nominal geometry.

| | $E_T > 25\ GeV$ | | $E_T > 40\ GeV$ | |
|---|---|---|---|---|
| | LLR | Cut based | LLR | Cut based |
| Efficiency(%) | $84.3 \pm 0.2$ | $84.5 \pm 0.2$ | $87.1 \pm 0.2$ | $86.3 \pm 0.2$ |
| Rejection | $2190 \pm 250$ | $1940 \pm 230$ | $2170 \pm 210$ | $2030 \pm 190$ |

Table 4.5: Comparison of jet rejection vs photon efficiency with three methods for $\gamma + jet$ sample.

| | $E_T > 25\ GeV$ | | $E_T > 40\ GeV$ | |
|---|---|---|---|---|
| | LLR | Cut based | LLR | Cut based |
| Efficiency(%) | $84.3 \pm 0.2$ | $84.6 \pm 0.2$ | $85.5 \pm 0.2$ | $86.3 \pm 0.2$ |
| Rejection | $8930 \pm 650$ | $8240 \pm 270$ | $9170 \pm 1570$ | $9240 \pm 710$ |

Table 4.6: Comparison of jet rejection vs photon efficiency with three methods for di-jet samples

## 4.4 Photon identification and background estimation with Data

The photon identification studies shown in this chapter are based on a combination of MC and test beam studies. In this section, we give a qualitative discussion on the prospects for the optimization of the photon identification selection criteria using data. The study in this section is based on the likelihood photon ID method.

The understanding of how the di-photon spectrum breaks up in terms of various contributions is a cumbersome exercise and it requires a very good understanding of the quark and gluon fragmentation as well as the identification efficiency of $\pi^0$s. Nevertheless, in the regime of very tight ID and isolation criteria it is expected that the observed spectrum of photon candidates will be dominated by prompt photons. As the ID and isolation criteria tighten, the contribution from reducible backgrounds should drop quickly. If one defines the rate of photon candidates divided by the efficiency of real photons, one would expect that such a ratio would asymptotically approach a constant value as the ID and isolation criteria are tightened.

Two possibilities could be envisioned in order to avoid potential biases affecting the analysis. The first one is to study di-photon events with an invariant mass outside the range of the SM Higgs search, i.e. $110 < M_{\gamma\gamma} < 150$ GeV. This approach has the advantage of strongly suppressing potential biases but it jeopardizes a general search for di-photon resonances. Here, we discuss the possibility of studying photon ID and isolation in events with one photon candidate and we evaluate the bias introduced by

| $P_T$ Range | $\sigma\,(pb)$ | $\nu$ (Hz) | Lumi $(pb^{-1})$ |
|---|---|---|---|
| $25-40$ GeV/$c$ | $1.43\times10^{8}$ | $1.43\times10^{5}$ | $1.40\times10^{-2}$ |
| $40-70$ GeV/$c$ | $3.47\times10^{7}$ | $3.47\times10^{4}$ | $5.8\times10^{-2}$ |
| $70-100$ GeV/$c$ | $4.70\times10^{6}$ | $4.70\times10^{3}$ | 0.43 |
| $100-140$ GeV/$c$ | $1.53\times10^{6}$ | $1.53\times10^{3}$ | 1.31 |

Table 4.7: Relevant quantities for the photon identification studies with data as a function of the probing jet $P_T$ (see text). The second and third columns show the effective cross-sections and the corresponding input trigger rate assuming an instantaneous luminosity of $10^{32}cm^{-2}s^{-1}$ for di-jet events. The last column displays the equivalent integrated luminosity needed to collect two million events for each $P_T$ bin.

such a procedure.

The data samples necessary for the study could be collected with pre-scaled single jet triggers of different thresholds. In order to avoid trigger biases, the leading calorimeter deposition that was not used for triggering the event would be treated as a probing jet, or photon candidate. Table 4.7 displays the cross-sections and the corresponding input trigger rate assuming an instantaneous luminosity of $10^{32}cm^{-2}s^{-1}$ for di-jet events. These results were obtained with a fast detector simulation and the probing jet was required to lie in the central detector region, $|\eta| < 2.5$. The last column in Table 4.7 displays the effective integrated luminosity [1] needed to collect two million events for each $P_T$ bin.

Figure 4.15 shows the expected efficient cross-sections for events with one photon candidate over the photon efficiency and events with two photon candidates over the product of the photon efficiencies as a function of the efficiency of the probing photon candidate. In the case of events with two photon candidates, the sub-leading photon is treated as the probing photon candidate. The plot on the left in Figure 4.15 shows the

[1]The corresponding integrated luminosity required would be equal to the ratio of the effective luminosity reported in Table 4.7 divided by the trigger pre-scale.

expected cross-section over the photon efficiency for the di-jet and $\gamma$-jet processes in events with one photon candidate. The blue and black histograms correspond to the contribution from $\gamma$-jet and di-jet, respectively. The plot on the right in Figure 4.15 shows the expected cross-sections from the $\gamma$-jet and $\gamma\gamma$ processes over the product of the photon efficiencies. The blue and black distributions correspond to the $\gamma$-jet and $\gamma\gamma$ processes, respectively. As discussed above the ratios defined in Figure 4.15 approach a constant values for values of the photon efficiency at which the contribution from events with fake photons is suppressed.[2]

A tune of the photon ID and isolation using the curve on the left plot of Figure 4.15 may introduce a bias which can cause the difficulty of estimating contribution from different backgrounds. The diagrams contributing to the samples of one and two photon candidates, and, therefore the QCD color flow, are different. In addition, the relative contribution from quark and gluon initiated jets in events with a a fake photon is also different.

Figure 4.16 elucidates the bias introduced by photon ID optimization using single photon candidate events. The plot compares the shapes of the distributions shown in Figure 4.15. The plot on the right in Figure 4.16 shows the transverse momentum spectra of the probing photon candidate in events with one (blue histogram) and two photon candidates (red histogram). Both distributions in Figure 4.15 seem to indicate that the bias introduced is not a large one.

Finally, it is important to note that we rely on the on a MC prediction of the photon efficiency against ID and isolation requirements. This assumption can be

[2]It is relevant to note that in the study presented in this Section the contribution from fragmentation photons was not considered. This shortcoming does not alter the qualitative discussion presented here.

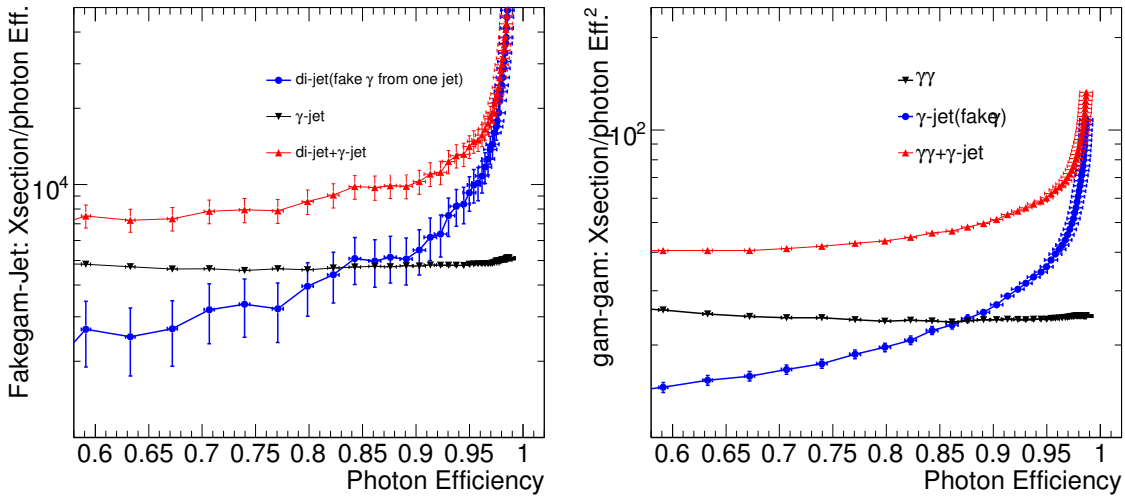


Figure 4.15: Expected efficient cross-sections for events with one photon candidate over the photon efficiency and events with two photon candidates over the product of the photon efficiencies as a function of the efficiency of the probing photon candidate. The plot on the left shows the expected cross-section over the photon efficiency for the di-jet and $\gamma$-jet processes in events with one photon candidate. The blue and black histograms correspond to the contribution from $\gamma$-jet and di-jet, respectively. The plot on the right shows the expected cross-sections from the $\gamma$-jet and $\gamma\gamma$ processes over the product of the photon efficiencies. The blue and black distributions correspond to the $\gamma$-jet and $\gamma\gamma$ processes, respectively. A $P_T$ cut of 35 GeV is applied on the photon.

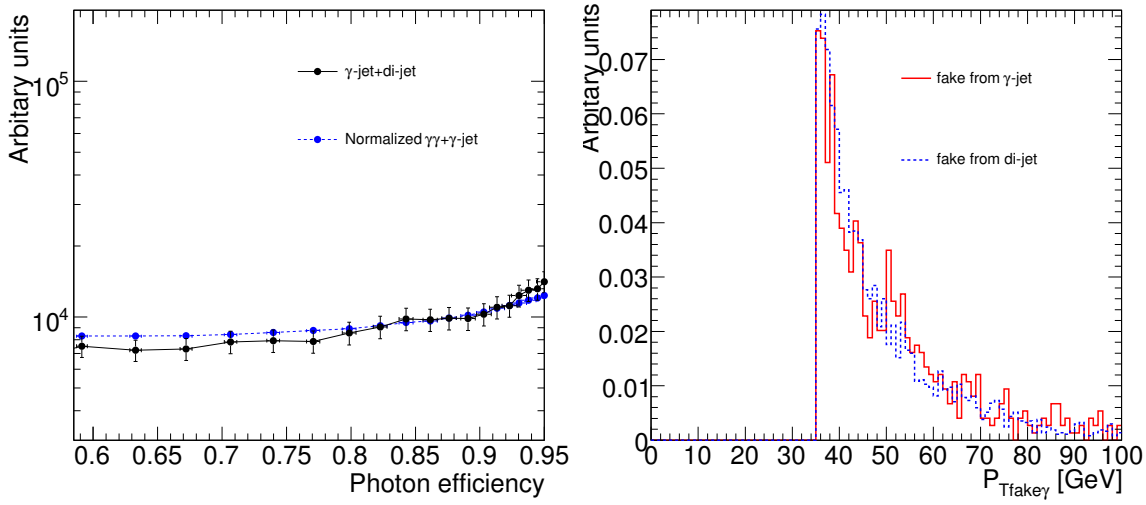


Figure 4.16: Evaluation of bias introduced by photon ID optimization using single photon candidate events. The plot compares the shapes of the distributions shown in Figure 4.15. The plot on the right shows the transverse momentum spectra of the probing photon candidate in events with one (blue histogram) and two photon candidates (red histogram).

partially checked with data using $Z \rightarrow e^+e^-$ and $Z \rightarrow e^+e^-\gamma$ events.

In order to estimate the background of $\gamma$-jet from a mixed $\gamma j$ and di-jet sample with one tagging photon [3], a low photon efficiency region is defined as control sample region. It is natural that the signal-like region is defined as the region having a photon efficiency between 80% and 90%. Thanks to the asymptotic shape of the di-jet+$\gamma$-jet (the red triangle curve on Figure 4.17), one can evaluate the overall cross-section of di-jet+$\gamma$-jet at very low photon efficiency region. Since the contribution from di-jet in this region is very small w.r.t that of $\gamma$-jet, this asymptotic value of the cross-section can be roughly regarded as the contribution from $\gamma$-jet although contamination from DUI-jet still introduces some bias to this method. Considering the flatness of the $\gamma$-jet shape

[3]Similarly, one can implement this method estimating $\gamma$-jet from a mixed $\gamma\gamma$ and $\gamma$-jet sample with two tagging photons.

as the black downward triangle in Figure 4.17 shows, a subtraction of the asymptotic value from the di-jet+$\gamma$-jet curve can be used as an estimation of di-jet background. The curves of expected di-jet and estimated di-jet (dotted green curve with square markers) are compared in Figure 4.17. As expected, with the enhancement of the photon efficiency, the bias goes down. In signal-like region, a very good agreement between expected and estimated di-jet can be achieved.

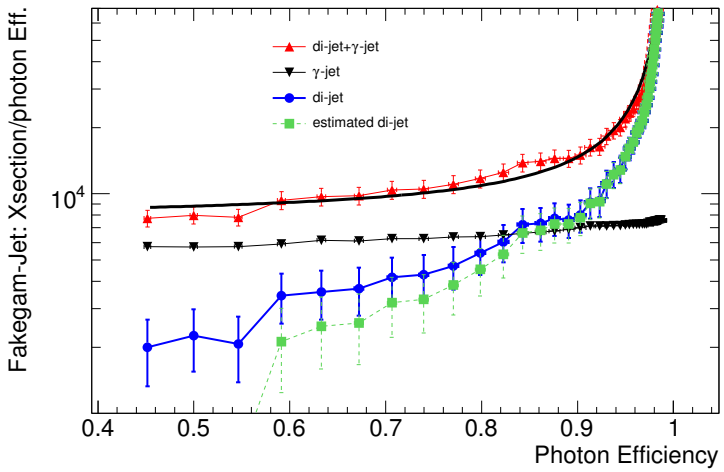


Figure 4.17: The expected cross-section over the photon efficiency for the di-jet and $\gamma$-jet processes in events with one photon candidate. The red curve is the contribution from $jj+\gamma j$. The blue and black curves correspond to the contribution from $\gamma$-jet and di-jet, respectively. The green dashed line is the estimated contribution from di-jet. $P_T$ cut applied on photon is 30 GeV.

# Chapter 5

# Analysis of the search for Standard Model $H \rightarrow \gamma\gamma$

The inclusive $H \rightarrow \gamma\gamma$ analysis has been studied in ATLAS for many years [22, 55, 69]. As Figure 1.4 shows, in the mass range $110 < m_H \leq 140$ GeV the Higgs boson is expected to decay into two photons with a reasonably large branching fraction; this makes the $H \rightarrow \gamma\gamma$ channel feasible at the LHC. In this chapter, the sensitivity of ATLAS via this channel considering the impact of higher order QCD corrections on the discovery potential is re-evluated.

The Higgs boson can be produced in association with one or two hadronic jets of high transverse momentum, $P_T$. The search for a Higgs boson using the diphoton decay in association with high $P_T$ hadronic jets at the LHC has been suggested in ref [43, 44]. In this chapter, an update of these studies based on a more complete description of the detector simulation is presented.

The Higgs boson production without a hard hadronic jet, with one hadronic jet and with two hadronic jets provides different S/B ratios. A combined analysis of these three sub-channels can improve the overall sensitivity. Furthermore, classifying the

photons according to $\eta$ [45, 46] can also help improve sensitivity because the Higgs mass resolution depends on the $\eta$ of photons. In addition to the diphoton invariant mass, other discriminating variables such as $P_{T\gamma\gamma}$ and $\cos(\theta^*)$ are incorporated into the analysis and a combination of them altogether with the $\eta$ and jets classification are processed by means of an unbinned maximum-likelihood fit (see also Chapter 6). The beautiful feature of the likelihood fit is that it uses reconstruction properties and event classification to separate the data sample into different subsamples and fit simultaneously. The systematics due to statistics of the side bands are taken into account automatically too.

## 5.1 Monte Carlo event generation

The MC event generation of the signal process in this study uses a full detector simulation based on GEANT4 [24]. The background MC samples are processed with a fast detector simulation [31] and are used primarily for the evaluation of the analysis sensitivity. The photon efficiency and photon-jet separation are parameterized as a function of the photon $P_T$ with a full detector simulation and applied to the fast detector simulation.

### 5.1.1 Signal processes

As Figure 1.2 shows, there are four Higgs production processes: gg Fusion, Vector Boson Fusion (VBF), W/Z associated with Higgs-strahlung and $t\bar{t}(b\bar{b})H$ associated production (ttH). The Leading Order (LO)/Next Leading Order (NLO) cross-section and branching ratios (Br.) for several masses are listed in Table 5.1 and Table 5.2. All signal cross sections in this chapter are normalized to QCD NLO. The gluon

fusion process simulated with MC@NLO is used here [28, 29]. It gives a QCD NLO matrix element in addition to a good description of multiple soft gluon emission at the next-to-next-to-leading logarithmic level (NNLL). This higher order consideration is relevant to the evaluation of the discriminating power of the $P_T$ of diphoton and jets distribution. Other signal events are generated by using PYTHIA which implements LO ME calculations for all signal processes considered here. All signal process used here are from full simulated samples. A photon filter with $P_T > 10$ GeV and $|\eta| < 2.7$ is implemented on all samples except for gluon fusion.

| $m_H$ | *gg Fusion* | | *VBF* | | *WH* | | *ZH* | | *ttH* | |
|---|---|---|---|---|---|---|---|---|---|---|
| | LO | NLO | LO | NLO | LO | NLO | LO | NLO | LO | NLO |
| 120 | 20.170 | 36.506 | 4.25 | 4.47 | 1.414 | 1.735 | 0.7517 | 0.9210 | 0.537 | 0.669 |
| 130 | 17.491 | 31.763 | 3.93 | 4.13 | 1.095 | 1.346 | 0.5852 | 0.7185 | 0.428 | 0.534 |
| 140 | 15.314 | 27.858 | 3.63 | 3.81 | 0.860 | 1.061 | 0.4617 | 0.5688 | 0.345 | 0.431 |

Table 5.1: Initial leading order (LO) and next leading order (NLO) cross-section (unit pb) for different signal process with mass (unit GeV) scan. The NLO cross-sections are used in this chapter.

| $m_H$ (GeV) | 120 | 130 | 140 |
|---|---|---|---|
| Br. | $2.23 \cdot 10^{-3}$ | $2.27 \cdot 10^{-3}$ | $1.97 \cdot 10^{-3}$ |

Table 5.2: The branching ratios for Higgs decay into two photons as a function of the mass.

### 5.1.2 Background processes

There are two groups of backgrounds. The first group is backgrounds coming directly from two isolated photons, namely irreducible background (see Figure 5.1. The second group consists of reducible backgrounds coming from events with at least one fake photon. These fake photons are mostly due to the misidentification of a leading

$\pi_0$ resulting from the fragmentation of a quark or a gluon as Figure 5.2 and Figure 5.3 shows. Same as signal, we consider QCD NLO corrections to backgrounds in the analysis. As Figure 5.1 shows, the irreducible background is mainly due to $q\bar{q} \rightarrow \gamma\gamma$ (diagrams a-c) and $qg \rightarrow \gamma\gamma$(diagram d), so called Born and Bremsstrahlung contributions and $gg \rightarrow \gamma\gamma$ (diagrams e-i) also refered to as the box contributions. Both the DIPHOX [47] and RESBOS [48, 49] programs can evaluate the irreducible background. DIPHOX includes diagrams a-e of Figure 5.1 and computes the cross-section at NLO but without the resummation effects. Moreover, it includes the fragmentation from quark and gluon to photons at NLO as diagrams j-m of Figure 5.1 shows. RESBOS covers the Born and box contributions at NLO except that fragmentation from quarks or gluons is only at LO as well as resummation effects to NNLL. The prediction of DIPHOX and RESBOS for the total irreducible background agree to better than 10% [50].

RESBOS and DIPHOX are parton-level generators. In order to evaluate the irreducible backgrounds for signal significance computations and to include the effect of high $P_T$ multi-jets, the ALPGEN MC generator is used. This includes $2 \rightarrow N$ tree-level matrix elements where N=2-5. The minimum parton and photon $P_T$ and maximum pseduorapidity are set to 20 GeV, $|\eta| < 5$ for jets and $|\eta| < 2.7$ for photons. The MLM matching between parton shower and matrix elements is used. The $P_T$ threshold for the merging of the parton shower and MC is 20 GeV.

The cross-section contributions from different components w.r.t the diphoton system $P_T$ are shown in the left plot of Figure 5.4. In comparison with the RESBOS Born contribution, one can see that RESBOS is NNLL description of resummation

significantly affecting the $P_T$ spectrum of the diphoton system at the soft $P_T$ region. The transverse momentum spectra ALPGEN is re-weighted to the RESBOS and the weighted invariant mass distribution agrees very well with RESBOS as the left plot of Figure 5.5 shows.

The Box contribution is simulated with the PYTHIA package with a LO matrix elements. The shapes of distributions predicted by PYTHIA and RESBOS are shown in the right plot of Figure 5.4. As was done for the Born process, PYTHIA's cross-section and the shape of the $P_{T\gamma\gamma}$ spectrum is reweighted to RESBOS. The weighted invariant mass distribution is also fairly consistent with RESBOS, as the right plot of Figure 5.5 demonstrates.

The inclusive cross-section for the $\gamma$-jet process is obtained using the package JETPHOX [51]. This package computes single photon production from the direct production and fragmentation . The distribution of the photon $P_T$ obtained with this package is compared with that obtained for the direct production using the PYTHIA package. The differential cross section obtained with JETPHOX is found to be a factor of 2.1 larger than that obtained with PYTHIA with weak $P_T$ dependence for $P_{T\gamma}$ larger than 25 GeV.

The inclusive cross-section for di-jet production is computed with the NLO-JET++ package [52, 53] which considers QCD NLO corrections. It is observed that the cross-section obtained is a factor of 1.3 larger than that obtained with PYTHIA with $P_{T\text{jet}} > 25$ GeV.

ALPGEN MC, simulated with Atlfast is used to generate samples of $\gamma$-jets and multi-jet in order to feasibly compute the signal significance. This generator produces

$2 \rightarrow N$ tree level matrix elements, where N = 2-5. Similar to $\gamma\gamma - jets$, the MLM prescription for the merging of the parton shower and the matrix elements is also implemented.

In summary, the MC packages and the cross-sections (unit pb) for irreducible and reducible backgrounds are described in Table 5.3.

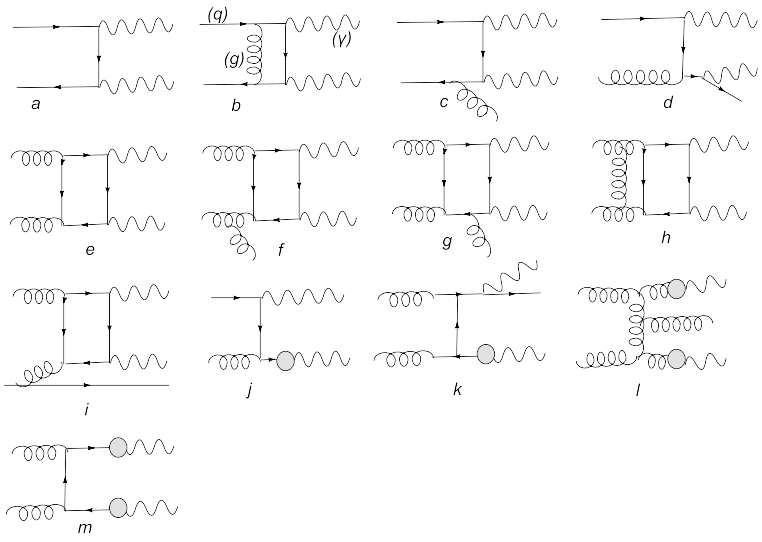


Figure 5.1: Some diagrams of NLO irreducible backgrounds. Among them, diagrams a-c are from $q\bar{q} \rightarrow \gamma\gamma$. Diagram d is the contributions from $qg \rightarrow \gamma\gamma$. Diagrams e-i are essentially box contributions. Diagrams k-m correspond to contributions from the fragmentation of one or two quarks and gluons.

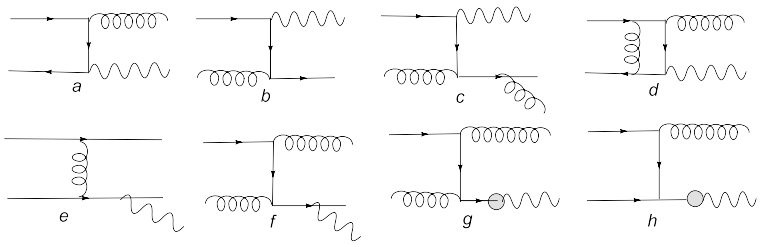


Figure 5.2: Some diagrams of NLO reducible backgrounds with one fake photon. Diagrams a-e are from the contribution with one photon from direct production and the other one from fake photon. Diagrams g-h correspond to one photon from fragmentation from a quark and the other one from fake photon.

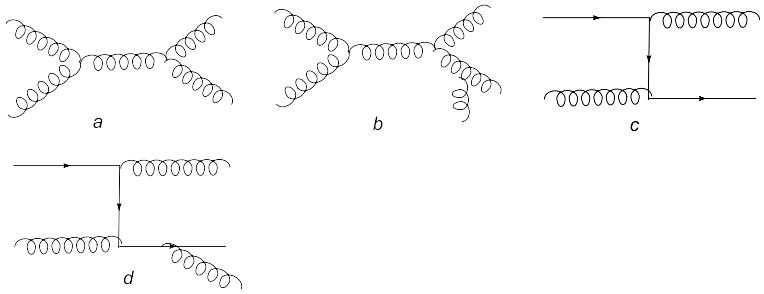


Figure 5.3: Some diagrams of reducible backgrounds with two fake photons.

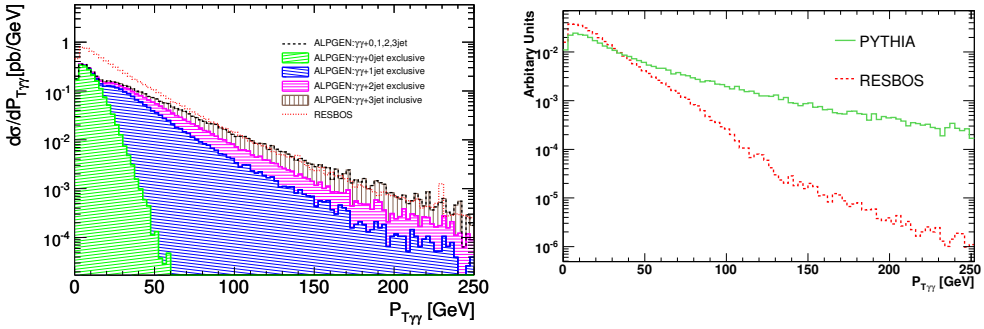


Figure 5.4: The $P_{T\gamma\gamma}$ distribution of the irreducible background of Born (left) and box (right). The generators used for left plot are ALPGEN 2.6 with contribution from different jet multiplicities and RESBOS. The generators for right plot are PYTHIA 6.4 and RESBOS. The cuts applied on leading and subleading photons are $P_{T\gamma 1} > 25$ GeV,$P_{T\gamma 2} > 25$ GeV and 80 GeV$< m_{\gamma\gamma} <$ 150 GeV.

| | Irreducible Backgrounds | | Reducible Backgrounds | |
|---|---|---|---|---|
| Process | $q\overline{q}, qg \rightarrow \gamma\gamma x$ | $gg \rightarrow \gamma\gamma$ | $\gamma$-jets | $jj$ |
| Cross-section calculator | RESBOS DIPHOX | RESBOS | JETPHOX | NLOJET++ |
| Cross-section (pb) | 20.9 | 8.0 | $180{\cdot}10^3$ | $477{\cdot}10^6$ |
| Event generator (fullsim) | PYTHIA | PYTHIA | PYTHIA | PYTHIA |
| Event generator (fastsim) | ALPGEN | PYTHIA | ALPGEN | ALPGEN |

Table 5.3: Summary of the cross-sections of the irreducible and reducible backgrounds used for the $H \rightarrow \gamma\gamma$ inclusive analysis. The last two rows indicate the MC packages used for event generation with a full and fast detector simulation, respectively.

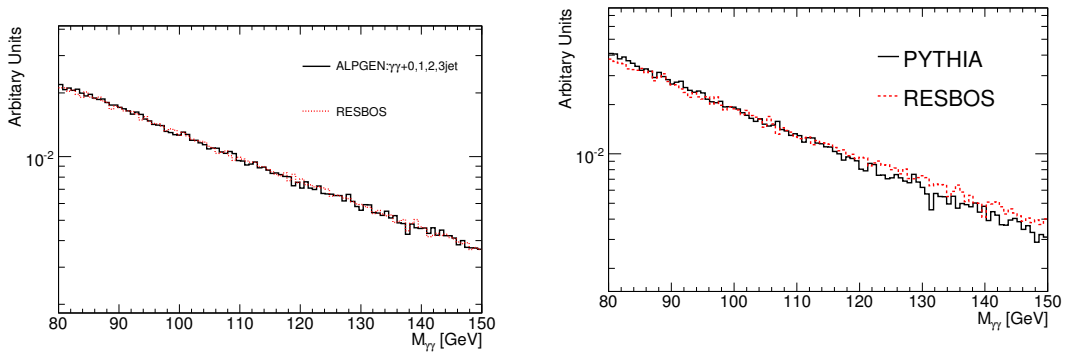


Figure 5.5: The $m_{\gamma\gamma}$ distribution of the irreducible background of Born (left) and Box (right) after reweighing $P_{T\gamma\gamma}$ from ALPGEN w.r.t that from RESBOS. The cuts applied on leading and subleading photons are $P_{T\gamma 1} > 25$ GeV,$P_{T\gamma 2} > 25$ GeV and 80 $GeV < m_{\gamma\gamma} < 150$ GeV.

## 5.2 Photon ID and Trigger effects

Powerful photon identification and jet rejection for $P_T > 25$ GeV is critically important for the $H \rightarrow \gamma\gamma$ channel. We use the cut based photon ID method in this chapter. The cross-sections of $\gamma$-jets and di-jet are at the level of 100 nb and 1 mb, respectively. This requires the rejection of quark initiated jets of about 1000 and gluon initiated jets of about 10000 to achieve a sensitive signal and background ratio.

In this study, detector effects for signal are estimated using full detector simulation. For backgrounds, photon efficiency and jet rejection are parameterized based on fully simulated samples, as shown in Figure 5.4, and the parametrizations are applied on a fast simulated samples. During the parameterization of photon fake rate, one effect that needs to be taken into account is the migration of high $P_T$ jets to low $P_T$ fake photons. For example, as shown in the upper right plot in Figure 5.6, a significant amount of fake photons have $P_T$ softer than the corresponding hadronic jet $35\,GeV < P_{Thadron} < 70\,GeV$. The migrations degrade the rejections for $\gamma$-jet1, $\gamma$-jet2 and $\gamma$-jet3, which are defined in Table 4.1, by 27%, 9% and 2%, respectively. The $\gamma$-jets is dominated by quark initiated jets. The rejections against gluon initiated jets and quark initiated jets are shown in Table 5.4 (see [34]). It can be concluded from this table that the rejection of gluon initiated jets is roughly a factor of 10 larger than that of quark initiated ones. This effect is also considered in the parametrization process. The reasonable consistency between fully simulated $\gamma$-jet and its parametrized fast simulated partner can be seen in Figure 5.8. The $\gamma$-jet samples employed in comparison and parametrization are totally independent. It is expected that the agreement

in low and high $m_{\gamma\gamma}$ regions could be improved if the statistics in the high and low $P_T$ $\gamma$-jet regions were higher.

There are three sequential triggers: L1, L2 and the Event Filter, as mentioned in Section 2.2.6. Currently, there are two trigger menus for the $H \rightarrow \gamma\gamma$: 2g17i and g55. The 2g17i trigger selects events with at least two isolated photons with $P_T > 20$ GeV. The g55 trigger selects events with at least one photon with $P_T > 60$ GeV without requiring isolation. The cumulative efficiency of 2g17i triggering on $H \rightarrow \gamma\gamma$ is about 94% as Table 5.5 shows [54, 34]. The trigger impact on the $\gamma$-jet sample can be seen in Figure 5.9. It can be found that the trigger is more powerful in reducing the $\gamma$-jet contribution in the regions with larger $m_{\gamma\gamma}$. This is mostly due to the isolation criteria the trigger brings. In this study, the trigger effect for signal is taken directly from full simulation. However, for the background, it is again parametrized according to the fully simulated sample and implemented into the fast simulated sample.

| | quark-jet | gluon-jet |
|---|---|---|
| Rejection before isolation cut | 1770±50 | 15000±700 |
| Rejection after isolation cut | 2760±100 | 27500±2000 |

Table 5.4: Rejection measured in the inclusive jet sample for $E_T > 25$ GeV.

| | 2g20i Trigger menu | |
|---|---|---|
| Trigger Level | Efficiency [%] | Rate [Hz] |
| LVL1 | 96.3±0.3 | 140 ± 10 |
| LVL2 Calo | 95 ±0.4 | 4.7 ± 1.6 |
| EF Calo | 93.6±0.4 | 1.6 ± 1 |

Table 5.5: Efficiency of 2g17i triggering on $H \rightarrow \gamma\gamma$ normalized w.r.t. kinematic cuts and the corresponding rate.

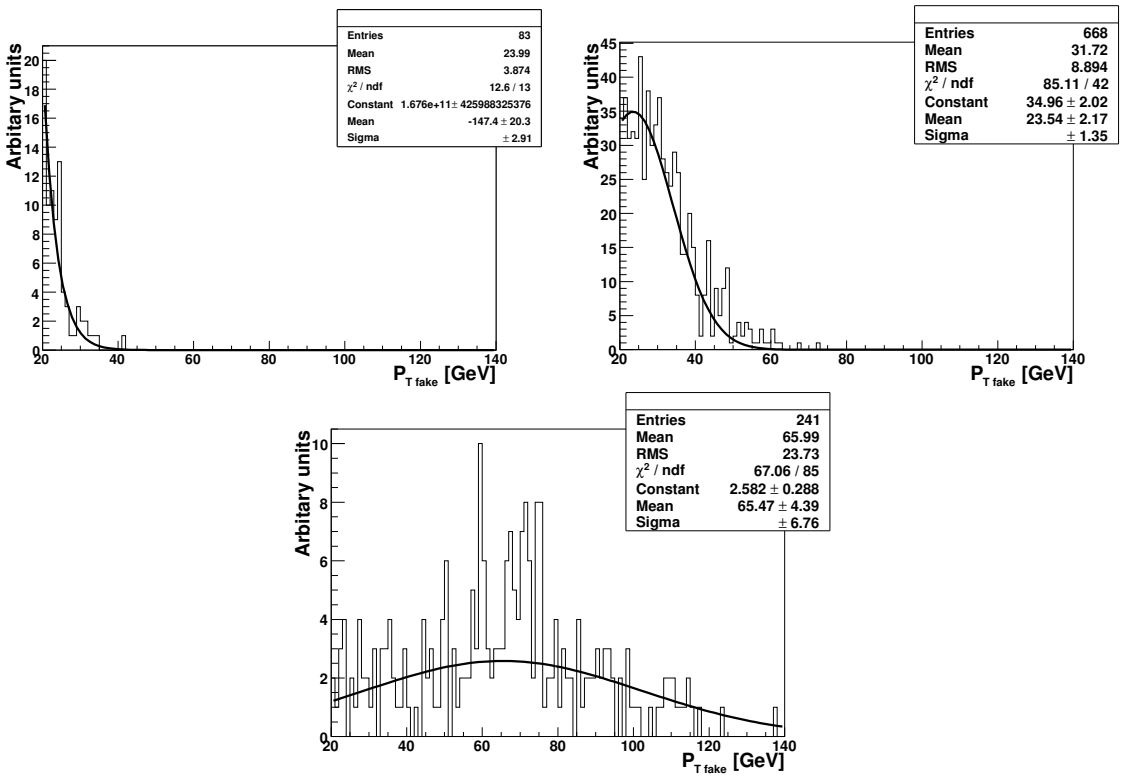


Figure 5.6: The distribution of fake photon for $\gamma Jet1$ (upper left), $\gamma Jet2$ (upper right plot) and $\gamma Jet3$ (bottom). The samples are described in Table 4.1.

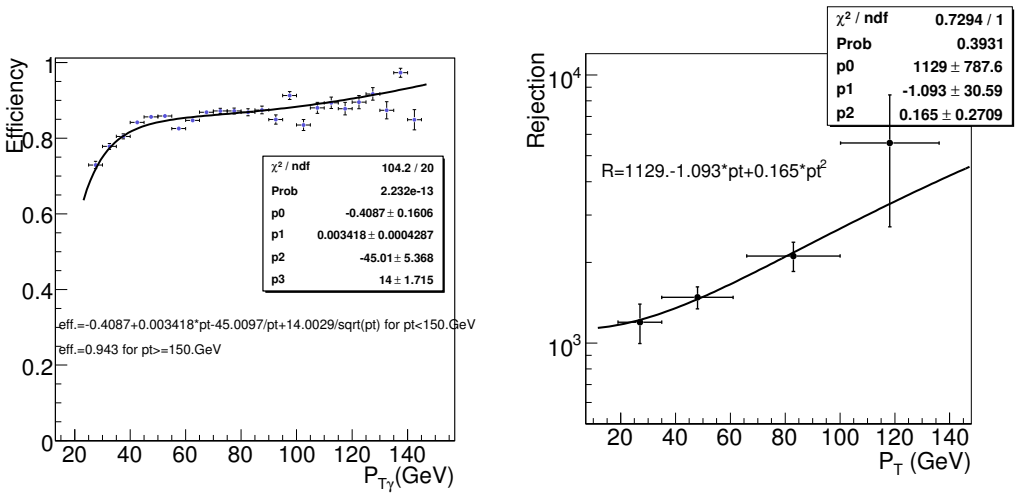


Figure 5.7: The parameterizations of photon efficiency and jet rejection. The photon is from fully simulated $H \to \gamma\gamma$. The jets are from binned full simulated $\gamma$-jet sample.

## 5.3 Event selection

In this Section the details of the various event selections are described. The event selection for the inclusive analysis is given in Section 5.3.1 and for the Higgs boson search in association with jets are given in Sections 5.3.2 and 5.3.3. The various event selections are presented as disjoint analyses. In Section 5.3.4 the combined analysis based on those three channels are described and discussed.

### 5.3.1 Inclusive analysis

The inclusive analysis refers to the search for a resonance in all events with two photons that pass certain quality criteria. The analysis reported here follows closely the event selection of past studies [22, 55].

The following cuts are applied:

**Ia** At least two photon candidates in the central detector region defined as $|\eta| <$ 2.37 excluding the transition region between barrel and endcap calorimeters,

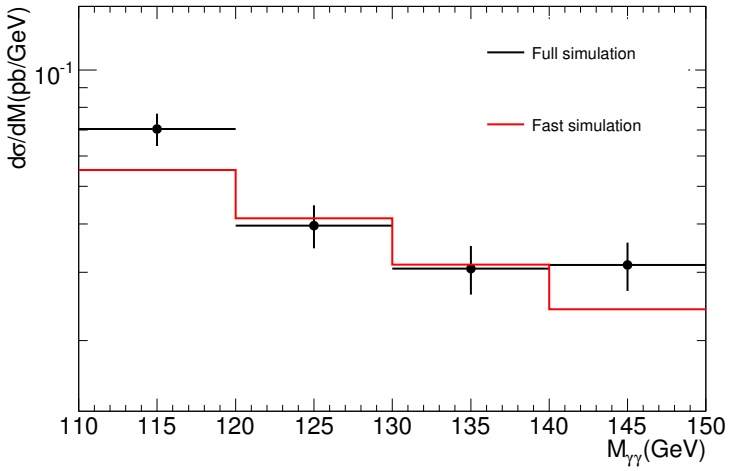


Figure 5.8: The comparison between fully simulated $\gamma jet$ and that of fast simulated with parametrization. The cuts applied on leading and subleading photons are $P_{T\gamma 1} > 40GeV$ and $P_{T\gamma 2} > 25GeV$.

$1.37 < |\eta| < 1.52$ i.e., the crack region. At this level it is required that the event passes the trigger selection.

**Ib** Transverse momentum cuts of 40 and 25 GeV on the leading and sub-leading photon candidates, respectively.

Figure 5.19 displays the transverse momentum spectra of photon candidates after the application of Cuts **Ia-Ib** for both signal ($m_H = 120$ GeV) and background. The plots on the left and right in Figure 5.19 correspond to the leading and sub-leading photons, respectively. Signal and background processes are summed according to cross-section and then normalized to unity.

The fiducial cuts in **Ia** are motivated by the quality of the off-line photon identification and the fake photon rate. The values of the cuts on the transverse momentum of the photon candidates (Cut **Ib**) are not varied and are obtained by previous optimization studies [22].

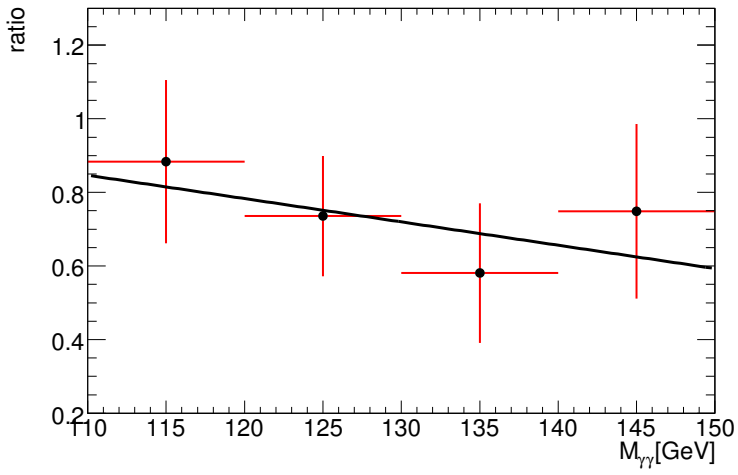


Figure 5.9: The ratio of the cross-section with trigger(2g17i) to that without trigger as a function of $m_{\gamma\gamma}$. The sample used here is $\gamma$-jet with one jet faking a photon.

Figure 5.11 shows the expected di-photon mass spectrum after the application of Cuts **Ia** and **Ib**. The hashed histogram in the bottom corresponds to the contributions from events with one and two fake photons. The second hashed histogram corresponds to the irreducible backgrounds. The background contributions are obtained with MC samples with a fast detector simulation normalized to the cross-sections. The fast detector simulation is corrected in order to reproduce the aspects of the detector performance critical to the analysis, which are obtained with a full detector simulation. The expected contribution from a Higgs boson signal for $m_H = 120$ GeV, obtained with a full detector simulation, is also shown in Figure 5.11. Figure 5.12 shows the signal's di-photon distribution after Cuts **Ia** and **Ib** and a Gaussian fit is applied around the peak of the $m_{\gamma\gamma}$. The resolution is about 1.4 for $m_H = 120$ GeV.

Tables 5.6 and 5.7 show the expected cross-sections (in fb) for background and signal in a mass window of $\pm 1.4\sigma$ around 120 GeV after the application of Cuts **Ia** and **Ib**. Table 5.6 indicates that the relative contribution from events with at least

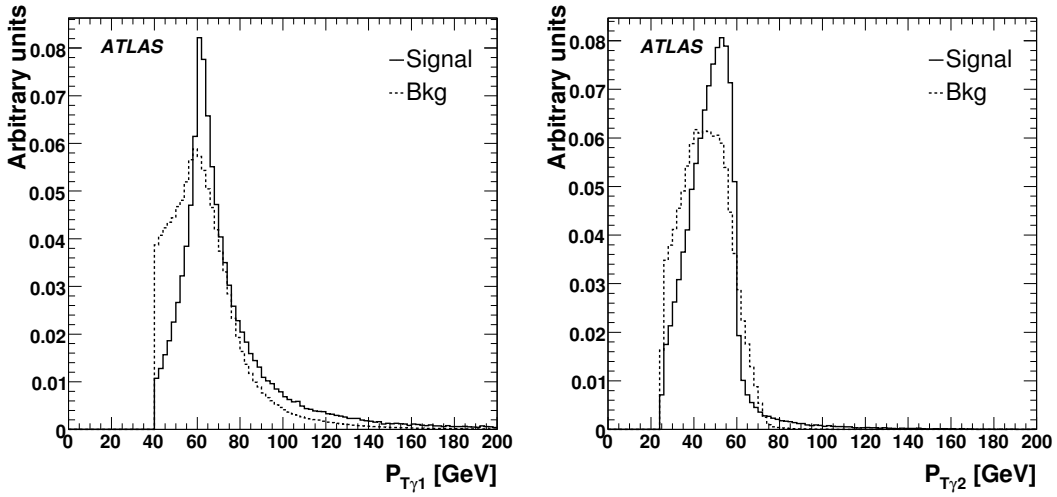


Figure 5.10: Transverse momentum distributions of the leading photon (left) and sub-leading photon (right) for signal ($m_H$ = 120 GeV) and background processes. The signal and background processes are summed according to cross-section. Histograms are normalized to unity.

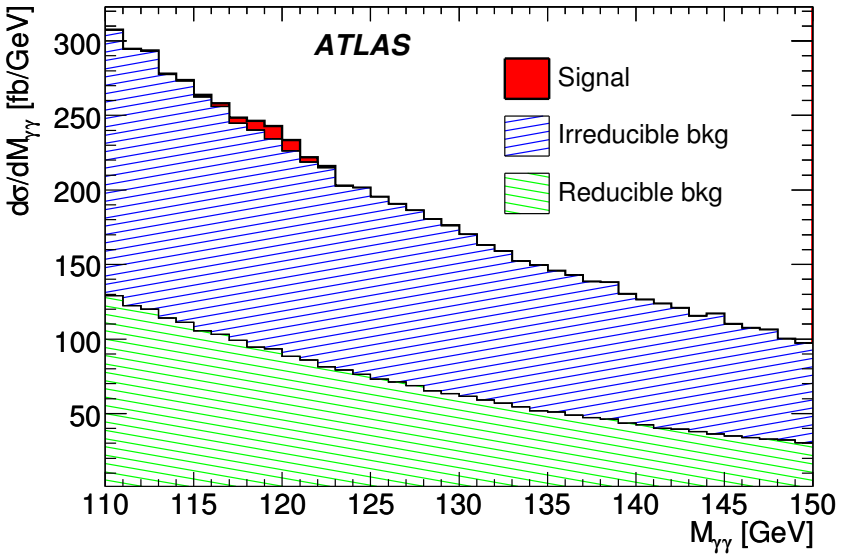


Figure 5.11: The di-photon invariant mass spectrum after the application of cuts of the inclusive analysis. Results are presented in terms of the expected cross-section. The contribution from various signal and background processes are presented in stacked histograms (see text).

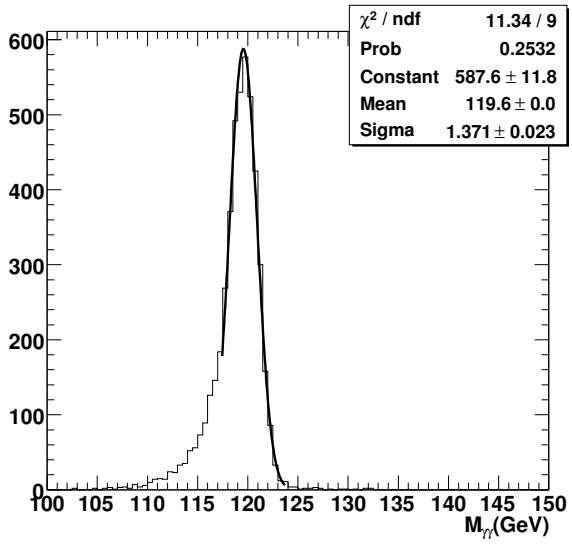


Figure 5.12: The $m_{\gamma\gamma}$ distribution for signal in the inclusive analysis, fit to a Gaussian. The fit range is roughly from $-1.5\sigma$ to $2\sigma$.

| Background Process | Cross-section (fb) |
|---|---|
| $\gamma\gamma$ | 562 |
| Reducible $\gamma j$ | 318 |
| Reducible $jj$ | 49 |

Table 5.6: Expected cross-sections (in fb) of backgrounds within a mass window, $m_{\gamma\gamma}$ of $\pm 1.4\sigma$ around 120 GeV in the case of no pileup. Cuts **Ia** and **Ib** were applied.

| Process | Cross-section (fb) |
|---|---|
| $gg \rightarrow H$ | 21 |
| VBF $H$ | 2.7 |
| $ttH$ | 0.35 |
| $VH$ | 1.3 |

Table 5.7: Expected cross-sections (in fb) of signal within a mass window, $m_{\gamma\gamma}$ of $\pm 1.4\sigma$ around 120 GeV. The results are given for the different signal processes without pileup. Cuts **Ia** and **Ib** were applied.

one fake photon constitutes 39 % of the total background, about a factor of two larger than evaluated in [55]. This increase is mostly attributable to three factors. First, a different method for the parametrization of the fake photon background is used here. Second, the budget of inactive material in front of the first layer of the calorimeter has increased with respect to the one used previously. Third, the contribution from fragmentation in the $\gamma j$ process is added here for the first time (see Section 5.1).

In comparison with other channels such as $H \rightarrow WW$, $H \rightarrow 4e$, the side band is extremely important for extracting background shape for $m_{\gamma\gamma}$ and other variables (see Section 5.3.4 too). It is necessary to check the stability of the $m_{\gamma\gamma}$ shape for background with varied cuts on $P_T$ of leading photon and subleading leading. Figure 5.13 shows $m_{\gamma\gamma}$ distribution with cuts $P_{T\gamma1,T\gamma2} > 50, 30$ GeV (upper left plot), $P_{T\gamma1,T\gamma2} > 45, 35$ GeV (upper right plot), $P_{T\gamma1,T\gamma2} > 40, 30$ GeV (lower left plot) and $P_{T\gamma1,T\gamma2} > 40, 25$ GeV (lower right plot). The background shapes look similar and no obvious turning point shows up in any of the plots. This sanity check helps to demonstrate the feasibility of varying the cuts on leading and subleading photon without significantly altering the background's $m_{\gamma\gamma}$ distribution.

### 5.3.2 Higgs boson + 1 jet analysis

The analysis selection presented in Section 5.3.1 does not consider the properties of the hadronic final state. In this Section and in Section 5.3.3 two event selections are presented that take into account the presence and properties of high $P_T$ hadronic jets in association with the photon pair. This analysis follows earlier studies in ATLAS using a fast detector simulation [31]

Parton level studies have indicated that searches for the Higgs boson in associ-

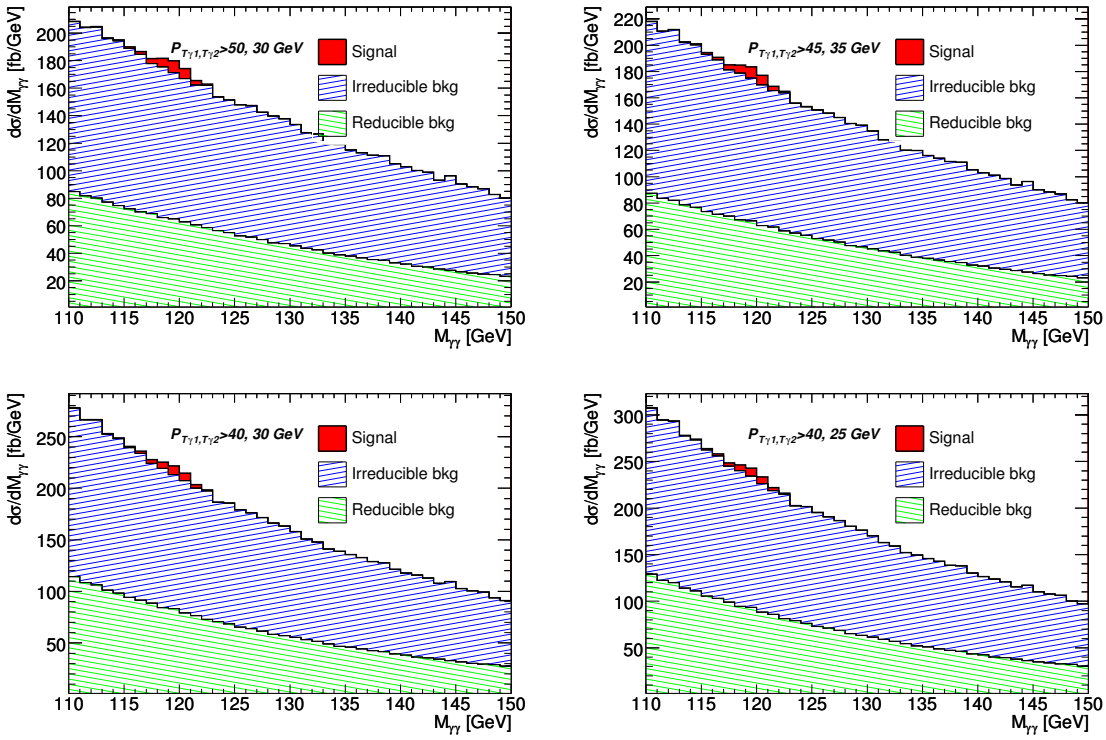


Figure 5.13: The di-photon invariant mass spectrum after the application of varied cuts of the inclusive analysis. Results are presented in terms of the expected cross-section. The upper left plot corresponds to $P_T$ cuts on leading and subleading photons at 50, 30 GeV respectively. The cuts on leading and subleading photons for the upper right plot are 40, 25 GeV. The lower left plot corresponds to $P_T$ cuts on leading and subleading photons at 40, 30 GeV and lower right is the standard one with cuts $P_{T\gamma1,T\gamma2} > 40, 25$ GeV.

ation with at least one high $P_T$ jet may have a strong discovery potential [44]. This analysis mainly exploits the fact that the gluon radiation pattern of the two leading Higgs boson production mechanisms strongly differ from the one expected for the reducible and irreducible backgrounds. The leading jet in the $gg \rightarrow Hj$ and $VBF$ mechanisms tends to be harder and more separated from the Higgs boson than in background events. The left plots in Figures 5.14-5.15 display the transverse momentum and the pseudo-rapidity of the leading jet for signal and backgrounds after the application of Cuts **Ia-Ib** in Section 5.3.1. The invariant mass of the di-photon and the leading jet in the event is a strong discriminating variable that can be used in the analysis to enhance the signal-to-background ratio. Figure 5.16 shows a comparison of the distributions of the invariant mass of the di-photon and leading jet system for signal and background processes after the application of cuts **Ia-Ib** in Section 5.3.1 and one can see that the invariant mass of the two photons and the jet system discriminates well the signal from the background.

The following event selection is chosen after the application of Cut **Ia**:

**IIa** Transverse momentum cuts of 45 and 25 GeV on the leading and sub-leading photon candidates, respectively.

**IIb** The presence of at least one hadronic jet with $P_T > 20$ GeV in $|\eta| < 5$.

**IIc** A cut on the invariant mass of the di-photon and the leading jet, $m_{\gamma\gamma j} > 350$ GeV.

The lower bound on the jet $P_T$ is dictated by the ability to calibrate hadronic jets in ATLAS [56]. The large hadronic activity due to underlying event and multiple proton-proton interactions at the LHC, in conjunction to the significant amount

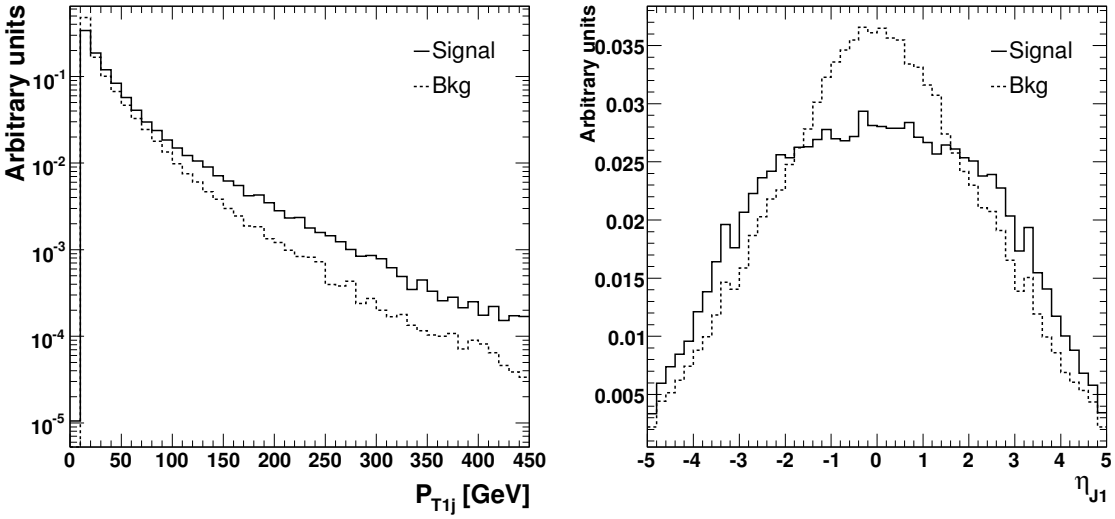


Figure 5.14: Transverse momentum distributions of the leading jet (left) and subleading jet (right) for signal and background processes after the application of Cuts **Ia-Ib** of the inclusive analysis (see Section 5.3.1). The contribution from different signal and background processes are added according to their cross-sections. Histograms are normalized to unity.

of inactive material before the calorimeter, may make it difficult to lower the $P_T$ threshold. The variable $m_{\gamma\gamma j}$ is the main discriminator used here to improve the signal-to-background ratio.

Figure 5.17 displays the resulting di-photon invariant mass spectrum after the application of Cuts **Ia** and **IIa-IIc**. The same procedure as in Figure 5.11 in Section 5.3.1 is used to obtain the histograms in Figure 5.17. The same codes for signal and backgrounds are used as in Figure 5.11. Figure 5.18 shows the signal's di-photon distribution after Cuts **Ia** and **IIa-IIc** and a Gaussian fit applied around the peak of the $m_{\gamma\gamma}$ distribution. The resolution is about 1.37 GeV for $m_H = 120$ GeV.

Tables 5.8 and 5.9 display the expected cross-sections for signal and background events in the range $110 < m_{\gamma\gamma} < 150$ GeV after the application of cuts **Ia** and **IIa-**

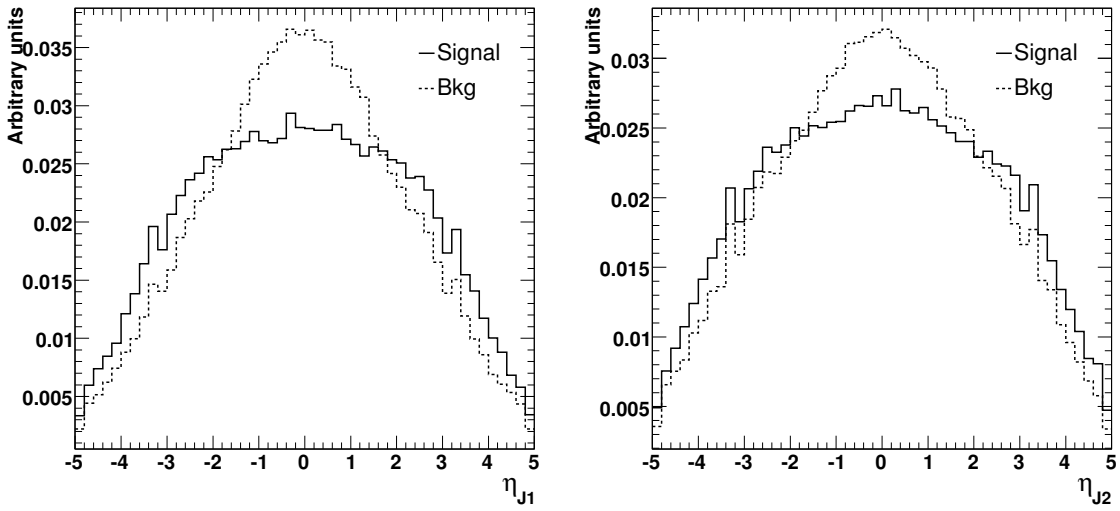


Figure 5.15: Pseudo-rapidity distributions of the leading jet (left) and sub-leading jet (right) for signal and background processes after the application of Cuts **Ia-Ib** of the inclusive analysis (see Section 5.3.1). The contribution from different signal and background processes are added according to their cross-sections. Histograms are normalized to unity.

**IIc**. Table 5.8 illustrates that the leading Higgs boson production mechanism after the application of cuts remains the $gg \rightarrow Hj$ process, closely followed by the VBF mechanism. It is important to note that we treat the $gg \rightarrow Hj$ process at LO ignoring the large QCD NLO corrections.

### 5.3.3 Higgs boson + 2 jets analysis

In this Section we consider an event selection comprising two photons in association with two high $P_T$ jets, or tagging jets. The tagging jets are defined as the two leading jets in the event. The plots on the left and right in Figures 5.20-5.25 show the $P_T$ and pseudo-rapidity of the leading and sub-leading jets for VBF signal process and background processes after the application of Cuts **Ia-Ib**. The VBF Higgs boson process at LO produces two high $P_T$ and relatively forward jets in opposite hemispheres

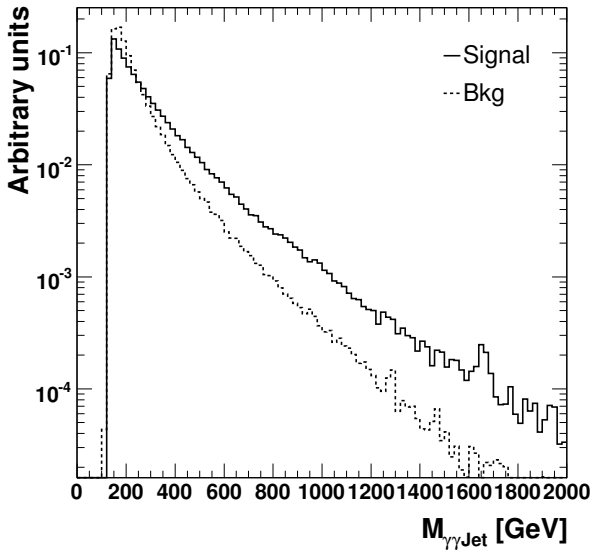


Figure 5.16: Distribution of the invariant mass of the di-photon and leading jet system for signals and backgrounds after the application of Cuts **Ia-Ib** (see Section 5.3.1). The contribution from different signal and background processes are added according to their cross-sections. Histograms are normalized to unity.

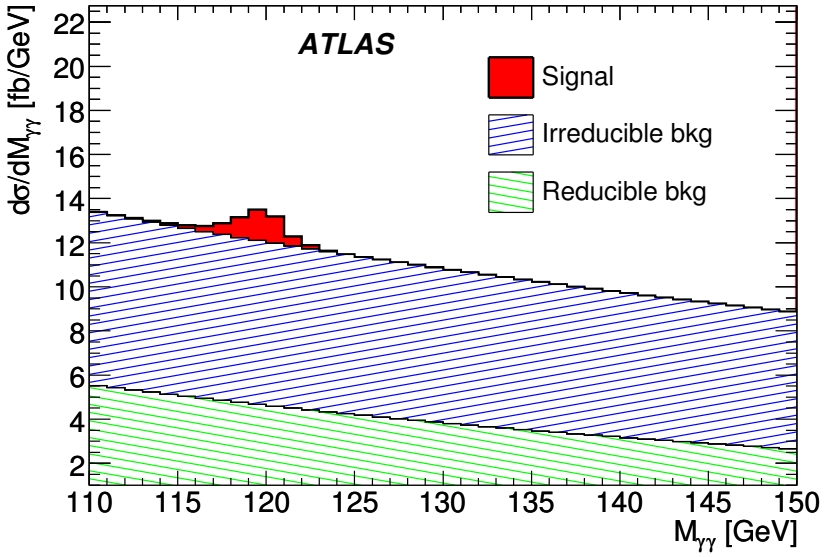


Figure 5.17: The di-photon invariant mass spectrum obtained with the Higgs boson + 1 jet analysis (see Section 5.3.2)(This plot is equivalent to Figure 9 in current verison of [34] except that the components of backgrounds' fluctuations due to MC statistics are depressed by smoothing their histogram curves.

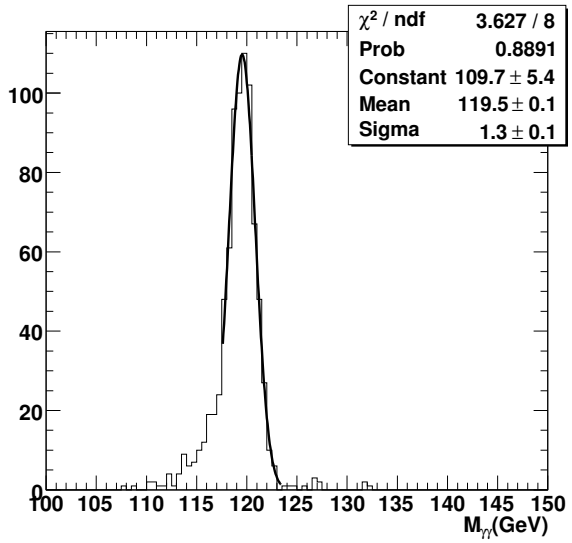


Figure 5.18: The $m_{\gamma\gamma}$ distribution for signal in the H+1 jet analysis, fit to a Gaussian. The fit range is roughly from $-1.5\sigma$ to $2\sigma$.

(backward-forward). The pseudo-rapidity gap and invariant mass of these jets tend to be significantly larger than the typical spectra for background processes. The NLO description of the VBF process does not significantly distort this picture.[1]

The plots in Figure 5.22 display the pseudo-rapidity gap between the tagging jets and their invariant mass, respectively. The contribution from different background processes (dashed histograms) are added according to their cross-sections. For simplicity, only the contribution from the VBF Higgs boson production mechanism is plotted (solid histograms).

A sizable contribution from the production of Higgs boson via gluon-gluon fusion is expected to appear at the LHC. This study is concerned with the feasibility of the

[1]About 10 % of the VBF events display the feature that a radiated gluon coming from one of the quark lines happens to become a tagging jet. In this class of events the pseudo-rapidity gap and the invariant mass of the tagging jets appear similar to what is displayed by a typical QCD background process. This effect is well reproduced by the HERWIG generator.

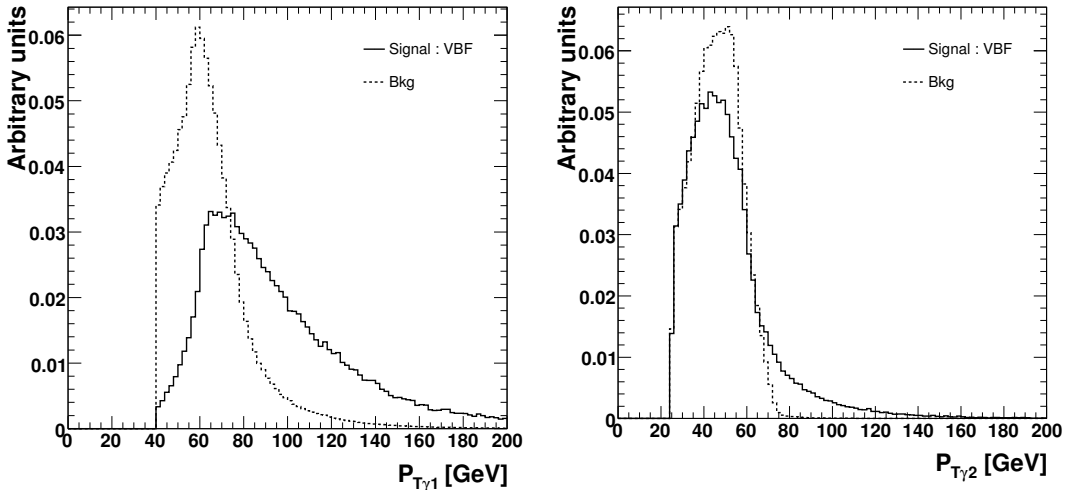


Figure 5.19: Transverse momentum distributions of the leading photon (left) and subleading photon (right) for signal from VBF process ($m_H = 120$ GeV) and background processes after the application of Cuts **Ia-Ib**. The background processes are summed according to cross-section. Histograms are normalized to unity.

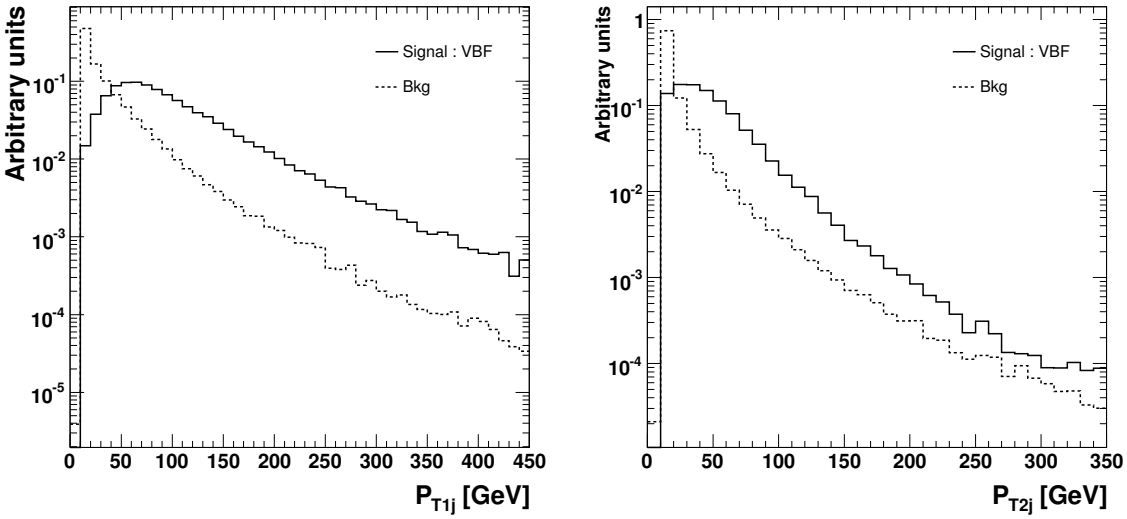


Figure 5.20: Transverse momentum distributions of the leading jet (left) and subleading jet (right) for signal from VBF process and background processes after the application of Cuts **Ia-Ib** of the inclusive analysis (see Section 5.3.1). The contribution from different background processes are added according to their cross-sections. Histograms are normalized to unity.

| Cut | $gg \to H$ | $VBFH$ | $VH$ | $ttH$ | Total |
|---|---|---|---|---|---|
| **Ia-IIa** | 28 | 3.6 | 1.7 | 0.49 | 34 |
| **IIb** | 13 | 3.5 | 1.5 | 0.49 | 19 |
| **IIc** | 3.2 | 1.9 | 0.22 | 0.17 | 5.5 |
| Mass Window | 2.3 | 1.4 | 0.17 | 0.13 | 4.0 |

Table 5.8: Expected cross-sections (in fb) for the Higgs boson + 1 jet Analysis. Results are given after the application of Cuts **Ia** and **IIa-IIc** (see Section 5.3.2). In the last row the expected cross-sections within a mass window of $m_{\gamma\gamma}$ of $\pm 1.4\sigma$ around 120 GeV are given.

| Cut | $\gamma\gamma$ | Reducible $\gamma j$ | Reducible $jj$ | EW $\gamma\gamma jj$ | Total |
|---|---|---|---|---|---|
| **Ia-IIa** | 9698 | 8498 | 937 | 99 | 19233 |
| **IIb** | 4786 | 4438 | 444 | 99 | 9768 |
| **IIc** | 501 | 824 | 89 | 71 | 1485 |
| Mass Window | 28 | 17 | 2.0 | 1.5 | 49 |

Table 5.9: Expected cross-sections (in fb) of background for the Higgs boson + 1 jet Analysis. Results are given after the application of cuts **Ia** and **IIa-IIc** (see Section 5.3.2). In the last row the expected cross-sections within a mass window of $m_{\gamma\gamma}$ of $\pm 1.4\sigma$ around 120 GeV are given. Trigger effect is applied and k-factors are 2.1 for $\gamma j$ and 1.3 for $jj$.

observation of a Higgs boson signal with a dedicated event selection meant to enhance the VBF signal. Nevertheless, the contribution from Higgs boson production via gluon-gluon fusion is considered as a signal processes.

A number of variables are chosen that are sensitive to the different kinematics displayed by the signal and background processes [57]. The following is the optimized event selection after the application of Cut **Ia**:

**IIIa** Transverse momentum cuts of 50 and 25 GeV on the leading and sub-leading photon candidates, respectively.

**IIIb** The presence of at least two hadronic jets in $|\eta| < 5$ with $p_T > 40$ and 20 GeV for

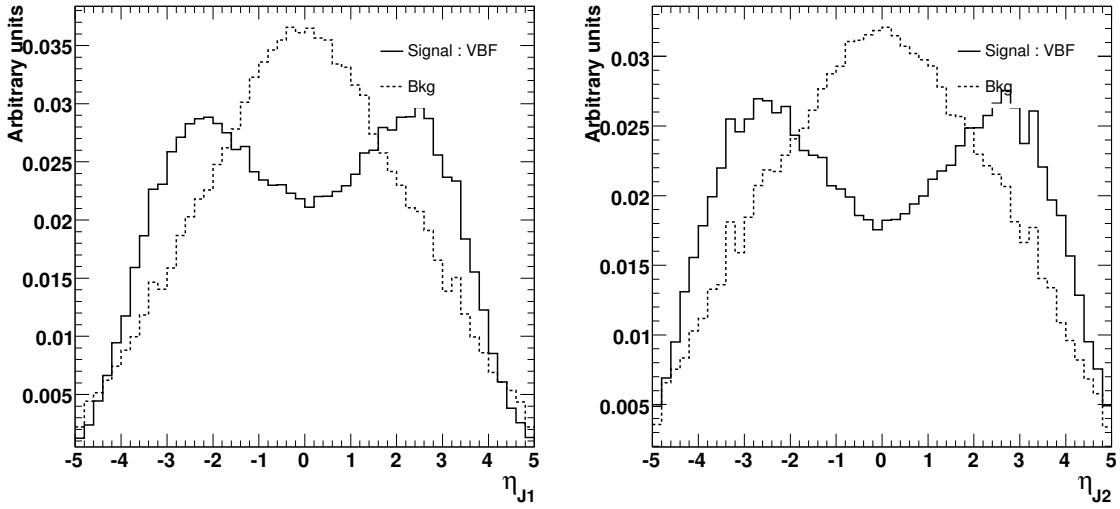


Figure 5.21: Pseudo-rapidity distributions of the leading jet (left) and sub-leading jet (right) for signal from VBF process and background processes after the application of Cuts **Ia-Ib** of the inclusive analysis (see Section 5.3.1). The contribution from different background processes are added according to their cross-sections. Histograms are normalized to unity.

the leading and sub-leading jet, respectively. Require that the tagging jets be in opposite hemispheres, $\eta_{j1} \cdot \eta_{j2} < 0$, where $\eta_{j1}$ and $\eta_{j2}$ correspond to the pseudo-rapidity of the leading and sub-leading jets, respectively. Finally, it is required that the pseudo-rapidity gap between the tagging jets be large, $\Delta\eta_{jj} > 3.6$.

**IIIc** Photons are required to be in between the tagging jets in pseudo-rapidity.

**IIId** Invariant mass of the tagging jets, $M_{jj} > 500$ GeV.

**IIIe** Veto on events with a third jet with $P_T > 20$ GeV and $|\eta| < 3.2$

The motivation of **IIIe**, namely the Central Jet Veto (CJV), is due to the fact that the presence of extra QCD radiation between the two jets exists in the backgrounds, but not in the signal processes. The study of the CJV effects were carried

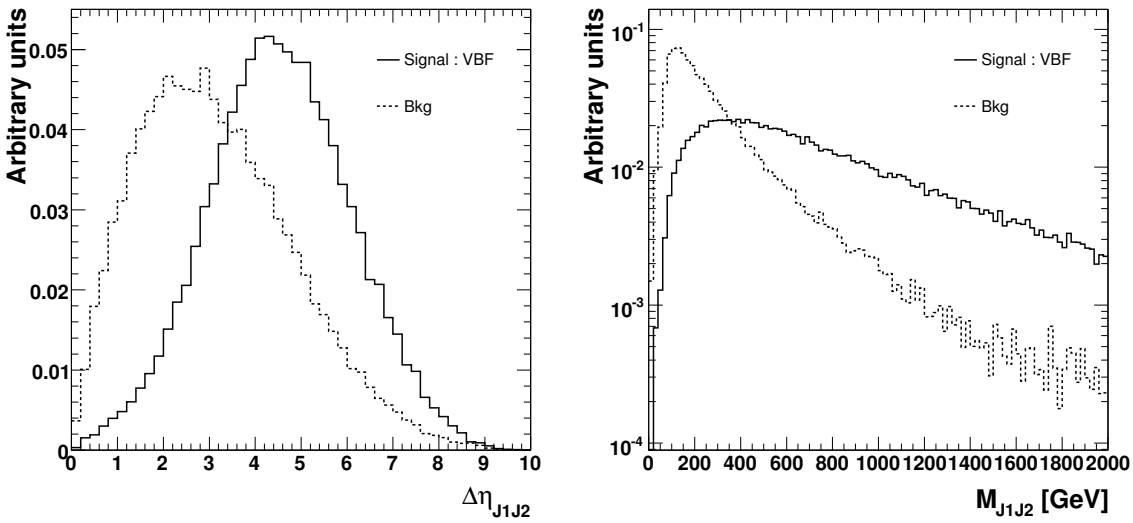


Figure 5.22: Distributions of the pseudo-rapidity gap between tagging jets (left) and their invariant mass (right) after requiring both jets in opposite hemispheres and cuts **Ia-Ib** (see text). The contribution from different background processes (dashed histograms) are summed according to their cross-sections. For simplicity, only the contribution from the VBF Higgs boson mechanism is plotted (solid histograms). Histograms are normalized to unity.

out in [58] by constructing a variable called $\eta^*$ which is sensitive to coherence effects among $\eta$ of jets:

$$\eta^* = \eta_3 - \frac{\eta_1 + \eta_2}{2}, \tag{5.1}$$

where $\eta_i$ is the pseudorapity of $i^{th}$ jet which is ordered in decreasing $P_T$. This is demonstrated in Figure 5.23 where the left plot shows the signal $P_T$ of third leading jet and $\eta^*$ for signal and background after Cuts **IIIa-IIId**.

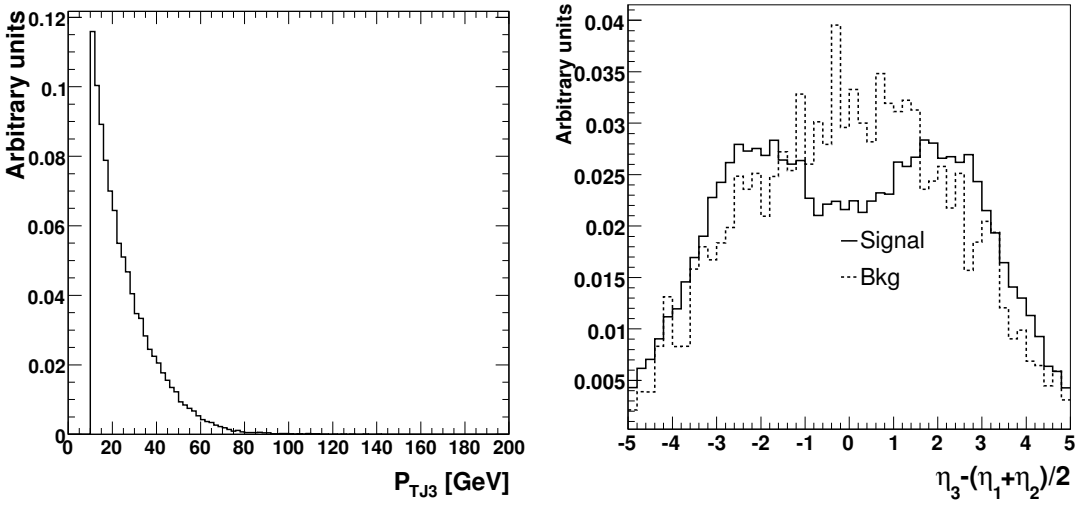


Figure 5.23: $P_T$ distribution of signal's third jet ordered in decreasing $P_T$ (left) and the distribution of $\eta^*$ for signal and background. The cuts of **IIIa-IIId** are applied beforehand.

Figure 5.24 displays the resulting di-photon invariant mass spectrum after the application of cuts **Ia** and **IIIa-IIIe**

Figure 5.25 shows the signal's di-photon distribution after Cuts **Ia** and **IIIa-IIIe** are applied and a Gaussian fit is performed around the peak of the $m_{\gamma\gamma}$. The resolution is about 1.5 for $m_H = 120$ GeV.

Tables 5.10 and 5.11 display the expected cross-sections for signal and back-

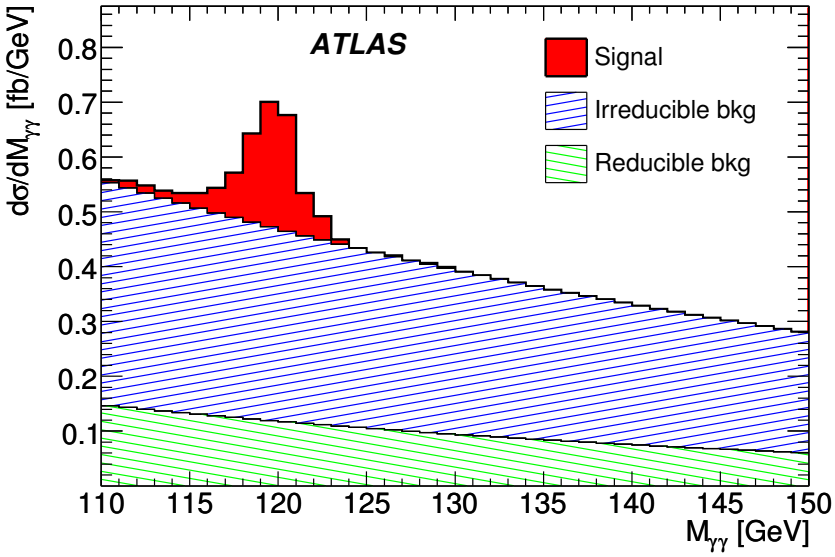


Figure 5.24: The di-photon invariant mass spectrum obtained with the Higgs boson + 2 jet analysis (see Section 5.3.3) (This plot is equivalent to Figure 10 in current verison of [34] except that the components of backgrounds' fluctuations due to MC statistics are depressed by smoothing their histogram curves.).

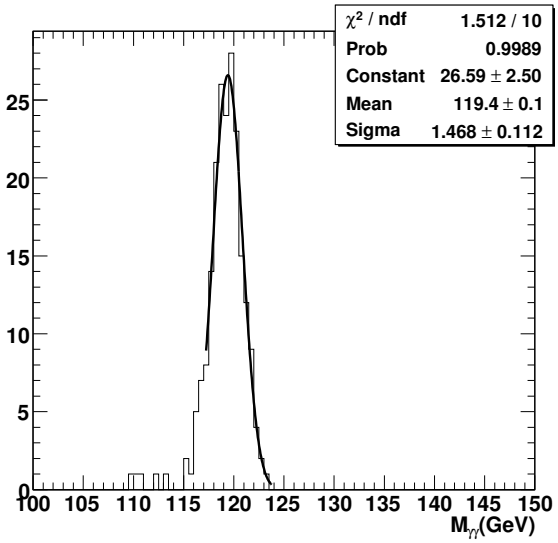


Figure 5.25: The $m_{\gamma\gamma}$ distribution for signal in the H+2 jets analysis, fit to a Gaussian. The fit range is roughly from $-1.5\sigma$ to $2\sigma$.

| Cut | $gg \to H$ | $VBFH$ | $VH$ | $ttH$ | Total |
|---|---|---|---|---|---|
| **Ia-IIIa** | 26.40 | 3.53 | 1.68 | 0.50 | 32.11 |
| **IIIb** | 0.63 | 1.44 | 0.02 | 0.01 | 2.10 |
| **IIIc** | 0.55 | 1.39 | 0.01 | 0.01 | 1.96 |
| **IIId** | 0.32 | 1.16 | 0.01 | 0.00 | 1.49 |
| **IIIe** | 0.25 | 1.03 | 0.00 | 0.00 | 1.28 |
| Mass Window | 0.18 | 0.79 | 0.00 | 0.00 | 0.97 |

Table 5.10: Expected cross-sections (in fb) for the Higgs boson + 2 jet Analysis. Results are given after the application of Cuts **Ia** and **IIIa-IIIe** (see Section 5.3.3). In the last row the expected cross-sections within a mass window of $m_{\gamma\gamma}$ of $\pm 1.4\sigma$ around 120 GeV are given.

| Cut | $\gamma\gamma$ | Reducible $\gamma j$ | Reducible $jj$ | EW $\gamma\gamma jj$ | Total |
|---|---|---|---|---|---|
| **Ia-IIIa** | 7417 | 6355 | 710 | 92 | 14574 |
| **IIIb** | 94 | 97 | 13 | 45 | 249 |
| **IIIc** | 70 | 69 | 9.9 | 41 | 189 |
| **IIId** | 33 | 34 | 5.6 | 38 | 111 |
| **IIIe** | 17 | 17 | 2.5 | 26 | 63 |
| Mass Window | 0.86 | 0.42 | 0.06 | 0.59 | 1.95 |

Table 5.11: Expected cross-sections (in fb) of background for the Higgs boson + 2 jet Analysis. Results are given after the application of Cuts **Ia** and **IIIa-IIIe** (see Section 5.3.3). In the last row the expected cross-sections within a mass window of $m_{\gamma\gamma}$ of $\pm 1.4\sigma$ around 120 GeV are given. The effect of trigger is considered here and the k-factors used are 2.1 for $\gamma j$ and 1.3 for $jj$.

ground events in the mass range $\pm 1.4\sigma$ around 120 GeV after the application of Cuts **Ia** and **IIIa-IIIe**. Table 5.10 shows that the dominant Higgs boson production mechanism surviving the events selection is the VBF mechanism, whose QCD NLO corrections are known to be small. Unfortunately the QCD NLO corrections to the main backgrounds included in Table 5.11 are not known; therefore, the results presented in 5.11 suffer from large theoretical uncertainties.

The overlap of events presented in this section and the Sections 5.3.2 is about

20%. This is particularly relevant for the VBF Higgs boson production mechanism. In Section 6.4.1 the signal significance of a combined analysis is presented that takes the event overlap into account.

### 5.3.4 Combined analysis of H+0,1,2jets and its optimization

In Section 5.3.1, Section 5.3.2 and Section 5.3.3, we discussed the traditional inclusive $H \to \gamma\gamma$, $H \to \gamma\gamma + 1\,\text{jet}$ where the jet is supposed to be hard and $H \to \gamma\gamma + 2\,\text{jets}$ which is a VBF analysis. The reason to introduce the second mode is based on the fact that the Higgs boson can be produced with large transverse momentum recoiling against a hard jet. For the third mode, due to the VBF mechanism, two forward hard jets and a clean central region can be exploited to identify the signal. However the disadvantage, especially for the third mode, is that the statistical fluctuations have a significant impact on the analysis at low luminosities like $10 - 20\,\text{fb}^{-1}$. On the one hand, in a combined analysis, one can make full use of various sensitivities introduced by using dynamic kinematic features of the final states $\gamma\gamma + 1\,\text{jet}$ and $\gamma\gamma + 2\,\text{jet}$. On the other hand, the statistical fluctuations from $\gamma\gamma + 2\,\text{jet}$ can be effectively compensated by $\gamma\gamma + 0\,\text{jet}$ and $\gamma\gamma + 1\,\text{jet}$. Technically, this can be realized by a simultaneous fit for those three subchannels; such a fit will be introduced in next chapter.

As illustrated in Figure 5.26, the analysis procedure is summarized as follows:

- Any event, which passes $H + 2\,\text{jet}$ Cuts (**IIIa-IIIe**), will be included in $H + 2\,\text{jet}$ subchannel;
- Otherwise, if it passes the $H + 1\,\text{jet}$ Cuts (**IIa-IIc**), it will be selected by $H + 1\,\text{jet}$ subchannel;
- Events failing both $H + 2\,\text{jet}$ and $H + 1\,\text{jet}$, will go to $H + 0\,\text{jet}$ if they still pass $H + 0\,\text{jet}$ Cuts (**Ia-Ib**);

- Event that fail all the cuts above are dropped.

It is obvious that there is no overlap among different sub-channels for combined analysis. A comparison of final cross-section with mass window of $m_{\gamma\gamma}$ of $\pm 1.4\sigma$ around 120 GeV between the combined analysis and the analysis of the Inclusive, $H+1$ jet and $H+2$ jets channels are shown in Table 5.12. Final cross-sections for $H+2$ jets and combined $H+2$ jets are same (as expected) and most events from $H+1$ jet and Inclusive are deposited in combined $H+1$ jet and combined $H+0$ jet. The overall number of events from $H+0$ jet and $H+1$ jet and $H+2$ jets in combined analysis should be equivalent to those in inclusive case since no event selected by inclusive analysis is dropped.

It has to be pointed out that the selections introduced in Section 5.3.1, Section 5.3.2 and Section 5.3.3 do not necessarily need to be optimized for combined analysis. Figures 5.27-5.28 display the background distributions of the kinematic variables such as $P_{T\gamma\gamma}$, $m_{\gamma\gamma j}$ above 200 GeV, the invariant mass $M_{j1j2}$ and the pseudo-rapidity $\Delta\eta_{j1j2}$ between leading and subleading jets with respect to different $m_{\gamma\gamma}$ spectra. These plots show that there are no strong correlations between $m_{\gamma\gamma}$ and the other kinematic variables. Thus it is feasible that one can extract the shapes of the discriminating variables for the background from the sideband in data while introducing minimal bias into the analysis. Of course, we have to depend on the SM prediction of those kinematic shapes for the signal.

After extracting those shape distributions, it is also possible to optimize the cuts on variables such as $P_{T\gamma\gamma}$, $M_{\gamma\gamma j}$, $M_{j1j2}$, $\Delta\eta_{j1j2}$ and the $P_T$ of the leading and subleading photons. An optimization based on current MC is performed with the help

of the MINUIT program and shows that the improvement to significance is less than 10% considering the shape of $m_{\gamma\gamma}$ distribution is roughly kept during the process. A similar result can be obtained with a Neural Net analysis.

| | Inclusive | H+1jet | H+2jet |
|---|---|---|---|
| Signal | 25.4 | 4.0 | 0.97 |
| Background | 929 | 49 | 1.95 |
| | H+0jet (combined) | H+1jet (combined) | H+2jet (combined) |
| Signal | 20.4 | 3.3 | 0.97 |
| Background | 883 | 48 | 1.95 |

Table 5.12: Expected cross-sections (in fb) of signal and background for the inclusive, H+1 jet and H+2 jets and combined H+0 jet, H+1 jet and H+2 jets within a mass window for $m_{\gamma\gamma}$ of $\pm 1.4\sigma$ around a central mass of 120 GeV.

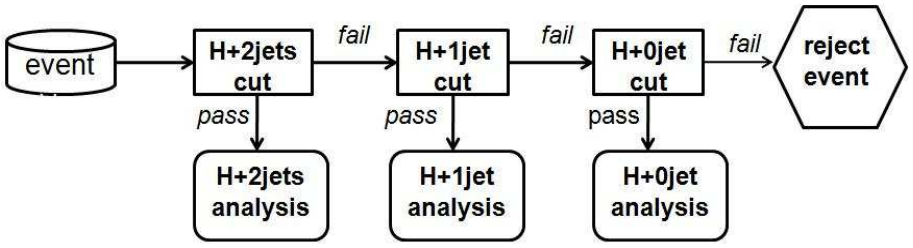


Figure 5.26: The block diagram of the strategy for the combined analysis of H+0, 1 and 2 jets.

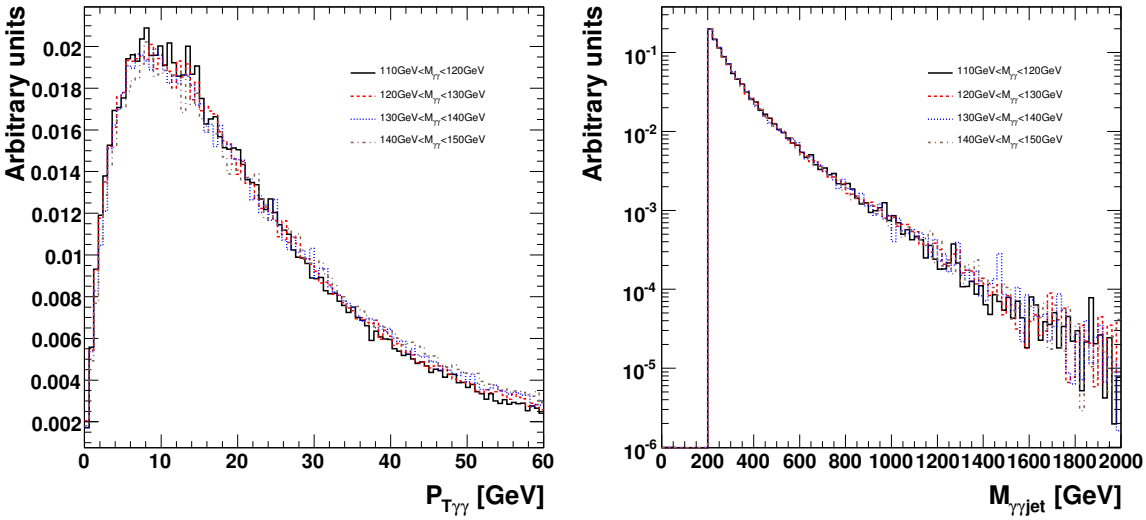


Figure 5.27: $P_{T\gamma\gamma}$ and $M_{\gamma\gamma j}$ distributions of background in different $m_{\gamma\gamma}$ bins. The cuts of **Ia-Ibo** are applied beforehand.

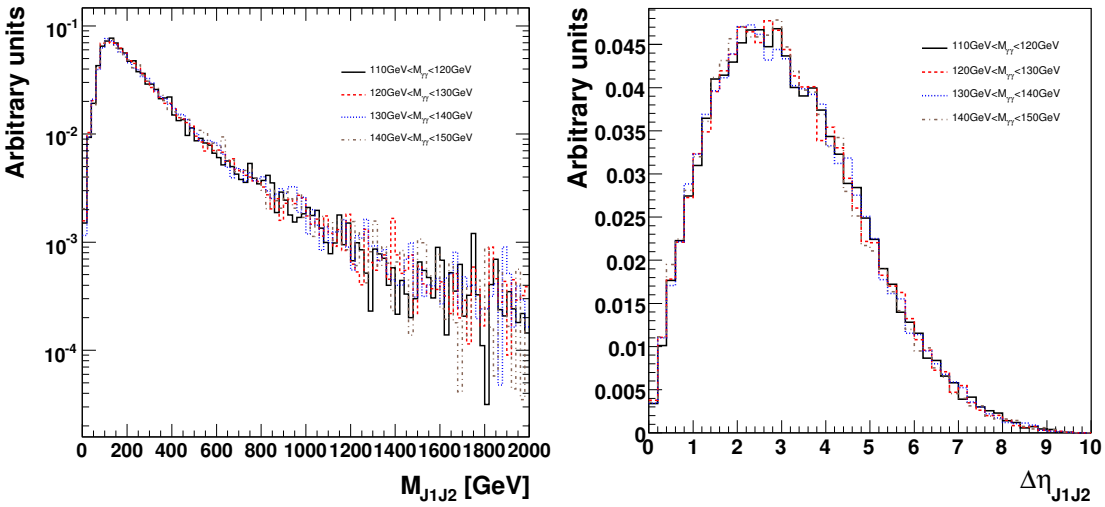


Figure 5.28: The distribution of invariant mass and pseudo-rapidity difference between leading and subleading jet for background in different $m_{\gamma\gamma}$ spectra as the Legends describe. The cuts of **IIIa-IIIb** are applied beforehand.

### 5.3.5 Conclusion

In the chapter, we present a cut based analysis on the inclusive, H+1 jet and H+2 jets analyses with NLO cross-sections for all signal and backgrounds. The result with mass scan has been shown in Table 5.13. Furthermore, a combined analysis of H+0 jet, H+1 jet and H+2 jets sub-channels is firstly performed in the chapter. Table 5.14 shows the result for the results with mass scan.

A number of directions are envisioned in order to further improve the sensitivity of the inclusive analysis. The feasibility of the optimization of the cuts based on data are discussed. The treatment of the photon identification with LLR or HMatix may potentially lead to improved sensitivity.

| | *Inclusive* | | *H+1jet* | | *H+2jets* | |
|---|---|---|---|---|---|---|
| $m_H$ (GeV) | S | B | S | B | S | B |
| 120 | 25.4 | 929 | 4.0 | 49 | 0.97 | 1.95 |
| 130 | 24.1 | 741 | 4.3 | 47 | 0.96 | 1.72 |
| 140 | 19.3 | 601 | 3.9 | 46 | 0.81 | 1.72 |

Table 5.13: Expected cross-sections (in fb) of signal and background for the inclusive, H+1 jet and H+2 jets as described in Section 5.3.1, Section 5.3.2 and Section 5.3.3 within a mass window for $m_{\gamma\gamma}$ of $\pm 1.4\sigma$ around central masses 120, 130 and 140 GeV.

| | *H+0jet* | | *H+1jet* | | *H+2jets* | |
|---|---|---|---|---|---|---|
| $m_H$ (GeV) | S | B | S | B | S | B |
| 120 | 20.4 | 883 | 3.3 | 48 | 0.97 | 1.95 |
| 130 | 19.2 | 695 | 3.5 | 46 | 0.96 | 1.72 |
| 140 | 14.6 | 557 | 3.3 | 44 | 0.81 | 1.72 |

Table 5.14: Expected cross-sections (in fb) of signal and background for the H+0 jet, H+1 jet and H+2 jets as described in Section 5.3.4 within a mass window for $m_{\gamma\gamma}$ of $\pm 1.4\sigma$ around central masses 120, 130 and 140 GeV.

# Chapter 6

# Maximum-likelihood fit for $H \rightarrow \gamma\gamma$

In addition to event counting, a maximum-likelihood fit method has been developed and widely implemented approaching the signal significance in ATLAS [59, 46, 60]. The statistical method adapted is a frequentist one and maximum-likelihood fit takes into account the systematic uncertainties during the process of the fit.

In this chapter, an unbinned extended a maximum-likelihood fit is performed to extract the signal significance for $H \rightarrow \gamma\gamma$. The cuts adapted in this chapter are those introduced in Sections 5.3.1-5.3.3. The signal sigificance extraction is developed both by including only discrimating variable di-photon invariant mass and by covering extra discriminating variables: the transverse momentum of $\gamma\gamma$ system $P_{TH}$ and the magnitude of the photon decay angle in the Higgs boson rest frame with respect to the Higgs boson lab flight direction, $|cos\theta^*|$. In this study, the signal shapes and relative normalizations are decided from theoretical predictions. So far, the background shapes are taken from the MC [34] and normalization are allowed to float during the fit process. In principle, as discussed in Section 5.3.4, the parametric shapes of the backgrounds can be effectively extracted from the sidebands of the $m_{\gamma\gamma}$ distribution.

## 6.1 Fit variables

### 6.1.1 Di-photon invariant mass

- **Signal parametrization**

  The $H \to \gamma\gamma$ distribution of $m_{\gamma\gamma}$ shows a Gaussian peak. However its left tail is longer than the right one, which is mostly due to either the energy losses before the EM Calorimeter or the leakage into Hadronic Calorimeter. This kind of asymmetric distribution can be modeled by *Crystal Ball* (CB) [61] function,

$$f_s(m_{\gamma\gamma}) = \begin{cases} e^{-t^2/2} & \text{if } t > -a \\ (\frac{n}{|a|}{}^n \cdot e^{-|a|^2/2} \cdot (\frac{n}{|a|} - |a| - t)^{-n} & \text{otherwise} \end{cases} \tag{6.1}$$

  where $t = (m_{\gamma\gamma} - m_H - \delta_{m_H})/\sigma(m_{\gamma\gamma})$, $N$ is a normalization parameter, $m_H$ is the Higgs boson mass, $\delta_{m_H}$ is a category dependent offset, $\sigma$ represents the di-photon invariant mass resolution, and where $n$ and $\alpha$ parametrise the non-Gaussian tail. More detailed descriptions can be found in [34].

- **Background parametrisation**

  The background distribution of $m_{\gamma\gamma}$ can be well modeled by an exponential tail so that within an effective mass window ($110 < m_{\gamma\gamma} < 150$ GeV), the following PDF is found to be appropriate

$$f_B(m_{\gamma\gamma}) = e^{-cm_{\gamma\gamma}} \tag{6.2}$$

  where $c$ is the exponential slope which can be determinated from the fit.

### 6.1.2 Higgs transverse momentum

- **Signal parametrisation**

  The distribution of the Higgs transverse momentum, $P_{TH}$, has a maximum at approximately 15 GeV, and exhibits a steep rise at left side of the peak and a long exponential tail beyond the maximum. The spectrum is harder for events with recoiling jets. The distributions can be model by a sum of three exponential polynomials times the pow of $P_{TH}$,

$$f_S(P_{TH}) = N \cdot \sum_{i=1}^{3} P_{TH}^{\lambda_i} e^{-c_i P_{TH}} \tag{6.3}$$

  of which one term mainly accounts for the strong rise at low $P_{TH}$. Another candidate can be Landau distribution.

- **Background parametrisation**

  Di-photon transverse momentum for background show similar distribution as that for signal, with however a softer spectrum. Equation 6.3 is feasible to be applied on the background.

### 6.1.3 Higgs decay angle

- **Signal parametrisation**

  The phase space of $|cos(\theta^*)|$ for the signal is supposed to be isotropic in the center of mass system of the two photons. However, acceptance effects due to Cuts **Ia-Ib** from Sec. 5.3.1 suppress $|cos(\theta^*)|$ values around one. The PDF can be interpolated by a summation of several exponential distributions.

$$f_S(|cos(\theta^*)|) = N \cdot (\sum_{i=1}^{3} e^{-c_n|cos^i(\theta^*)|}) \tag{6.4}$$

- **Background parametrisation**

  The $t$-channel (such as Diagram (a) of Figure 5.1 shows) and the quark or gluon fragmentation at NLO, give rise to the small $\theta^*$ distribution in the center-of mass system of the two photons. In other words, the $|cos(\theta^*)|$ distribution exhibits some enrichment towards large values. A similar paramterization for the signal or a more sophisticated one can describe the shape for background.

## 6.2 Fit classifications

Fit classifications mean that we can divide the sample into several branches according to some similar properties. The reason that the classifications are introduced in the fit study and so that it can provide a finer, more accurate description of the likelihood model. Moreover, it can be possible to enhance the signal and background distinction due to various kinematics. Therefore, subdivision into different classifications can enhance the signal significance. However, the more classifications introduced, the less statistics one will have in the individual models which can enhance the uncertainties of the models.

### 6.2.1 Pseudo-rapidity classifications

The idea of introducing pseudo-rapidity [45, 46] classifications is that photons with different pseduorapidities have different resolutions due to the different responses

of the detector. One can classify photon pairs with good, reasonable and bad reconstructed Higgs resolutions which is described in detail in [62, 34]. Another kind of similar but more natural pseudo-rapidity classification is that the photon pairs can be divided according to the place of their hits in the EM calorimeter, namely barrel-barrel (good resolutions), endcap-endcap (reasonable resolutions) and barrel-endcap (bad resolutions).

### 6.2.2 Jet classifications

As described in Section 5.3.4, the inclusive analysis can be divided into three disjunct sub-channels H+0 jet, H+1 jet and H+2 jets. Thus, in the fit method, the cuts in H+0 jet, H+1 jet and H+2 jets are inherited and samples are separated with Higgs boson with zero, one and two accompanying hard jets.

## 6.3 Likelihood Model

First, we consider separating the sample into three jet classifications. For H+0 jet and H+1 jet classifications, three $\eta$ classifications are introduced for each of them. Taking into account the low statistics of the H+2 jets classification, we didn't separate it further into $\eta$ classifications. The number of entries $n_c$ in classification $c$ is modeled as a Poisson variables with a mean value $E$:

$$E[n^c] = \mu s^c + b^c \tag{6.5}$$

where $\mu$ is defined as the strength parameter; $\mu = 0$ corresponds to the absence of a signal; $\mu = 1$ gives the signal rate $s^c$ expected from Standard Model; $b^c$ is the expected number of background events in classification $c$. The parameters of most interest for a Higgs search are $m_H$ and $\mu$ . All other parameters to describe the

signal and background shapes (such as those which can be adjusted or fixed are called nuisance parameters. The notation $p = (p_s, p_b)$ is used to refer to all of the nuisance parameters.

From Equation 6.5, the probability density function (PDF) $f_i^c$ for an event $i$ in classification $c$ is explicitly given by

$$f_i^c(\mu, p^c) = \mu\rho_s^c\rho f_{si}^c(p^c) + (1-\rho)f_{bi}^c(p^c), \tag{6.6}$$

where $\rho$ is the fraction of overall signal events over total events. $\rho_s^c$ the fraction of signal events in classification $c$ and $\sum \rho_s^c = 1$. $f_{si}^c$,$f_{si}^c$ are signal and background PDFs respectively. Equation 6.6 can also be written as the numbers of signal and background events instead of a fraction.

$$f_{Ei}^c(\mu, p^c) = \mu N_s^c f_{si}^c(p^c) + N_b^c f_{bi}^c(p^c), \tag{6.7}$$

where $N_s^c$ is the number of signal events in classification $c$, $N_b^c$ is the number of background events found in classification $c$. The number of expected events by the model in classification $c$ is $N^c = N_s^c + N_b^c$.

In general,

$$f_{S(B),i}^c(p^c) = \prod_{k=1}^{n_{var}} f_{S(B)}^c(x_{k,i}, p^c) \tag{6.8}$$

where $x_{k,i}$ are the discriminating variables used and $p^c$ are parameters for the classification $c$.

In particular cases of $H \to \gamma\gamma$, the discriminating variables $x_{k,i}$ can be $P_{TH,i}$ and $|cos(\theta_i^*)|$ as well as $m_H$, The $n_{var}$ involves three $\eta$ classifications for $H + 0$ jet and

three $\eta$ classifications for $H+1$ jet and just one overall $\eta$ classification for $H+2$ jets due to the high statistic fluctuations for luminosity such as 10 fb$^{-1}$.

Finally, the extended likelihood over all classifications is

$$\mathcal{L} = \prod_{t=1}^{n_{var}} e^{-N^c_{exp}} {N^c_{exp}}^{N^c_{obs}} \prod_{i=1}^{N^c_{obs}} f^c_i \tag{6.9}$$

Here the term $e^{-N^c_{exp}} {N^c_{exp}}^{N^c_{obs}}$ accounts for the poisson fluctuations in the number of events observed in each classification. $N^c_{obs}$ denotes the actual number of events observed in data. $1/N^c_{obs}!$ is omitted since it is a constant term in the minimization process. Equation 6.9 can equivalently be written as:

$$\mathcal{L}_| = \prod_{t=1}^{n_{var}} e^{-N^c_{exp}} \prod_{i=1}^{N^c_{obs}} f^c_{Ei} \tag{6.10}$$

Technically, the quantity to be minimized by the likelihood fit using *Minuit* in ROOT via the likelihood fit package RooFit [63] is $-\log(\mathcal{L})$, which is called Negative log-likelihood ($NLL$),

$$NLL(\mu, p) = \sum_{t=1}^{n_{var}} (N^c_{exp} - \sum_{i=1}^{N^c_{obs}} \log(f^c_{Ei})) \tag{6.11}$$

## 6.4 Fit Performance to investigate the discovery and exclusion

### 6.4.1 The Computation of the p-value

In this section, we consider two hypotheses, the background hypothesis (null hypothesis) with $\mu = 0$, assuming the background only in the observed distribution. The alternative hypothesis is the one with $\mu = 1$ assuming the presence of signal and

background. To establish discovery, we will try to reject the null hypothesis. On the contrary, one wants to reject the hypothesis $\mu = 1$ for excluding a SM Higgs discovery.

In general, to test a hypothesis with some specified $\mu$, the $\Delta(-\log(\mathcal{L}))$ is constructed,

$$\Delta NLL(\mu) = NLL(\mu, \hat{\hat{p}}) - NLL(\hat{\mu}, \hat{p}) \tag{6.12}$$

where $\hat{\hat{p}}$ denotes the value of $p$ that minimizes $NLL$ for the specified $\mu$ (e.g. $\mu = 0$ for discovery, $\mu = 1$ for exclusion); $\hat{\mu}$ and $\hat{p}$ are the estimators to minimize the $NLL$.

Taking into account that expected signal events $N_s \geq 0$, one can see that $\Delta NLL \geq 0$ with $\Delta NLL = 0$ implying good agreement between the data and the hypothesized value of $\Delta NLL$.

The evaluation of the compatibility between data and the hypothesis can be quantified by the p-value

$$p_{value}(\mu) = \int_{\Delta NLL_{obs}}^{\infty} \mathcal{F}(\Delta NLL) d\Delta NLL \tag{6.13}$$

where $\mathcal{F}(\Delta NLL)$ is the distribution for $\Delta NLL$. Here the lower limit of the integral is the observed (measured) $\Delta NLL_{obs}$. The higher incompatibility between the measurement and the hypothesis, the greater $\Delta NLL$ will be. Consequently, the smaller p-value is expected as illustrated by left the plot of Figure 6.1.

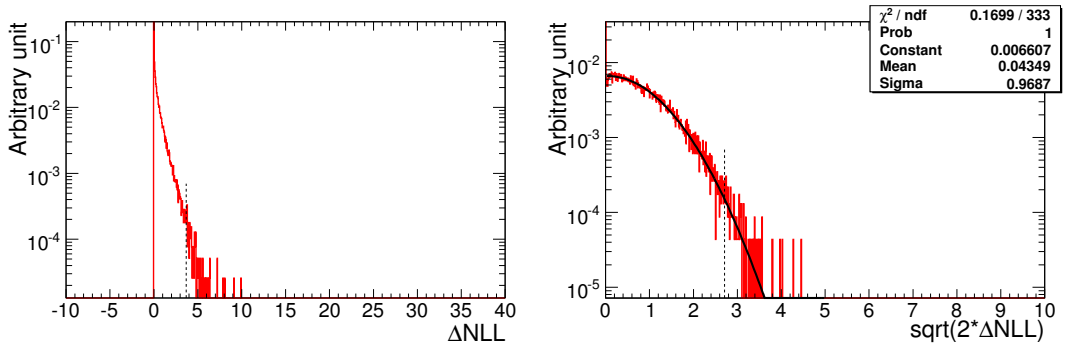


Figure 6.1: Illustration of the p-value computation. The curve in the left plot which peak at zero is the distribution of $\mathcal{F}(\Delta NLL)$ with the constraint $N_s \geq 0$ resulting in the non-negative distribution. The p-value for the observation of $\Delta NLL_{obs} = 3.8$ as x-coordinate of the dashed line displays is normalized filled area of the tail. The right plot shows the distribution of $\mathcal{F}'(\sqrt{2 \cdot \Delta NLL})$ using a fixed mass Higgs mass during the fit process.

### 6.4.2 Discovery and Exclusion

To establish discovery, we try to reject the null assumption with $\mu = 0$. The p-value in this case, is

$$p_{value}(0) = \int_{\Delta NLL_{obs}}^{\infty} \mathcal{F}(\Delta NLL(0)) d\Delta NLL(0) \tag{6.14}$$

Normally, the distribution of $\mathcal{F}(\Delta NLL)$ is a $\chi^2$ with $N_{d.o.f}$ degrees of freedom where $N_{d.o.f}$ is the difference of free parameters for the background hypothesis and the signal+background hypothesis fit. In the particular case, when only the normalization for signal is allowed to float (the other parameters such as $m_H$ and shapes of the signal parameters are fixed), the distribution of $\mathcal{F}(\Delta NLL)$ follows the distribution of a $\chi^2$ with one degree of freedom, or equivalently, $\mathcal{F}'(\sqrt{2 \cdot \Delta NLL})$ follows the standard Gaussian distribution with $mean = 0$ and $resolution = 1$ as the right plot of Figure 6.1 displays. Similar to Equation 6.13, we have

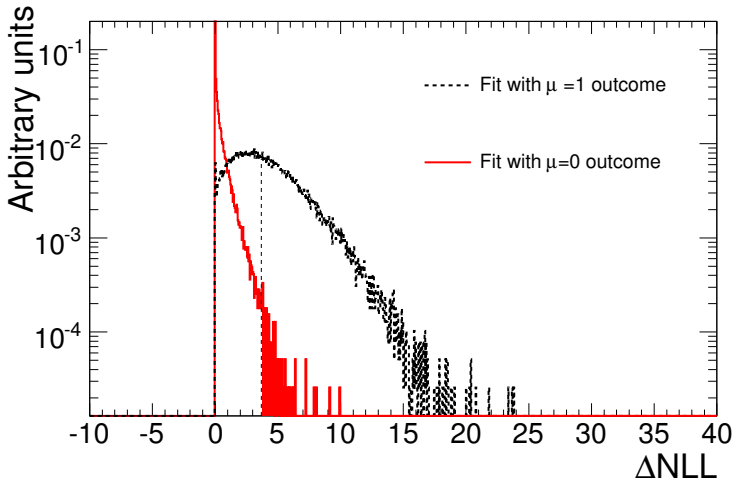


Figure 6.2: The distribution of $\Delta NLL$ for SM Signal+Background outcomes (dashed curve) and that for Background-only outcomes. The x-coordinate corresponds the median value for the distribution of SM signal+background outcomes. The solid curve is the background-only outcomes. The p-value can be computed from the filled area in that curve which is just the integral of the median value to infinity in that curve.

$$p_{value}(\mu) = \int_{\sqrt{2\cdot\Delta NLL_{obs}}}^{\infty} \mathcal{F}'(\sqrt{2\cdot\Delta NLL_{obs}})d\sqrt{2\cdot\Delta NLL_{obs}} \tag{6.15}$$

For the latter case, the significance is defined as the number of standard deviations $\sigma$ given some p-value as the x-coordinate of the dashed line exhibits. $\sigma$ here is called the discovery significance. The relation between p-value and $\sigma$ is

$$p_{value} = \int_{\sigma}^{\infty} \frac{1}{\sqrt{2\pi}} e^{\frac{-x^2}{2}} dx = 1 - \phi(\sigma) \tag{6.16}$$

Comparing Equation 6.15 and Equation 6.16, it is obvious that $\sigma = \sqrt{2\cdot\Delta NLL}$. In the general case, where $N_{d.o.f} > 1$, we can find a $\sigma$ from the standard Gaussian such that the p-value from it is equal to the observed one computed from the distribution of $\mathcal{F}(\Delta NLL)$.

We usually report the median significance under the assumption that the signal is

present at $\mu = 1$. where $\sigma_{med}$ and $p_{value_{med}}$ correspond to the median signal significance and p-value related to the median respectively.

Figure 6.2 helps to illustrate the discovery significance calculation from the fit. The dashed curve is the outcomes with the signal, i.e. $\mu = 1$. The vertical dashed line corresponds to the median of the curve. The solid curve is the one with background-only outcomes distribution. The integral of this curve from the x coordinate to infinity is essentially the p-value which is technically equivalent to the normalized filled area as one can see from the plot. Then it is easy to convert the p-value to signal significance [1].

In addition to rejecting the $\mu = 0$ hypothesis, we are also interested in rejecting some non-zero $\mu'$, i.e. setting an exclusion limit. The process of the setting limit is

- First for a given luminosity, we compute the p-value following Equation 6.13. This is similar to the procedure of discovery except for replacing the $\mu = 0$ hypothesis with the $\mu = \mu'$ hypothesis during the fit process.
- We scan with different $\mu$ (i.e. $0.1 \leq \mu < 2$ with step 0.1) and find the upper limit of $\mu$ for which the p-value is not less than a fixed confidence level (CL), typically 95%. Sometimes the $\mu$ for the CL with $\pm 1\sigma$ and $\pm 2\sigma$ fluctuations are also provided.
- One can also repeat the process with the luminosity scan.

The signal uncertainty has an impact on the Standard Model prediction. Table 6.1- 6.2 show the estimated signal systematics and their effect on the signal efficiency (also see [64]). A Gaussian term with the signal efficiency uncertainty as the

[1] In ROOT, the function $p_{value} = TMath :: Erfc(Z/\sqrt{2})$ relates the p-value with significance.

resolution can be added while fitting with a non-zero $\mu'$ hypothesis for an exclusion study. We implemented different kinematic variables and classifications while computing the signal significance as Table 6.3 shows. The resulting median likelihood ratio for exclusion, $\lambda(\mu)$ (using toy background only MC and taking the median of the $\lambda(\mu)$ distribution, is given in Table 6.4) for Higgs boson mass of 120 GeV at some given luminosity and $\mu = 1$ which corresponds to a SM Higgs boson.

| source | Relative effect(%) |
|---|---|
| luminosity | 3 |
| $\gamma$ ID eff. | 0.2 |
| $\gamma$ fake rate | 20 |
| $\gamma$ energy scale | 0.5 |
| $\gamma$ resolution | 0.5 |
| jet energy scale | 7 |
| jet resolution | $75\%\sqrt{(E)} + 7\%$ (when $\|\eta\| < 3.2$)<br>$110\%\sqrt{(E)} + 10\%$ (when $\|\eta\| > 3.2$) |

Table 6.1: Estimated scale of signal systematics.

| *source* | *Inclusive* | | *H+1 jet* | | *H+2 jets* | |
|---|---|---|---|---|---|---|
| | gg | VBF | gg | VBF | gg | VBF |
| luminosity | 3 | 3 | 3 | 3 | 3 | 3 |
| $\gamma$ ID eff. | $\pm$ 0.3 | $\pm$ 0.4 | $\pm$ 0.3 | $\pm$ 0.4 | $\pm$ 2.3 | $\pm$ 0.4 |
| $\gamma$ fake rate | $\pm$ 0.1 | $\pm$ 0.0 | $\pm$ 0.0 | $\pm$ 0.0 | $\pm$ 0.8 | $\pm$ 0.1 |
| $\gamma$ energy scale | $\pm$ 0.2 | $\pm$ 0.2 | +0.6/-0.5 | +0.5/-0.7 | $\pm$ 0.0 | +0.3/-0.2 |
| $\gamma$ resolution | $\pm$ 0.1 | $\pm$ 0.0 | $\pm$ 0.0 | $\pm$ 0.0 | $\pm$ 0.0 | $\pm$ 0.1 |
| jet energy scale | N/A | N/A | +10./-13. | +5.5/-6.1 | +19./-23. | +4.9/-8.7 |
| jet resolution | N/A | N/A | $\pm$ 0.2 | $\pm$ 0.1 | $\pm$ 2.3 | $\pm$ 0.6 |
| total | 3.0 | 3.0 | +10./-13. | +6.3/-6.9 | +19./-24. | +5.8/-9.2 |

Table 6.2: The impact (%) of signal systematics on the signal efficiency. where gg means the gg Fusion process and VBF means the VBF process.

| variables | Classifications | $\sigma^{Fix}$ | $\sigma^{Floating}$ |
|---|---|---|---|
| $m_{\gamma\gamma}$ | - | 2.4 | 1.5 |
| $m_{\gamma\gamma}$ | $\eta$ | 2.5 | 1.7 |
| $m_{\gamma\gamma}$ | $\eta$ and jet | 3.1 | 2.6 |
| $m_{\gamma\gamma}$, $P_{TH}$ | $\eta$ and jet | 3.4 | - |
| $m_{\gamma\gamma}$, $\|cos\theta^*\|$ | $\eta$ and jet | 3.3 | - |
| $m_{\gamma\gamma}$, $\|cos\theta^*\|$ | $\eta$ and jet | 3.6 | 2.8 |

Table 6.3: $H \rightarrow \gamma\gamma$ discovery potential for various likelihood configurations with a Higgs mass at 120 GeV and an integrated luminosity of 10 fb$^{-1}$. $\sigma^{Fix}$ means the significance from a fixed Higgs mass scenerio and $\sigma^{Floating}$ corresponds to that from a floating mass scenerio.

| L (fb $^{-1}$) | 1 | 2 | 5 | 10 | 30 |
|---|---|---|---|---|---|
| $-2\log(q_\mu)(\mu = 1.0)$ | 0.1089 | 0.4624 | 1.8225 | 4.5796 | 10.4976 |

Table 6.4: Exclusion: the median $-2\log(q_\mu)(\mu = 1.0)$ for a Higgs boson mass of 120 GeV and a few luminosities.

### 6.4.3 The Look-elsewhere effect

So far, we compute the p-value of background-only outcomes for a given mass. The Look-elsewhere effect in HEP addresses this probability of false discovery due to floating the Higgs mass and its impact on the discovery sensitivity [65, 66, 67]. In this scenario, the Higgs mass is technically treated as one of the nuisance parameters during the fit process. The Higgs mass distributions of the Background-only outcomes and the Signal+Background outcomes are shown in the left and right plot of Figure 6.3, respectively. As expected, the left plot shows that the possibility of a false discovery for signal+background outcomes is very low. It is also expected to see that the distribution of false discovery for Background-only outcomes is more or less flat within the range considered as right plot presents. However some edge effects appear as one notices two spikes at 110 GeV and 140 GeV in the plot. Fortunately, it doesn't introduce a significant bias for $\Delta NLL(0)$ distribution as Figure 6.4 illustrates. Migrating from a fixed mass scenario to one with floating mass, the variance of the median of $\Delta NLL$ for signal+background is small as the solid and dotted black curves in Figure 6.5 show. However, the tail of the $\mathcal{F}(\Delta NLL(0))$ distribution follows a $\chi^2$ with $N_{d.o.f}$ larger than one (a floating mass introduces the extra degree of freedom, see the discussion in Section 6.4.2). The change enhances the p-value by a factor of 8, which equivalently decreases the significance from 2.4 to 1.5 as the first row of Table 6.3 presents. In the Higgs mass range from 120 to 140 GeV, for $H \to \gamma\gamma$, the Higgs mass resolution varies in the range from 1.4 GeV to 1.6 GeV. The variation has been parametrized with a linear function (see Figure 6.6). The impact of the mass dependency of the

Higgs mass resolution on the signal significance is negligible, as Table 6.5 shows.

In principle, as suggested in [68], the relation between a fixed mass p-value and one from a floating mass can be described as,

$$p'_{value} = p_{value} \cdot \Delta m_H / \sigma \tag{6.17}$$

where $p'_{value}$ is for the floating mass and p-value is for the fixed mass case. $\Delta m_H$ is the floating mass range, which is 110-140 GeV for $m_H = 120$, 130 GeV and 120-150 GeV for $m_H = 140$ GeV. $\sigma$ is the Higgs mass resolution. This parameterization works reasonably well for relatively high significance values as Table 6.6 describes. However for low significance value this method is not applicable.

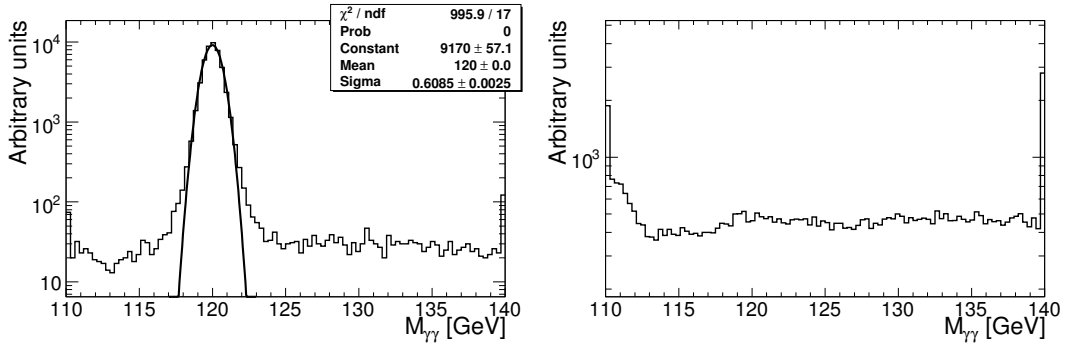


Figure 6.3: The left plot shows the fitted Higgs mass distribution for signal+background outcomes. In the toyMC, the true Higgs mass is at 120 GeV. In most cases, the Higgs mass is well fitted. These outcomes roughly correspond to 10 fb$^{-1}$ inclusive $H \to \gamma\gamma$ data. The right plot shows same distribution but for background-only outcomes.

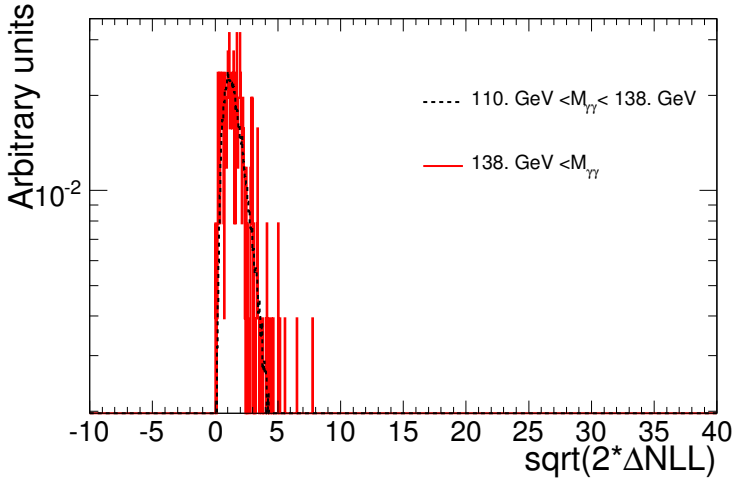


Figure 6.4: $\Delta NLL(0)$ distributions w.r.t $110\,GeV \leq m_H \leq 138\,GeV$ (dotted line) and for $130\,GeV \geq m_H$ in the right plot of Figure 6.3. One can see these two distributions are consistent which can illustrate the spark introduced in right plot of Figure 6.3 does not bias $\Delta NLL(0)$ distribution.

| $m_H$ | 120 | 130 | 140 |
|---|---|---|---|
| $\sigma(S,B)$ from para. | 1.46 | 1.83 | 1.29 |
| $\sigma(S,B)$ from fixed mass resolution | 1.45 | 1.88 | 1.32 |
| variation | -0.01 | 0.05 | 0.03 |

Table 6.5: Comparison of the signal significance $\sigma(S,B)$ obtained from using a parameterized Higgs mass resolution and a fixed resolution. As the third row shows, the difference between them is negligible.

| $\sigma(S,B)$ $m_H$ fixed | 4.80 | 3.61 | 2.42 | 1.25 |
|---|---|---|---|---|
| $\sigma(S,B)$ $m_H$ floating | 4.40 | 2.85 | 1.46 | 0.44 |
| p-value $m_H$ fixed | $1.59 \cdot 10^{-6}$ | $3.06 \cdot 10^{-4}$ | $1.55 \cdot 10^{-2}$ | $2.11 \cdot 10^{-1}$ |
| p-value $m_H$ floating | $1.08 \cdot 10^{-5}$ | $4.37 \cdot 10^{-3}$ | $1.44 \cdot 10^{-1}$ | $6.60 \cdot 10^{-1}$ |
| p-value'$m_H$ floating | $3.41 \cdot 10^{-5}$ | $6.56 \cdot 10^{-3}$ | $3.32 \cdot 10^{-1}$ | N/A |

Table 6.6: Significance $\sigma(S,B)$ for fixed and floating mass and p-value for fixed and floating mass. p-value' means floating mass p-value computed from Equation 6.17.

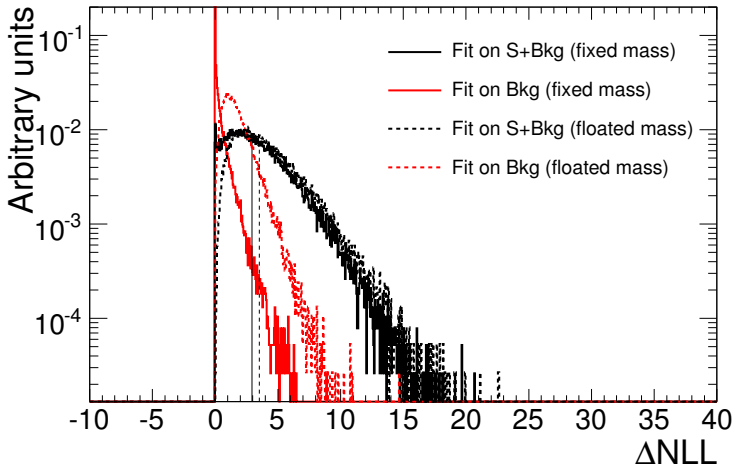


Figure 6.5: Comparison of distribution of $\Delta NLL$ for fixed mass and floating masses. The two black curves correspond to those for Signal+Background fixed mass (solid line) and floating mass (dotted line). The two red curves represent the Background-Only fixed mass (solid line) and floating mass (dotted line). The $x$-coordinate of the solid (dotted) perpendicular line corresponds to the median value for the distribution of signal+background outcomes in the fixed (floating) mass scenario. It is obvious that the impact on $\Delta NLL$ from the fixed mass case to the floating mass case is trivial. However, This effect is significantly different for the Background-Only outcomes as one can see that the p-value (integration of the detail from the median for background-only outcomes) will vary dramatically.

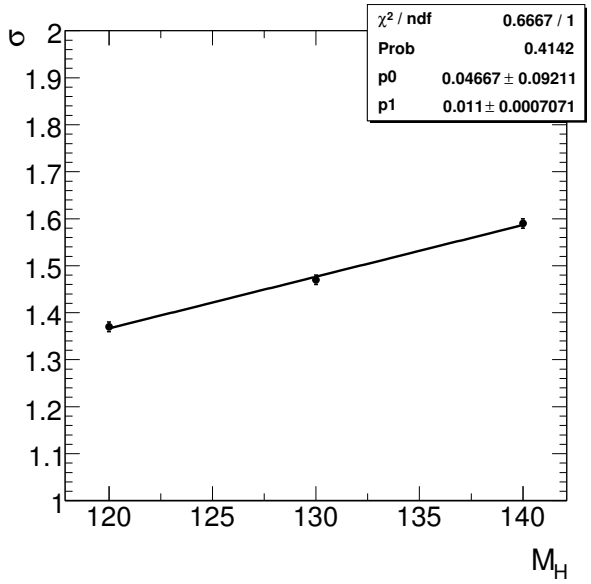


Figure 6.6: The linear parameterization of the inclusive Higgs mass resolution w.r.t the Higgs mass for inclusive $H \rightarrow \gamma\gamma$.

# Chapter 7

# Discovery potential and exclusion

## 7.1 Discovery potential

In this section I report on the potential for the discovery of a Higgs boson in the mass range $120 \leq M_H \leq 140$ GeV using the event counting computation and maximum likelihood fit formalism (see Chapter 6).

For the event counting method Poisson statistics are used to obtain the significance. For large statistics the significance of an observation can be approximated well by $S/\sqrt{B}$ (Gaussian statistics). In the combination using event counting, the signal significance for individual subchannels such as H+0 jet, H+1 jet and H+2 jet are summed up in quadrature:

$$\sigma(S,B)_{combined} = \sqrt{\sigma^2_{H\to\gamma\gamma+0j} + \sigma^2_{H\to\gamma\gamma+1j} + \sigma^2_{H\to\gamma\gamma+2j}} \tag{7.1}$$

For the fit based significance we implemented different approaches introduced in Chapter 6. The notations for those approaches are: $\sigma^{Fix}_{1Df}$, $\sigma^{Fix}_{C_1 3Df}$ and $\sigma^{Fix}_{C_2 3Df}$ corresponding to a one dimensional fit, a three dimensional fit by dividing events with $\eta$ classification, and a three dimensional fit (see Section 6.1) using all classifications

considered in Section 6.2, respectively, using a fix Higgs boson mass. The significances $\sigma_{1Df}^{Float}$, $\sigma_{C_1 3Df}^{Float}$ and $\sigma_{C_2 3Df}^{Float}$, correspond to fit based results obtained with a floating Higgs boson mass.

| | Analysis | | | | | | | | |
|---|---|---|---|---|---|---|---|---|---|
| | Inclusive | | | $H+1$jet | | | $H+2$jet | | |
| $m_H$ | $\sigma(S,B)$ | $\sigma_{1D}^{Fix}$ | $\sigma_{1D}^{Float}$ | $\sigma(S,B)$ | $\sigma_{1D}^{Fix}$ | $\sigma_{1D}^{Float}$ | $\sigma(S,B)$ | $\sigma_{1D}^{Fix}$ | $\sigma_{1D}^{Float}$ |
| 120 | 2.6 | 2.4 | 1.5 | 1.8 | 1.8 | 1.3 | 1.9 | 2.0 | 1.1 |
| 130 | 2.8 | 2.7 | 1.8 | 2.0 | 2.1 | 1.6 | 2.1 | 2.1 | 1.2 |
| 140 | 2.5 | 2.2 | 1.3 | 1.8 | 1.7 | 1.2 | 1.7 | 2.0 | 1.0 |

Table 7.1: Signal significances for a Standard Model Higgs boson as a function of the mass (in GeV) using the different analyses reported in Section 5.3.1-Section 5.3.3 for $10\,\text{fb}^{-1}$ of integrated luminosity. Results are reported in terms of the signal significance based on event counting, $\sigma(S,B)$, and a one dimensional fit-based signal significance, $\sigma_{1D}^{Fix}$ and $\sigma_{1D}^{Float}$.

| | Analysis | | | |
|---|---|---|---|---|
| $m_H$ | $H+0$jet (exclusive) | $H+1$jet (exclusive) | $H+2$jet | Combined |
| 120 | 2.2 | 1.5 | 1.9 | 3.3 |
| 130 | 2.3 | 1.6 | 2.1 | 3.5 |
| 140 | 2.0 | 1.6 | 1.7 | 3.0 |

Table 7.2: Signal significances for a Standard Model Higgs boson as a function of the mass (in GeV) using the different analyses reported in Section 5.3.4 for $10\,\text{fb}^{-1}$ of integrated luminosity. Results are reported in terms of the signal significance based on event counting, $\sigma(S,B)$ and correspond to Table 5.14.

Table 7.1 presents signal significance using the different analyses in Section 5.3.1-5.3.3 with $10\,\text{fb}^{-1}$ of integrated luminosity. The value of $\sigma(S,B)$ can be compared with earlier studies performed by the TLAS collaboration [69, 22, 55, 70, 57].

The other values of $\sigma_{1D}^{Fix}$ and $\sigma_{1D}^{Float}$ are those obtained from a fit-based method with either fixing or floating the Higgs boson mass. In the floating Higgs boson mass

scenario, the mass is floated in the range $110 \leq m_H \leq 140$ GeV for Higgs mass 120, 130 GeV and the range for a 140 GeV Higgs is $120 \leq m_H \leq 150$ GeV.

Table 7.2 shows the results of event counting for each individual subchannels such as H+0 jet, H+1 jet and H+2 jet and combined with Equation 7.1. In comparison to the inclusive analysis, the combined analysis enhances the sensitivity by 20%-30%.

Table 7.3 shows two fit-based signal significances compared to $\sigma_{1D}^{Fix}$ and $\sigma_{1D}^{Float}$ reported in Table 7.1. The values of $\sigma_{C_1 3D}^{Fix}$ and $\sigma_{C_1 3D}^{Float}$ correspond to the signal significance computed from a three dimensional fit, including $m_{\gamma\gamma}$, $P_{TH}$ and $|cos\theta^*|$ while fixing and floating the mass, respectively. At this stage the event classification according to $|\eta|$ regions is used (see Section 6.2). The values of $\sigma_{C_2 3D}^{Fix}$ and $\sigma_{C_2 3D}^{Float}$ correspond to the maximum achievable sensitivity of all the analyses reported in Section 5.3 combined. In addition to the procedure followed to obtain $\sigma_{C_1 3D}^{Fix}$ and $\sigma_{C_1 3D}^{Float}$, a classification of events according to the presence of hadronic jets is used.

| $m_H$[ GeV] | $\sigma_{1D}^{Fix}$ | $\sigma_{1D}^{Float}$ | $\sigma_{C_1 3D}^{Fix}$ | $\sigma_{C_1 3D}^{Float}$ | $\sigma_{C_2 3D}^{Fix}$ | $\sigma_{C_2 3D}^{Float}$ |
|---|---|---|---|---|---|---|
| 120 | 2.4 | 1.5 | 3.1 | 2.1 | 3.6 | 2.8 |
| 130 | 2.7 | 1.8 | 3.4 | 2.4 | 4.2 | 3.4 |
| 140 | 2.2 | 1.3 | 3.2 | 2.2 | 4.0 | 3.2 |

Table 7.3: Signal significances for a Standard Model Higgs boson as a function of the mass for $10\,\text{fb}^{-1}$ of integrated luminosity. Different fit-based approaches are used. The significances, $\sigma_{1D}^{Fix}$, $\sigma_{C_1 3D}^{Fix}$ and $\sigma_{C_2 3D}^{Fix}$ correspond to the fixed Higgs boson mass results. The significances $\sigma_{1D}^{Float}$, $\sigma_{C_1 3D}^{Float}$ and $\sigma_{C_2 3D}^{Float}$, correspond to fit-based results obtained with a floating Higgs boson mass (see text for the explanation of the notations).

Figure 7.1 displays a summary of the expected signal significance for the inclusive and final combined analysis for $10\,\text{fb}^{-1}$ of integrated luminosity as a function of the Higgs boson mass. The solid circles correspond to the sensitivity of the inclusive analysis reported in Section 5.3.1 using event counting with background and signal

rates assumed. The solid triangles linked with solid and dashed lines correspond to the sensitivity of the inclusive analysis by means of one dimensional fits, with a fixed and floating Higgs boson mass, respectively. The solid squares linked with solid and dashed lines correspond to the values of $\sigma^{Fix}_{C_2 3D}$ and $\sigma^{Float}_{C_2 3D}$ given in Table 7.3, respectively.

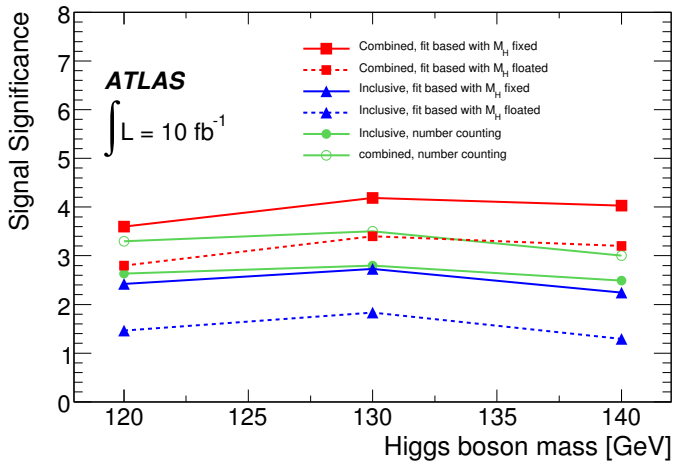


Figure 7.1: Expected signal significance for a Higgs boson using the $H \to \gamma\gamma$ decay for $10\,\mathrm{fb}^{-1}$ of integrated luminosity as a function of the mass. The solid circles correspond to the sensitivity of the inclusive analysis reported in Section 5.3.1 using event counting. The open circles display the event counting significance when the Higgs boson plus jet analyses (see Sections 5.3.2 and 5.3.3) are included. The solid triangles linked with solid and dashed lines correspond to the sensitivity of the inclusive analysis by means of one dimensional fits, with a fixed and floating Higgs boson mass, respectively. The solid squares linked with solid and dashed lines correspond to the maximum sensitivity that can be attained with a combined analysis (see text and Table 7.3).

## 7.2 Exclusion

The computation of exclusion limits has been discussed in Section 6.4.2. In this chapter the exclusion results with a mass scan are presented using the inclusive analysis. The resulting median likelihood ratio for exclusion, $\lambda(\mu)$ (using toy background only MC and taking the median of the $\lambda(\mu)$ distribution as given in Table 7.4), for a few Higgs masses at some given luminosities and $\mu = 1$ (which corresponds to a SM Higgs boson).

Figure 7.2 shows the exclusion of $\mu$ for an inclusive study with a mass scan and luminosity of $5\,\mathrm{fb}^{-1}$.

| L $\mathrm{fb}^{-1}$ | $m_H$ (GeV) 115 | 120 | 130 | 140 |
|---|---|---|---|---|
| 1 | 0.0676 | 0.1089 | 0.2209 | 0.0841 |
| 2 | 0.2500 | 0.4624 | 0.5476 | 0.2809 |
| 5 | 1.2321 | 1.8225 | 2.5281 | 1.4161 |
| 10 | 3.0276 | 4.5796 | 5.7121 | 4.0401 |
| 30 | 8.4700 | 10.4976 | 11.6281 | 9.0000 |

Table 7.4: Exclusion: the median $-2\log(q_\mu)(\mu = 1.0)$ for various Higgs masses and a few luminosities.

## 7.3 Conclusions

In this chapter, I discuss the feasibility of the search for Standard Model Higgs boson in the $H \to \gamma\gamma$ decay with the ATLAS detector. Based the analysis of Chapters 3-6, a signal significance with event counting of 2.6 can be obtained with 10 $\mathrm{fb}^{-1}$ of integrated luminosity for $m_H = 120GeV$ in the case of inclusive analysis. In addition

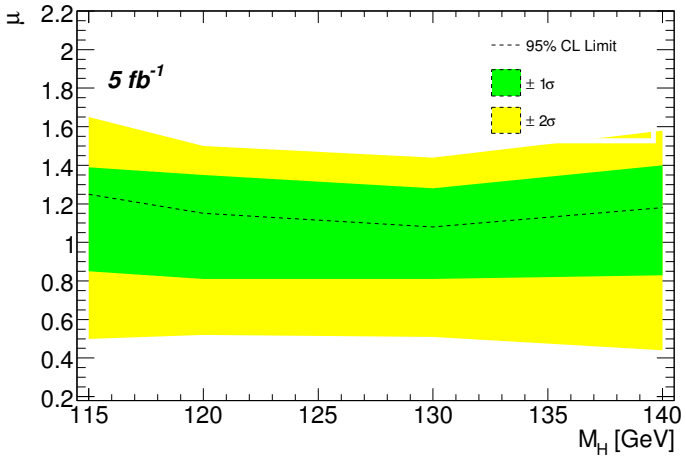


Figure 7.2: The exclusion of $\mu$ for inclusive study with a mass scan. The dashed line is the exclusion of $\mu$ with 95% CL. The green (yellow) band represents the exclusion of $\mu$ with variation of background outcome with $\pm 1\sigma$ ($\pm 2\sigma$) around the median. The luminosity for this plot is 5 fb$^{-1}$.

to the inclusive analysis, the combination of H+0 jet, H+1 jet and H+2 jets analyses can improve the significance about 27% for 120 GeV. The upper limit to the expected sensitivity has been estimated by the introduction of unbinned maximum likelihood fit by dividing the data into different sets of classifications and including more discriminating variables. The maximum enhancement of the discovery potential with respect to inclusive one has found to be 50% (80%) in the case of fixed (floating) mass fit with 10 fb$^{-1}$ of integrated luminosity. Around 5 fb$^{-1}$, this channel can be excluded with a 95% confident level.

# Bibliography


[1] W.-M. Yao et al., Particle data group., J. Phys G 33, 1 (2006).

[2] Albert Einstein, The foundation of the general theory of relativity., Annalen Phys., 49:768-822 (1916).

[3] Frank Wilczek, Quantum field theory., Review of Modern Physics 71 (1999) S85-S95.

[4] Elias kiritsis, Introduction to superstring Theory., hep-th/9709062 and references therein.

[5] David J. Gross, The role of symmetry in fundamental physics., Proc. Natl. Acad. Sci. USA, Vol. 93, pp. 14256-14259 (1996).

[6] G.'t Hooft, Renormalization of Massless Yang-Mills Fields., Nucl. Phys. B33:173 (1971).

[7] Chen-Ning Yang and R.L. Mills, Conservation of isotopic spin and isotopic gauge invariance., Phys. Rev. 96:191-195 (1954).

[8] Sau Lan Wu and Georg Zobernig., A method of three jet analysis in $e^+e^-$ annihilation., Zeit. Phys. C2:107, (1979).

[9] R.Brandelik et al., Evidence for planar events in $e^+e^-$ annihilation at high energies., Phys. Letts B86:243, (1979).

[10] G. Arnison et al., Experimental observation of lepton pairs of invariant mass around $95 Gev/c^2$ at cern sps collider., Phys. Lett. B126:398-410, (1983).

[11] G. Arnison et al., Experimental observation of isolated large transverse energy electrons with associated missing energy at $\sqrt{s} = 540 Gev$., Phys. Lett. B122:103-116, (1983).

[12] Peter W. Higgs, Broken symmetries, massless particles and gauge fields., Phys. Lett. 12:132-133 (1964).

[13] Peter W. Higgs, Broken symmetries and the masses of gauge bosons., Phys. Rev. Lett. 13:508-509 (1964).

[14] S.L. Glashow, Partial symmetries of weak interaction., Nucl. Phys. 22:579-588 (1961).

[15] S. Weinberg, A model of leptons., Phys. Rev. Lett. 19:1264 (1967).

[16] A. Salam, Elementary Particle Theory., Almqvist and Wiksells, Stockholm (1968).

[17] A. Djouadi, J. Kalinowski and M. Spira, HDecay: a program for Higgs boson decays in the Standard Model and its supersymmetric extension, hep-ph/9704448 April 1997.

[18] The LEP Collaborations (ALEPH, DELPHI, L3 and OPAL), the LEP Electroweak Working Group, Precision electroweak measurements and constrants on the Standard Model, arViv:0712:0929;http://lepewwg.web.cern.ch/LEPEWWG.

[19] R.Barate et al. ALEPH Collaboration, Observation of an excess in the search for the standard model higgs., Physics Letters B495:1, (2001).

[20] M. Benedikt et al., LHC Design Report. 3. The LHC injector chain., CERN-2004-003-V-3,(2004).

[21] B. Mellado et al, Higgs production cross-sections and branching ratios for the ATLAS Higgs working group., ATLAS-PHYS-PUB-2007-024.

[22] ATLAS Collaboration, Detector and physics performance technical design report., CERN-LHCC/99-14 (1999).

[23] ATLAS Collaboration, The ATLAS experiment at the CERN Large Hadron Collider., Preprint (2008).

[24] GEANT 4 Collaboration, GEANT 4-a simulation toolkit., Nuclear Instruments and Methods in Physics Research A506:250-303 (2003).

[25] H. U. Bengtson and T. Sojostrand., Pythia., Computer Physics Commun., 46:43, (1987).

[26] M.L. Mangano, M. Moretti, F. Piccinini, R. Pittau, A. Polosa., ALPGEN, a generator for hard multiparton processes in hadronic collisions., JHEP 0307:001, (2003).

[27] G. Corcella, I.G. Knowles, G. Marchesini, S. Moretti, K. Odagiri, P. Richardson, M.H. Seymour and B.R. Webber., HERWIG 6: an event generator for hadron emission reactions with interfering gluons., JHEP 0101 010 (2001).

[28] S. Frixione and B.R. Webber., Matching NLO QCD computations and parton shower simulations., JHEP 0206 029 (2002).

[29] S. Frixione, P. Nason and B.R. Webber., Matching NLO QCD and parton showers in heavy flavour production., JHEP 0308 007 (2003).

[30] D. Costanzo, et al., The Geant4-based simulation software of the ATLAS detector, IEEE Nuclear Science Symposium Conference Record, 2006.

[31] E. Richter-Was, D. Froidevaux and L. Poggioli, ATLFAST2.0 a Fast Simulation Package for ATLAS., ATLAS Note ATL-PHYS-98-131 (1998).

[32] A Khmadaliev S.Z. et al., Results from a new combined test of an electromagnetic liquid argon calorimeter with a hadronic scintillating-tile calorimeter., Nucl. Instrum. Methods Phys. Res. A 449:461-77 (2000).

[33] W. Lampl, et al., Calorimeter clustering algorithms: description and performance, ATL-LARG-PUB-2008-002.

[34] $H \rightarrow \gamma\gamma$ group of the ATLAS collabration, Prospects for the discovery of the Standard Model Higgs Boson using the $H \rightarrow \gamma\gamma$ decay with the ATLAS detector., contribution to ATLAS CSC book, in preparation.

[35] The ATLAS Collaboration, Photon conversions in ATLAS, contribution to ATLAS CSC book, in preparation.

[36] I. Koletsou, PhD thesis,, Universite Paris 11, LAL 08-38, April 2008 (unpublished).

[37] G. Unal, L. Fayard, Photon identification in gamma-jet events with Rome layout simulation and background to $H \rightarrow \gamma\gamma$., ATLAS-PHYS-PUB-2006-025.

[38] M. Escalier et al., Photon/jet separation with DC1 data., ATLAS-PHYS-PUB-2005-018.

[39] M. Wielers, Photon identification with the Atlas detector, ATLAS-PHYS-99-016.

[40] Photon ID and combined peformances group of the ATLAS collabration, ATLAS photon identification algorithms and their performances., contribution to ATLAS CSC book, in preparation.

[41] K. Benslama, Private communication..

[42] K. Cranmer, Kernel estimation in high-energy physics., Computer Physics Communications, Volume 136, Number 3, 15 May 2001 , pp. 198-207(10).

[43] D.L. Rainwater, Ph.D. thesis, University of Wisconsin-Madison., hep-ph/9908378.

[44] Abdullin, S. et al., Higgs boson discovery potential of LHC in the channel $pp \rightarrow \gamma\gamma + jet.$, Phys. Lett. B431:410-419, (1998).

[45] The CMS Collaboration, CMS physics technical design report.

[46] S.Laplace et al., New developments for $H \rightarrow \gamma\gamma$, Talk present at Higgs working group meeting, CERN, November 15, 2006.

[47] T. Binoth, J.P. Guillet, E.Pilon and M. Werlen, A Full next-to-leading order study of direct photon pair production in hadronic collisions., Eur.Phys.J.C16:311-330, (2000).

[48] C. Balazs and C.P. Yuan., Soft gluon effects on lepton pairs at hadron colliders., Phys.Rev.D56:5558-5583, (1997).

[49] P. Nadolsky, C. Balazs, Edmond L. Berger, C.-P. Yuan., Gluon-gluon contributions to the production of continuum diphoton pairs at hadron colliders., Phys.Rev.D76:013008, (2007).

[50] M. Escalier, Ph.D. thesis, University Paris., CERN-THESIS-2005-023.

[51] S. Catani et al., Cross-section of isolated prompt photons in hadron hadron collisions., HEP 0205:028, (2002).

[52] Zoltan Nagy, Three-jet cross sections in hadron-hadron collisions at next-to-leading order., Phys.Rev.Lett. 88 (2002).

[53] Zoltan Nagy and Zoltan Trocsanyi, Multi-jet cross sections in deep inelastic scattering at next-to-leading order., Phys.Rev.Lett. 87 (2001).

[54] ATLAS Collaboration, Overall trigger strategy for the electron and photon selection., ATL-PHYS-PUB-2008-xxx.

[55] Bettinelli, M et al., Search for a SM Higgs decaying to two photons with the ATLAS detector., ATL-PHYS-PUB-2007-013.

[56] ATLAS Collaboration, Jet calibration: strategies and performances., this volume.

[57] K. Cranmer, B. Mellado, W. Quayle and Sau Lan Wu, Search for higgs boson decay $H \rightarrow \gamma\gamma$ using vector boson fusion, ATL-PHYS-2003-036, hep-ph/0401088.

[58] David L. Rainwater, R. Szalapski and D. Zeppenfeld, Probing color-singlet exchange in z+2jet events at the LHC, Phys. Rev., D54:5580-6689,1996.

[59] W. Quayle et al., Signal extraction in $WW \rightarrow l\nu qq$, Talk present at Higgs working group meeting, CERN, September 13, 2006.

[60] Y. Fang et al., Signal Significance in $H \to \gamma\gamma$+1, 2jet and combined analyses, Talk present at Higgs working group meeting, CERN, Decemember 13, 2006.

[61] J.E. Gaiser, Charmonium spectroscopy from radiative decays of the J/Psi and Psi-Prime, Ph.D. Thesis, SLAC-R-255 (1982).

[62] Nicolas Berger et al., Update on $H \to \gamma\gamma$ study, Talk present at CSC $H \to \gamma\gamma$ group meeting, CERN, December 20, 2007.

[63] W. Verkerke and D. Kirkby, The RooFit toolkit for data modeling, Computing in High Energy and Nuclear Physics, 24-29 March 2003.

[64] Y. Fang et al., Statistics from $H \to \gamma\gamma$ group, Talk present at ATLAS Statistics Forum Higgs Combination Workshop, CERN, May 11, 2008.

[65] I. Koletsou, G. Unal and L. Fayard, Preliminary study of S/sqrt(B) in Higgs to $\gamma\gamma$, ATL-PHYS-INT-2006-003.

[66] W. Quayle et al., Signal extraction in $H \to l\nu qq$, Talk present at CSC Higgs working group meeting, CERN, October 11, 2007.

[67] Y. Gao,L. Lu, X. Wang, Significancd calculation and a new anlysis method in searching for new physics at the LHC, Eur. Phys. J. C45 (2006) 659.

[68] The ATLAS Statistics Forum, Statistical combination of ATLAS Higgs results, contribution to ATLAS CSC book, in preparation.

[69] L. Fayard and G. Unal, Search for Higgs decays using photon with EAGLE, ATL-PHYS-92-001.

[70] S. Zmushko, Search for $H \to \gamma\gamma$ in association with one jet, ATL-PHYS-2002-020.